TURBINE VANE FILM COOLING AND INTERNAL ROTATING COOLANT PASSAGE HEAT TRANSFER

A Dissertation

by

SHANG-FENG YANG

Submitted to the Office of Graduate and Professional Studies of
Texas A&M University
in partial fulfillment of the requirements for the degree of

DOCTOR OF PHILOSOPHY

Chair of Committee,	Je-Chin Han
Committee Members,	Hamn-Ching Chen
	Eric L. Petersen
	Sai Lau
Head of Department,	Andreas A. Polycarpou

December 2014

Major Subject: Mechanical Engineering

ABSTRACT

The first part of this dissertation experimentally studies the effect of transonic flow velocity on local film cooling effectiveness distribution of turbine vane suction side. Pressure Sensitive Paint (PSP), a conduction-free method is used to determine local film cooling effectiveness. Tests were performed in a five-vane annular cascade at TAMU Turbolab blow-down flow loop facility. The exit Mach numbers are controlled to be 0.7, 0.9, and 1.1, from subsonic to transonic flow conditions. Three foreign gases N_2, CO_2 and Argon/ SF_6 mixture are selected to study the effects of three coolant-to-mainstream density ratios, 1.0, 1.5, and 2.0 on film cooling. Four averaged coolant blowing ratios in the range, 0.7, 1.0, 1.3 and 1.6 are investigated. The test vane features 3 rows of radial-angle cylindrical holes around the leading edge, and 2 rows of compound-angle shaped holes on the suction side. Results suggest that the PSP is a marvelous technique capable of producing clear and detailed film cooling effectiveness contours at transonic condition. The effects of coolant to mainstream blowing ratio, density ratio, and exit Mach number on the vane suction-surface film cooling distribution can be obtained, and the consequence results can be presented and explained in this research.

The second part of this dissertation experimentally investigates the effect of rotation on heat transfer in typical turbine blade serpentine coolant passage with ribbed walls at low Mach numbers. To achieve the low Mach number (around 0.01) condition, pressurized Freon R-134a vapor is utilized as the working fluid. The flow in the first passage is radial outward, after the 180° tip turn the flow is radial inward to the second passage, and after the 180° hub turn the flow is radial outward to the third passage. The effects of rotation on the heat transfer coefficients were investigated at rotation numbers up to 0.6 and Reynolds numbers from 30,000 to 70,000. Heat transfer coefficients were measured using the thermocouples-copper-plate-heater regional average method. Heat transfer results are obtained over a wide range of Reynolds numbers and rotation numbers. An increase in heat transfer rates due to rotation is observed in radially outward passes; a reduction in heat transfer rate is observed in the radially inward pass. Regional heat transfer coefficients are correlated with Reynolds numbers for non-rotation and with rotation numbers for rotating condition, respectively. The results can be useful for understanding real rotor blade coolant passage heat transfer under low Mach number, medium-high Reynolds number and high rotation number conditions.

DEDICATION

This dissertation is lovingly dedicated to my mother, Yue-Feng Chen. Her support, encouragement, and constant love have sustained me throughout my life.

ACKNOWLEDGEMENTS

I would like to thank my committee chair, Dr. Je-Chin Han, and my committee members, Dr. Hamn-Ching Chen, Dr. Eric Petersen, and Dr. Sai Lau, for their guidance and support throughout the course of this research.

Thanks also go to my friends and colleagues and the department faculty and staff for making my time at Texas A&M University a great experience. I also want to extend my gratitude to the Department of Energy, Solar Turbines Inc, Siemens Energy Inc. and Honeywell Aerospace Turbine Company, which supported my research.

Finally, thanks to my family for their encouragement and to my fiancée Yu-Hsi Lin for her patience and love.

NOMENCLATURE

Cx	Axial chord length of the test vane
d	Diameter of film cooling hole
DR	Density ratio
H	Vane height
I	Image pixel intensity
L	Actual vane surface length
LE	Leading edge of vane
M	Blowing ratio = $(\rho V)_{coolant}/(\rho V)_{mainstream}$
Ma	Mach number
P	Partial pressure
S	hole-to-hole spacing
V	velocity
W	molecular weight
X	surface distance from vane leading edge
y	spanwise distance from hub
η	film cooling effectiveness
ρ	fluid density
A	heat transfer surface area of a copper plate
AR	channel aspect ratio, W:H
Bi	Biot Number

Bo	Local buoyancy parameter
cp	specific heat at constant pressure
Dh	channel hydraulic diameter
H	channel height
h	regionally averaged heat transfer coefficient
i	designates a given region in the channel (1≦i≦15)
I	current
k	thermal conductivity of the coolant
m	mass flow rate
Nu	regionally averaged Nusselt number
Nus	stationary regionally averaged Nusselt number
Nu0	Nusselt number for fully developed turbulent flow in stationary smooth pipe
Pr	Prandtl number of the refrigerant
Qin	total power input
Qnet	net heat transfer
Qloss	external heat loss
R	Electric resistance for each heater
Re	Reynolds number
Ro	Rotation number, ΩDh /Ub
Tw	regionally averaged wall temperature
Tb	local coolant bulk temperature

Tb,in	bulk fluid temperature at inlet of a given region
Tb,out	bulk fluid temperature at outlet of a given region
Ub	bulk velocity in streamwise direction
V	voltage
W	channel width
Ω	rotation speed

TABLE OF CONTENTS

LIST OF FIGURES

LIST OF TABLES

Page

CHAPTER I

INTRODUCTION

The inceptive stages of a modern gas turbine are continually exposed to extremely high temperatures gases exiting the combustion chambers. In pursuit of higher thermal efficiencies and power output, contemporary gas turbines are operated at turbine rotor inlet temperature (RIT) around 1500°C; by far higher than the material melting point (around 1000°C). Continuous operation under extremely high RIT greatly endangers and jeopardizes the integrity of hot gas path components due to enhanced probability of thermal failure. Thus the initial stages of turbine components are cooled by compressor discharge air (around 650°C) in most recent designs. Gas turbine vanes and blades lifespan can be significantly increased by implementing a variety of internal and external cooling techniques comprehensively documented by Han et al. [1]. External cooling is also well-known as film cooling in open literature, and this technique is commonly used in coincidence with internal cooling methods to protect the turbine components from thermal failure. Figure 1 illustrated the schematics of most employed internal and external methods for typical cooling design in a turbine blade.

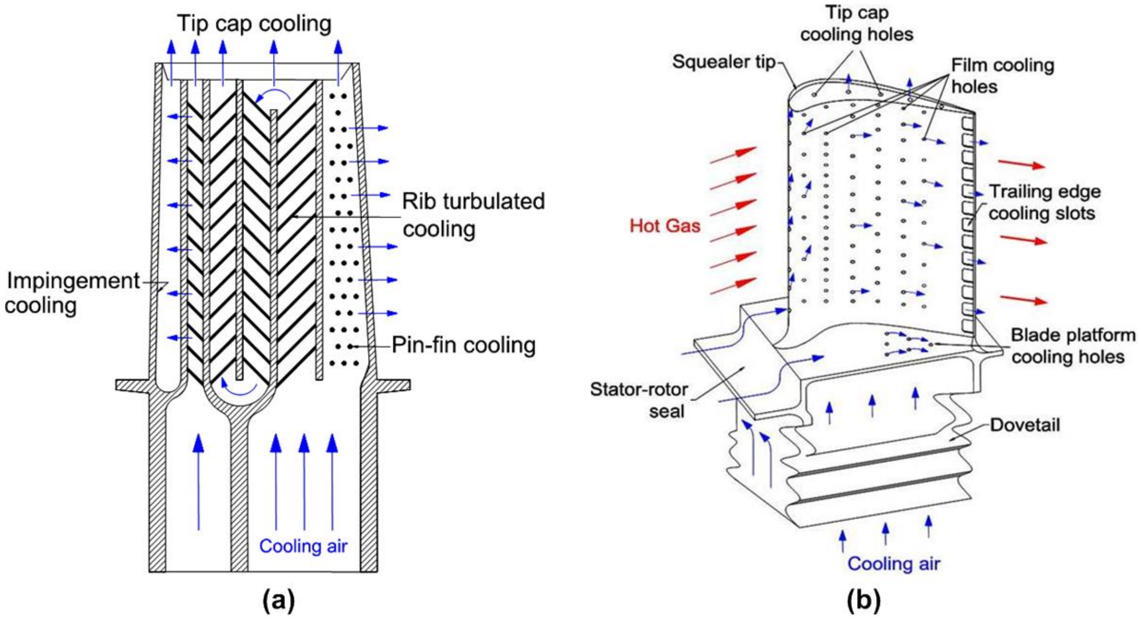

Figure 1 Typical gas turbine blade/ vane cooling scheme (a) internal cooling; (b) external cooling

CHAPTER II

TRANSONIC FILM COOLING EFFECTIVENESS OF TURBINE VANE SUCTION SIDE WITH COMPOUND-ANGLE SHAPED HOLE CONFIGURATION STUDY

The primary concept of film cooling is to dislocate the mainstream boundary layer by creating a protective film of ejected coolant that insulates the material surface of exposed component. The compressed air bled from compressor stages, ducted and circulated through the internal plenums and passages inside the turbine blades, and finally discharged to the mainstream flow through series of coolant configuration design. The released compressed coolant provides a diaphanous, relatively cool layer that protected the exposed material surface as function of a shield. This technique enables the contemporary turbines components to withstand the drastic RIT and extends their lifespan. For the past decades, gas turbine designer and engineers always struggled to maximize the cooling performance with less coolant in order to obtain optimum results for overall engine efficiency. And this optimum efficiency can be often described with three coupled major factors; they are quantity, momentum, and distribution. (1) Quantity, the more coolant air extracted from the compressor stage, the lower overall engine efficiency. (2) Momentum, when the magnitude of coolant jet momentum is too high, instead of forming a thin protection layer attached on the exposed material surface, it will lift off from the surface and shoot into the mainstream directly. Therefore, the blade surface lost its shielding from extreme RIT and the efficiency of film cooling design is limited. (3) Distribution, local hot spots are usually found between two discrete coolant traces. At these locations the material surfaces are most not well covered by the thin coolant layer. Especially momentum and distribution are the main reasons that cause un-uniform coolant coverage and local hot spots.

II.A. Literature Survey

The major factors that would affect blade surface film cooling and heat transfer have been recognized as cooling configuration; the location, quantity and geometry, blowing ratio, density ratio, free-stream turbulence and blade tip leakage. And these parameters were concluded from Goldstein [2], Han et al. [1], Bunker [3], Bogard and Thole [4], and Han and Rallabandi [5]. This study focuses on the transonic adiabatic film cooling effectiveness and heat transfer of an innovative vane suction side design. The experiment work is carried out in a 1:3 scaled up 5 vane annulus cascade.

II.A.1. Cooling Configuration Effect

Gas turbine designers and engineers always tried to aggrandize cooling efficiency by extracting less and less coolant from compressor stage and obtain maximum cooling performance. After decades of extensive study, it is proved in open literature that the cooling geometry has a prominent impact on film cooling phenomenon.

Among the variety of film cooling hole designs, there are four kinds of geometries are generally considered in research study and actual component design. The four design are cylindrical holes, laterally-diffused (fan shape) holes, forward-diffused holes (laidback) holes, and laterally and forward-diffused (laidback fan shape) holes. Four cooling hole design parameters are displayed in Figure 2 and the dashed lines represent the center lines of all hole shapes. The angle between the main-flow direction and cooling hole center line is defined as compound angle (β). Depend on the compound angle, the cooling features are indentified as an compound angle hole if $\beta \neq 0$, and otherwise axial hole. Coolant jets distribution at each design exits are also conceptually illustrated in Figure 2.

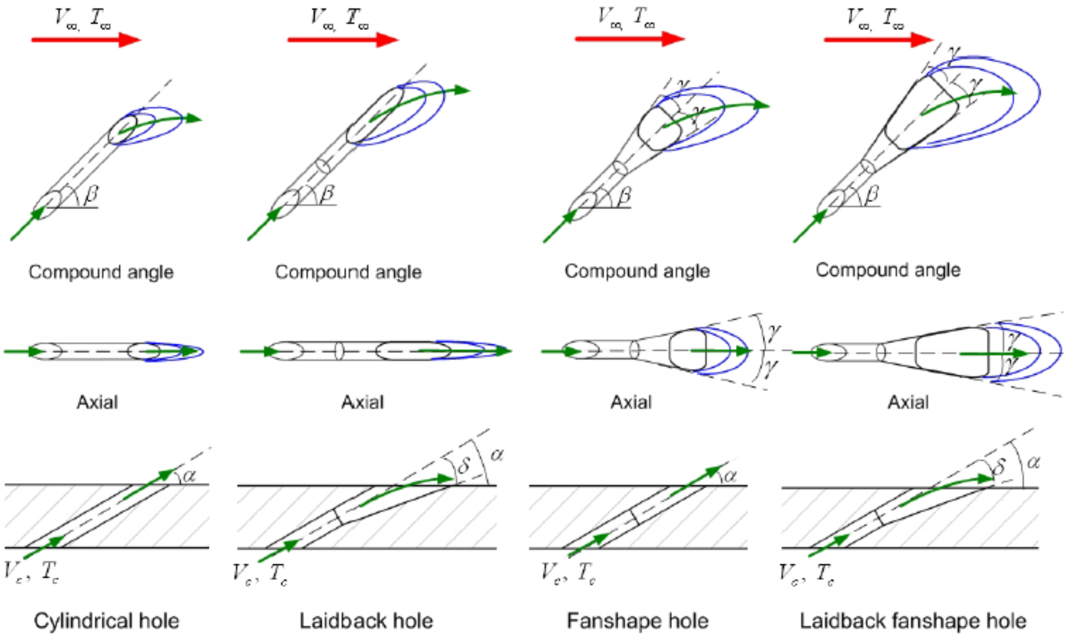

Figure 2 Four commonly used film cooling hole configurations

Generally speaking, the compound angle usually yields better film cooling effectiveness. A larger film covered area due to the coolant jet deflected by the main-stream flow. And the shaped hole performs better than the cylindrical holes ($\delta = \gamma = 0$), since the jet expends at the hole breakout area and reduces the momentum. Thus decreases the possibility of jet lift-off from the material surface.

Flat plate experiments often serves as the base line of film cooling study. Goldstein et al [6] demonstrated the benefits of shaped holes design. In the study, they compared film-cooling effectiveness for cylindrical holes and axial shaped holes with 10°lateral diffusion angle (γ). And both holes were designed with 35° inclined angle (α) from breakout surface. The study results showed a significant enhancement in film cooling effectiveness immediately downstream of the laterally expanded configuration. This phenomenon primarily associated to the reduced coolant jet mean velocity at the cooling exits causing the jet to stay near to the surface.

Thole et al. [7] studied flow field at the exit of three different hole exit geometries with LDV. These geometries included cylindrical hole, laterally expanded hole, and forward-laterally expanded hole. All holes were inclined 30° (α) angle from the surface. Their results indicated that both laterally and forward-laterally expanded holes experienced less shear mixing of cooling jet with the mainstream and greater lateral spreading of the coolant compared to that of the cylindrical hole. Additionally, the forward-laterally expanded design had relatively lower film effectiveness than the laterally expanded exit due to excessive diffusion of the coolant jet and subsequent mainstream interaction. Gritsch et al. [8] studied the same cooling configurations and orientations as [7] with a density ratio of 1.85. The film-cooling effectiveness data were confined to $x/D = 10$ in order to focus on the near hole region. Their results indicated both expanded exits demonstrated significantly improved thermal protection at surface downstream of jet exits when compared with cylindrical hole. This trend is more prominent particularly at high blowing ratios. Yu et al. [9] studied film effectiveness and heat transfer distributions on a flat plate with three configurations; cylindrical, 10° forward diffusion and 10° in both forward and lateral diffusion. The center lines of all designs are orientated 30° (β) relative to the mainstream direction. The result point out that among the three designs, the one with both forward and lateral diffusion provided the best film cooling performance.

Schmidt et al. [10] concluded that the compound-angled holes provide better coolant coverage compared with axial holes. Their results show that 60° compound angled holes, with and without forward expanded shaped exit, have much greater effectiveness than cylindrical holes aligned with the mainstream at larger momentum flux ratios. Several studies in the open literature (Ekkad et al. [11], Wright et al. [12], and Goldstein and Jin [13]) achieved similar conclusions using different experimental techniques. Ito et al. [14] and Liu et al. [15] showed the effect of curvature on film cooling effectiveness. Ito et al. reported higher effectiveness on a convex surface than on a flat plate at low momentum flux ratio and the reverse at high momentum flux ratio. The trend is reversed on concave wall. Liu et al. reported in both convex and concave surfaces, the film cooling effectiveness of compound shaped hole configuration is significantly higher compared with axial cylindrical designs. Li et al. [16] and Liu et al. [17] compared the film cooling effectiveness of shaped and cylindrical configuration on a leading edge and the end wall of a turbine blade respectively. Both studies concludes that the shaped hole designs provides superior film cooling performance compared with cylindrical configuration.

II.A.2. Blowing Ratio Effect

Blowing ratio has been extensively studied in the past and it is defined as the mass flow ratio between coolant jet and mainstream flow. Optimizing this parameter in film cooling design is of crucial importance. Since insufficient coolant in low blowing ratio scenario would not provide enough coolant film coverage to the blade surface, and in excessively high blowing ratio scenario the coolant will lift-off from the blade surface and cannot provide proper shielding as well. Past studies indicates the optimum blowing ratio depends on the cooling configuration design as well.

Goldstein et al. [2, 18] concluded the optimum blowing ratio for cylindrical holes is abound M = 0.5. For blowing ratios higher that 0.5, coolant jets tend to penetrate into the mainstream and reduce the cooling effectiveness. For further downstream of the surface, the effectiveness tended to increase with the blowing rate. This is due to the lifted-off coolant jets were turned by mainstream flow and reattached to the surface.

Cho et al. [19] compared the blowing ratio effects for two different types of hole shapes. (1) $\delta = \gamma = 4\,^{\circ}$; diffused in all direction, (2) forward diffusion of $\delta = 8\,^{\circ}$. The results indicated the coolant tends to be more separate from the surface and reduces the cooling effectiveness as blowing ration increases. The optimum blowing ratio for cylindrical hole in this study is also closed to M = 0.5. All direction diffused design showed decreasing effectiveness for further increasing blowing ratio over M=1.0. Forward diffusion configuration performed similarly when compared to the other holes. At M=2.0, the film cooling effectiveness distribution was more similar to the cylindrical design. Since this design has only expansion in forward direction, the diffusion of coolant in the hole is asymmetric. Therefore the interaction between the mainstream and the coolant is more significant.

The Turbine Heat Transfer Laboratory (THTL) at Texas A&M University has undertaken a series of study on film-cooling in their 5-blade linear cascade facility. Mhetras and Han [20], Narzary et al. [21], and Gao et al. [22] studied film-cooling in blades featuring compound cylindrical holes, compound shaped holes, and axial shaped holes, respectively. Between all the configurations, compound shaped holes produced the highest effectiveness on the suction side followed by compound cylindrical holes and axial shaped holes at a given blowing ratio. Liu et al. [15] studied the film cooling effectiveness distribution on turbine blade convex (suction) and concave (pressure) surfaces with shaped hole design. They demonstrated the film cooling effectiveness in both concave and convex surfaces has a positive correlation with blowing ratio. However, in convex surface this trend only valid within M= 1.0~1.5 range. The effectiveness in M=2.0 decreased to lower than M=1.5 case.

II.A.3. Density Ratio Effect

The relatively cool (650°C) compressed air extracted from the compressor stages of a real gas turbine engine is used for film cooling coolant. Compared with the RIT (1500°C), the temperature difference between coolant and hot mainstream flow causes a notable density difference. The density ratio is defined as the ratio of coolant to mainstream densities, and it is usually range from 2 to 3 in contemporary gas turbine engines. In laboratory studies, gases with greater molecular weight are used to simulate the density ratio effect.

Pedersen et al [23], Sinha et al. [24] and Ethridge [25] et al. conducted experiment studies and draw similar conclusion. As density ratio increases, the peak on cooling effectiveness moves toward to higher blowing ratio. For a constant density ratio, the film cooling effectiveness reaches a peak as blowing ratio increases and starts to drop off at relatively high blowing ratio. Due to the coolant ejection penetrates through the mainstream and losses the protection of the blade surface. Peaks move toward higher blowing ratio by increasing density ratio and provide higher effectiveness. Thus, they concluded that due to less mixing and lower momentum in greater density ratio scenarios, coolant tends to attach closer to the blade and provide a significant improvement in film cooling effectiveness.

Goldstein [6] proved that film cooling performance at coolant ejection downstream was greatly improved when the coolant density ratio is high, particularly at high blowing ratios. Liu et al. [15] proved similar conclusion on both suction and pressure surface of a turbine blade. They studied three densities (DR= 1.0, 1.5, and 2.0). In recent years, several film cooling effectiveness and heat transfer on the surface of transonic airfoil has been studied in the literature. Furukawa and Ligrani [26] studied different geometry of film cooling hole and concluded the compound-angle shaped holes performs better than axial shaped holes and axial cylindrical holes. Kodzwa and Eaton

[27], [28] demonstrated that increasing coolant density improves effectiveness when the coolant jets are attached to the surface. And they also significant heat transfer attenuation far downstream at high blowing conditions.

Several experiment techniques have been applied to determine film cooling effectiveness in open literature. For almost identical conditions, the film cooling effectiveness data determined by thermal methods are higher than mass transfer analogy methods. Due to lateral conduction take place in low conductivity substrate plate in regions of high thermal gradients. This issue has been discussed by Nicoll and Whitelaw [29], and Wright et al. [12].

II.A.4. Free-Stream Turbulence Effect

In stationary cascade experiment setups, free-stream turbulence is often generated by employing upstream grids into the mainflow path. This grid serves as a blockage to the mainstream flow. In a Jet grid setup, air is forced through an array of pipes into mainstream flow, and it is also used to generate free stream turbulence. The turbulence intensity at the combustor exit is around 7 to 20%. Thus to have up to 20% turbulence intensity at inceptive stage is one of the most important goals for test section design.

Kadotani [30, 31] tested turbulent intensities ranging from 0.3 to 20.6% with cylindrical holes inclined 33°to the mainstream. They observed that the centerline effectiveness of high turbulence intensity cases decreased with low blowing ratio but increased in high lowing ratio cases. Due to the turbulent mixing reduced the possibility of coolant jet penetration into mainstream. In addition, high turbulence intensity improved coolant lateral distribution for the cylindrical holes. And this is helpful to diminish the potential local coolant film unshielded hot spots.

Mehendal [32] investigated the effect of turbulence intensity on turbine blade leading edge. They employ local aerial average method to determine the cooling effectiveness on the semicircular leading edge with flat downstream body. The blowing ratio range varied from 0.4 to 1.2 for different free stream turbulence levels (9.67, 12.9%). They found that the free stream turbulence processed a negative effect on the film cooling effectiveness at leading edge. Greater free stream turbulence intensity accelerated coolant jet to dissipate into the mainstream. In addition, the highly turbulent mainstream tends to penetrate and mix with film cooling layer and therefore decrease the effectiveness. By increasing the coolant blowing ratio, the coolant jet momentum is stronger and unsteady mainstream causes fewer disturbances. Therefore at leading edge portion, turbulence effect is less on film cooling effectiveness.

Burd et al. [33] studied the interaction between film cooling hole L/D and free stream turbulent intensity. In their study, hot wire anemometer technique was employed to measure mainstream turbulence intensity on cylindrical holes angled 35°to the mainstream. Two turbulent intensities (0.5 and 12%) were studied while varying the L/D ranged from 2.3 to 7. This study concludes with low free-stream turbulence and short holes, the coolant is ejected farther from the wall and spreads more in the spanwise direction when compared to a long hole. However, at high free-stream turbulence level, the coolant flow distribution difference between large and small L/D holes significantly decreases.

Liu et al. [15] studied two turbulence intensities (Tu= 4.2 and 10.5%) on both suction and pressure surface of a turbine blade. They conclude free stream turbulence has a negative effect on film-cooling effectiveness as it induces more mixing.

II.B. Objectives of this Study

This research is to study the effect of transonic flow on turbine vane suction side film cooling effectiveness and heat transfer with Pressure Sensitive Paint (PSP) and Transient Liquid Crystal (TLC) methods. Tests were performed in a five-vane annular cascade with a blow-down facility at Texas A&M University Turbomachinery Laboratory. The exit Mach numbers are controlled in a range from subsonic (Ma#= 0.7, and 0.9) to supersonic (Ma#=1.1). The test vane features 3 rows of 7 radial-angle cylindrical holes (total 21) at the leading edge, and 2 rows of 7 compound-angle shaped holes on the suction side. Three density ratios (DR= 1.0, 1.5, and 2.0), and four blowing ratios (M=0.7, 1.0, 1.3, and 1.6) were investigated in this study.

Study results are presented in the form of film cooling effectiveness, heat transfer coefficient contours and spanwise-averaged plots. Employing mass transfer analogy, film cooling effectiveness is measured with pressure sensitive paint (PSP) method. And liquid crystal method is used to determine heat transfer coefficient under varying cooling coolant temperature circumstances.

II.C. Experimental Setup

II.C.1. 5-Vane Annular Cascade

The test section consisted of a stationary blow-down facility (**Fig. 3**) with a 5-vane annular cascade and a removable test vane (**Fig. 4(a)**). Pressurize air stored in reservoir tank enters a high flow pneumatic control valve that designed to receive feedback from the downstream pressure transducers that controls the mainstream velocity within ±3% of desired setting. Both the transition ducts at test section inlet and exit had 4 inch inner diameter and were made of 0.125 inch aluminum.

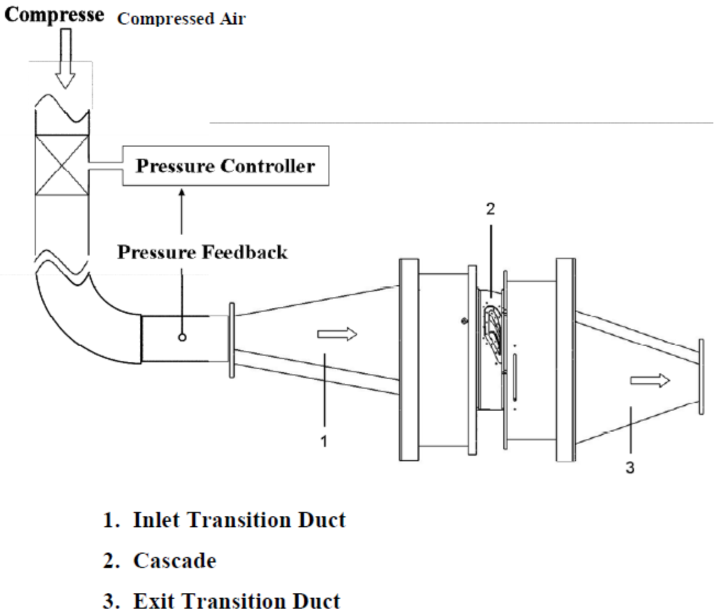

Figure 3 Schematic of blow down facility and digital controller setup

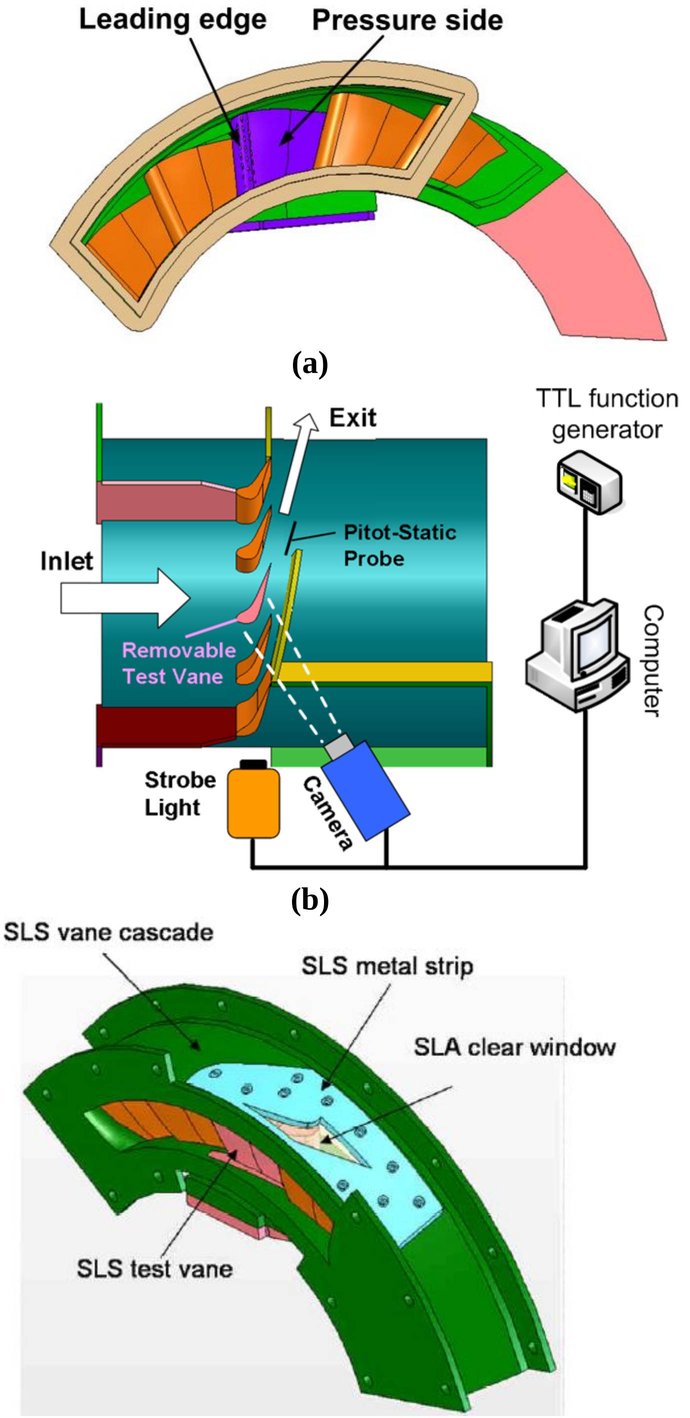

(a)

(b)

(c)

Figure 4 Test section setup (a) annular 5-vane cascade, (b) schematic of optical setup, (c) test cascade assembly

A schematic of the optical setup is shown in **Fig. 4(b)**. Due to safety concern while operating at high pressure, a limited size of viewing window manufactured by stereolithography (SLA) process is used to monitor the interested area (**Fig. 4(c)**). The test cascade and the metal reinforce cover were made of Selective Laser Sintering (SLS) technique. The SLA window is installed directly on the test vane top and it is bolted with the SLS cascade and SLS reinforce cover to provide additional protection.

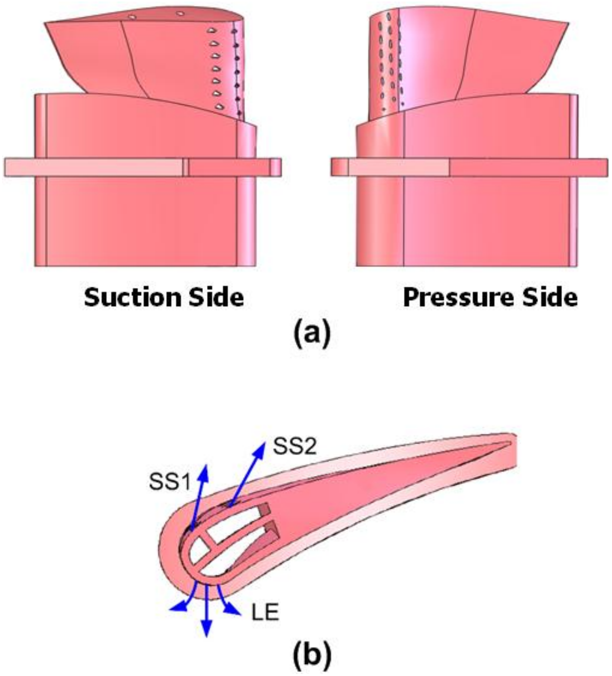

Figure 5 Test vane (a) hole locations (b) coolant passage

In the present study, the three target cascade exit Mach number (Ma_{exit}) were 0.7, 0.9, and 1.1. The corresponding Reynolds numbers based on axial chord length and exit mainstream velocity are 6.33×10^5, 8.16×10^5, and 9.98×10^5. The exit velocity was continuously monitored using a Pitot-static pressure probe placed 75% of chord length downstream of the cascade.

A scaled up model of Honeywell vane was placed in the center of annular cascade. Test vane manufactured by Selective Laser Sintering (SLS) process. **Figure 5(a)** shows the unique shape and cooling configuration of the vane. The test vane height decreases from leading edge to trailing edge as of 5.85 to 4.63 cm and the axial chord length is 3.96 cm. The leading edge of the test vane is equipped with three rows of cylindrical film cooling holes on the leading edge. Three leading edge rows are staggered with respect to one another with the middle row aligned with stagnation line. Each row has 7 holes with a hole-to-hole spacing of $s/d = 6.9$ and the incline angle with respect to the vertical is 15.8°. Two rows of compound-angle shaped holes (SS1, SS2) on the suction side with a hole-to-hole spacing of $s/d = 7.3$ and the incline angle is also 15.8°. Surface near the leading edge and trailing edge are out of visual range and cannot be seen. Shaded area represents the actual portion from the view of the camera (**Fig. 5(a**)). Each Coolant jet individually travels through a vertical circular (diameter 6.35mm, 64 mm long) passage before entering the vane design. And then the jets are delivered to three plenums with various cross-section areas as illustrated in **Fig. 5(b)**. And coolant flow in each passage is individually controlled by a rotameter in the experiment apparatus in **Fig. 6**.

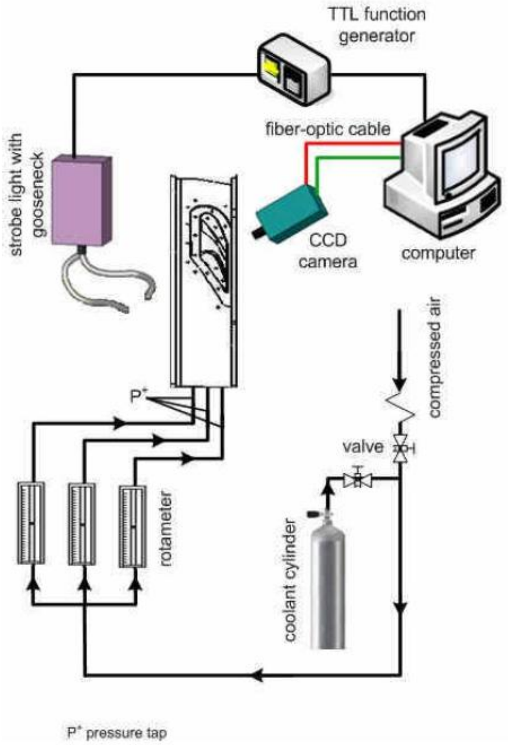

Figure 6 Schematic of experimental facility

II.C.2. Instrumentation

To monitor the exit velocity, a Pitot-static probe is stationed 75% chord length downstream of the test vane. And the real time pressure data from the Pitot-static tube is recorded by a Scanivalve system (RAD3200, from Scanivalve Corp.). The blow-down facility could maintain steady flow in the cascade for about 1 minute for Ma# 0.7 case, 40 and 15 seconds for Ma# 0.9 and 1.1 tests respectively. **Fig7** displays exit Mach number calibration results for all interested Mach numbers. A 30 second average and maximum exit Mach number are calculated. Time delay is defined as the duration between the instances that flow starts to reaches the target exit Mach number. The actual data starting time for PSP and LC are both 2 seconds after the mainstream flow started, which is very close to the time delay for flow to reach interested region. And the data acquisition durations for PSP and LC are 10 and 20 seconds respectively. In these time intervals, the exit flow velocities are still considered reasonably in steady and stable condition.

Before applying PSP/ LC to the test blade, it is coated with plain black base paint. The black paint acts as a binder for PSP/ LC. The neighboring vanes and the passages are also sprayed black to minimize stray reflection.

Pressure Sensitive Paint Instrumentation; On top of the black base paint, the blade is then sprayed with 6-8 coats of PSP (Uni-FIB UF470) using an air brush. A strobe light (PerkinElmer MVS-7000 Series) combined with a narrow band-pass interference filter (optical wavelength=520nm) is employed as the illumination source. The exciting light is directed on to the vane surface by a pair of flexible dual fiber-optic guides.

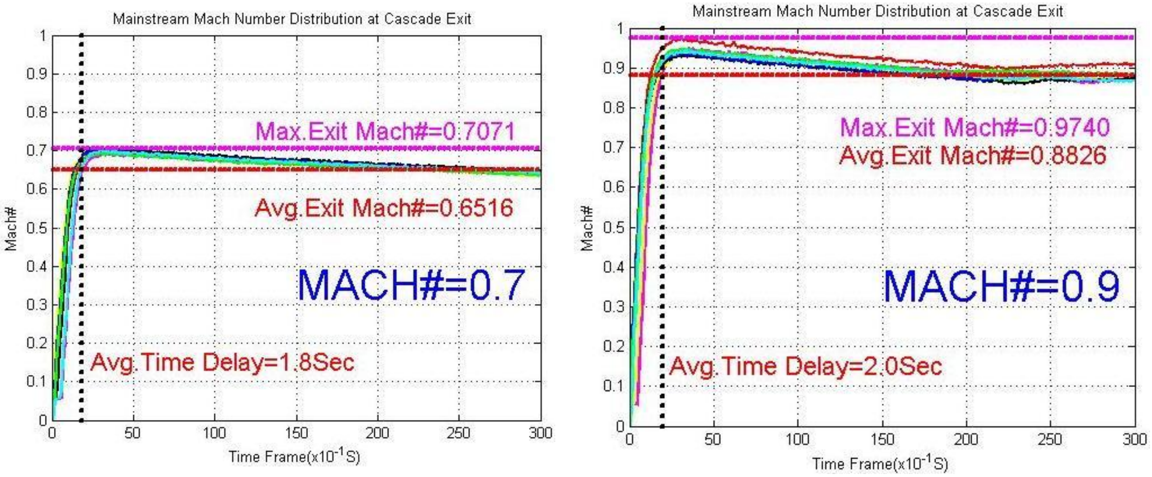

(a) Mach#=0.7 **(b) Mach#=0.9**

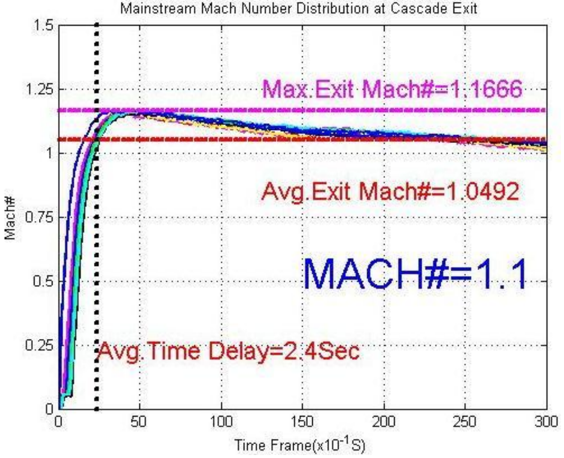

(c) Mach#=1.1

Figure 7 Real time exit Mach number calibration results

Upon excitation, the PSP coated surface emission range is above 600nm in wavelength. A 12-bit scientific grade CCD camera (Cooke Sensicam QE with CCD temperature maintained at -15°C using 2-stage peltier cooler), fitted with a 35mm lens and a 600nm long-pass filter, captures the surface emission intensity. The filter mounted on the camera is chosen such that no reflected light from the excitation source is able to pass through. The resolution obtained from the camera is 0.1mm/pixel.

The camera and the strobe light triggers are synchronized by TTL signal from a function generator, and the data acquisition 10 Hz. A total of 100 TIF images are captured and ensemble-averaged to get the emission intensity. In-house computer programs convert intensity into pressure and then to film-cooling effectiveness.

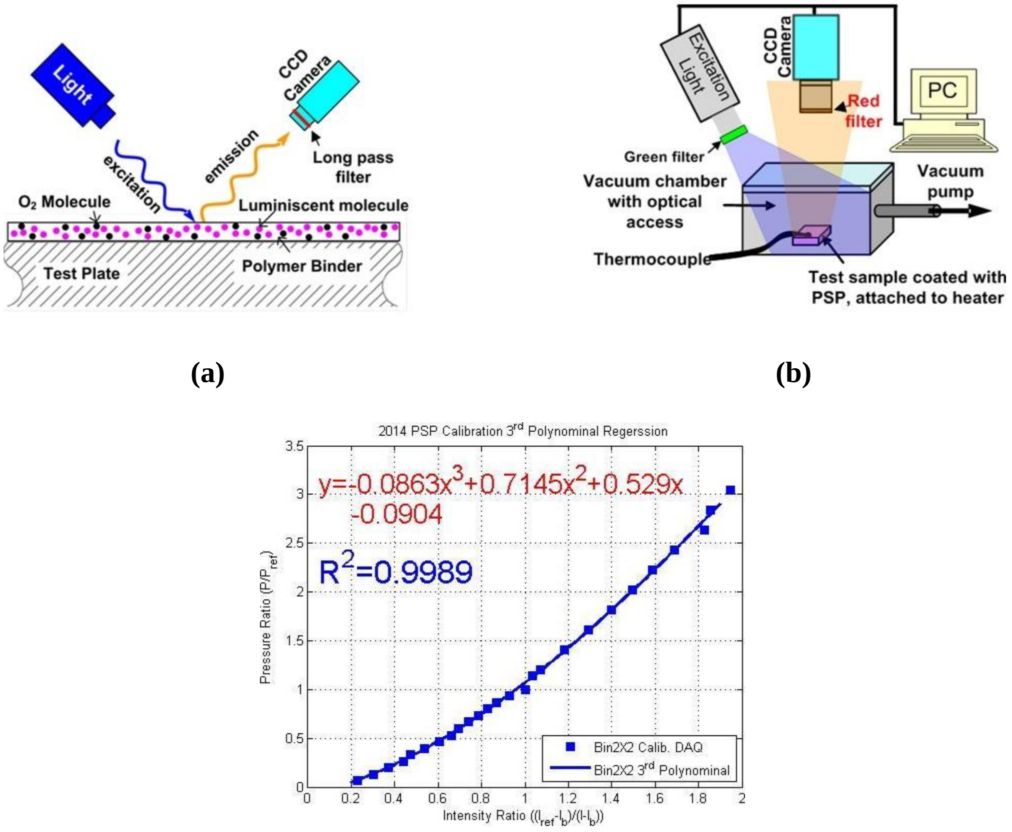

(a)

(b)

(c)

Figure 8 PSP working principle, calibration line

II.C.3. Pressure Sensitive Paint

II.C.3.1. Measurement Theory

In this study, pressure sensitive paint (PSP, UniFIB UF-470-750 from ISSI Inc.) technique is employed to obtain surface pressure data. A basic PSP system is shown in **Fig. 8(a)**. The test surface is sprayed with a layer of PSP and the PSP is composed of photo-luminescent molecules with oxygen-permeable polymer binder dissolved in a solvent.

When PSP excited by the green region of the spectrum (520 nm and a bandwidth of 20 nm), the PSP emits in the red region (>600nm). The exited electrons of photo-luminescent molecules emit a photon in the spectrum to fall back to their degenerate state. Another radiation-free path to the degeneration state is due to interaction with oxygen molecules. This phenomenon is known as oxygen quenching. The intensity of the emission decreases with the increase in oxygen concentration (i.e. partial pressure) adjacent to the PSP painted surface. McLachlan [34] documented detailed information on employing PSP technique for pressure measurements.

II.C.3.2. Calibration of Pressure Sensitive Paint

Fig 8(b) illustrated a schematic view of the PSP calibration setup. Upon the stainless steel (1 inch wall thickness) pressure chamber, a transparent viewing window is tightly mounted to provide optical access and maintain pressure level. PSP painted specimen (1×3 inches, identical material with SLS test vane) located in vacuum vessel is excited by the strobe light. Calibration is performed at several absolute pressure levels ranging from 0 to 3.0 atm, which fully covered the range expected during the experiments. The surface emission is recorded by a scientific grade CCD camera equipped with a red-filter (to ensure none of the exciting green light is captured) as gray-scale images and saved as TIFF files. The intensity of the emitted light (after correction for the background noise) is related to the partial pressure of oxygen surrounding the painted surface and is written as:

$$(1)\ \frac{I_{ref}-I_{blk}}{I-I_{blk}} = f\left(\frac{(P_{O_2})}{(P_{O_2})_{ref}}\right) = K_3(P_{ratio})^3 + K_2(P_{ratio})^2 + K_1(P_{ratio})^1 + K_0$$

In **Eq.1**, I_{ref} denotes the 'reference' intensity, typically corresponding with images acquired at atmospheric conditions. The corresponding (atmospheric pressure) is given by P_{ref}, and the atmospheric oxygen partial pressure is given by $P_{O2,ref}$. I_{blk} is the 'dark' intensity, it represents the back ground noise of the CCD camera. This corresponds with images acquired in a dark room condition. The term I represented the intensities acquired during the actual calibration with respect to all different pressure levels (P, pressure and vacuum) other than atmospheric. For simplicity, by least square method, a 3rd order polynomial regression model between the pressure ratio (P/P_{ref}) and intensity ratio ($(I_{ref}-I_{blk})/(I-I_{blk})$) is constructed. K_3, K_2, K_1 and K_0 represent constants of the third order polynomial regression.

One T-type thermocouple is mounted on the PSP coated side to record the temperature. Calibration temperature is controlled within PSP experiment operation range (23~25°C). The emitted light intensity by the pressure sensitive paint depends on both, the partial pressure of oxygen as well as the temperature of the surface. Since the experiment flow temperature variation is small (within 2°C) and the time duration is short (less than 15 seconds). The temperature dependency can be neglected in this PSP study.

Fig 8(c) shows the PSP calibration results of this study. Most of the data points collide with the 3^{rd} order polynomial model well. And the goodness of curve fitting R^2 is 0.9989.

II.D. Data Reduction

II.D.1. Film Cooling Effectiveness

Continuing from intensity ratio defined in the PSP calibration section, for every individual case, four images needed to determine the corresponding film cooling effectiveness. A dark image (with absence of excitation, mainstream flow, and coolant jets), a reference image (with absence of coolant jets), an air injection image (compressed air as coolant jet), and a foreign gas image (foreign gas as coolant jet); these four images constitute a complete set of information.

The compressed air injection image contains surface static pressure information and an oxygen-free foreign gas (N_2, CO_2, and $Ar+SF_6$ mixture) makes up the other coolant. The foreign gas mixes with or substitute air molecules (O_2 partial pressure) on the PSP coated surface leading to a change in emission intensity. By noting the difference in emitted intensity (O_2 partial pressure) between the air and foreign gas cases, film-cooling effectiveness can be calculated. Base on the heat and mass transfer analogy, contributed by Nicoll [29] and Jones [35], the film cooling effectiveness can be expressed as a form of oxygen concentrations measured by PSP and is calculated using the following equation.

$$(2)\ \eta = 1 - \frac{1}{\left\{\left(\frac{P_{O_2,air}}{P_{O_2,mix}} - 1\right)\frac{W_{fg}}{W_{air}} + 1\right\}}$$

In the above equation, $P_{O2,air}$ and $P_{O2,mix}$ correspond with pressure calculated from the intensity fields measured by two different injected coolants. By definition, the film effectiveness distribute between 0 at far downstream of coolant injection and 1 inside the inject hole. The expression (**Eq. 2**) was originally invented by Charbonnier et al. [36], and has been used by Nazarary et al. [37]. In the special case where the molecular weight of the foreign gas is similar to that of air (e.g. nitrogen injection), the above equation can be further simplified to:

$$(3)\ \eta = 1 - \frac{P_{O_2,mix}}{P_{O_2,air}}$$

II.D.2. Blowing Ratio

The PSP technique was used to measure mainstream partial oxygen pressure (static pressure) along the vane suction side surface. A pressure tap and a T-type thermal couple were installed downstream of all rotameters to provide actual flow rate (density) correction information. Using these information both mainstream and coolant densities can be determined by applying ideal gas law. The blowing ratio is defined as the ratio between products of coolant density, coolant volumetric flow rate divided by total cooling area and product of mainstream velocity and density.

$$(4)\ M = \frac{\left(\frac{\dot{m}}{A}\right)_c}{\rho_m V_m} = \frac{\left(\frac{\rho_c Q_c}{A_h n}\right)}{\rho_m V_m} = \frac{\rho_c V_c}{\rho_m V_m}$$

Mach number is calculated by the local static pressure (measured by PSP) and exit total pressure (measured by Pitot-static probe). The coolant supply is a trial and error process during the pretest configuration calibration for each and every parameter setup. **Fig 9** depicts the iteration process loop used throughout this study.

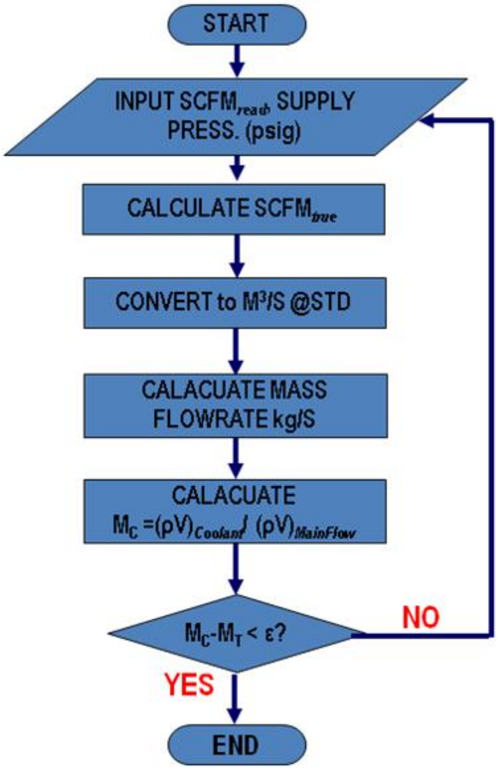

Figure 9 Coolant quantity monitor process

II.E. Experiment Condition

A total of 40 (36 set of PSP, 4 sets of LC) sets of experiments are performed to study the effects of exit Mach number ($Ma_{\#}$), blowing ratio (M), and density ratio (DR) on vane suction side effectiveness and heat transfer coefficients. Three Mach numbers– 0.7, 0.9, and 1.1; four average blowing ratios– 0.7, 1.0, 1.3, and 1.6; three density ratios- 1.1, 1.5, and 2.0 are selected for PSP study (summarized in **Table 1**).

Table 1 Vane suction side PSP test matrix

Num	Ma	DR	M	Num	Ma	DR	M	Num	Ma	DR	M
P07-1	0.7	1.0	0.7	P09-1	0.9	1.0	0.7	P11-1	1.1	1.0	0.7
P07-2	0.7	1.0	1.0	P09-2	0.9	1.0	1.0	P11-2	1.1	1.0	1.0
P07-3	0.7	1.0	1.3	P09-3	0.9	1.0	1.3	P11-3	1.1	1.0	1.3
P07-4	0.7	1.0	1.6	P09-4	0.9	1.0	1.6	P11-4	1.1	1.0	1.6
P07-5	0.7	1.5	0.7	P09-5	0.9	1.5	0.7	P11-5	1.1	1.5	0.7
P07-6	0.7	1.5	1.0	P09-6	0.9	1.5	1.0	P11-6	1.1	1.5	1.0
P07-7	0.7	1.5	1.3	P09-7	0.9	1.5	1.3	P11-7	1.1	1.5	1.3
P07-8	0.7	1.5	1.6	P09-8	0.9	1.5	1.6	P11-8	1.1	1.5	1.6
P07-9	0.7	2.0	0.7	P09-9	0.9	2.0	0.7	P11-9	1.1	2.0	0.7
P07-10	0.7	2.0	1.0	P09-10	0.9	2.0	1.0	P11-10	1.1	2.0	1.0
P07-11	0.7	2.0	1.3	P09-11	0.9	2.0	1.3	P11-11	1.1	2.0	1.3
P07-12	0.7	2.0	1.6	P09-12	0.9	2.0	1.6	P11-12	1.1	2.0	1.6

II.F. Results and Discussions

II.F.1. Mach Number Distribution

Mainstream velocity is monitored by a Pitot-static tube at 0.75 chord length downstream vane cascade. **Fig 10** displays the real time exemplary cases exit velocity and Pitot-Static tube data for Mach number 0.7, 0.9 and 1.1.

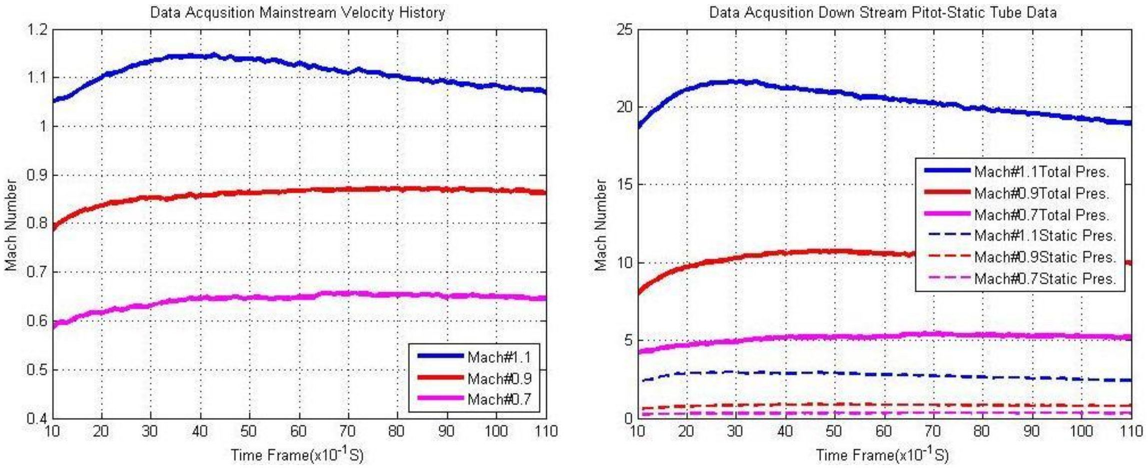

(a) Mainstream Velocity

(b) Total and static pressure at cascade exit

Figure 10 Real time exit Mach number results for exemplary cases

Local Mach number distribution can be evaluated by using PSP images of compressed air coolant cases. Mainstream air enters the test section with a relatively low bulk velocity, as it travels through the vane cascade it accelerated till the exit velocity become supersonic (Mach number = 1.1), shockwaves take place and affect the film cooling effectiveness. Mach number distribution for three different exit Mach numbers (Ma=0.7, 0.9, and 1.1) and blowing ratios 0.7, 1.0, 1.3, and 1.6 are plotted in **Figs 11, 12, 13** and **14** respectively. By distinguishing the discontinuous velocity contour region, one can indicate the locations of potential shockwave. Dotted lines represent the approximate cooling row locations on the suction side surface.

As mentioned earlier, the visual data coverage is roughly 60% of the van suction side surface due to limitation from viewing window. The contour figures were transformed from 3D (actual data image) to 2D (polar form) by in-house code to provide information in more detail. The abscissa and the ordinate of all contours are normalized with actual surface length (X/L) and vane height (y/H), respectively.

The brown color in the contours denotes the locations for flow Mach number close to unity. Although the value maybe magnified since using the cascade downstream total pressure and local static pressure for Mach number reference. The contours still provide a reasonable indication for potential shock regions. For Mach 1.1 cases, regardless the blowing ratio, shock waves started to take place at the suction side of vane surface at suction side second row (SS2) cooling hole. It is worthy to point out that in some high blowing ratios cases under Ma= 0.9 mainstream, there are potential shock regions around SS2 neighborhood. This may due to the contribution of SS2 coolant jets momentum.

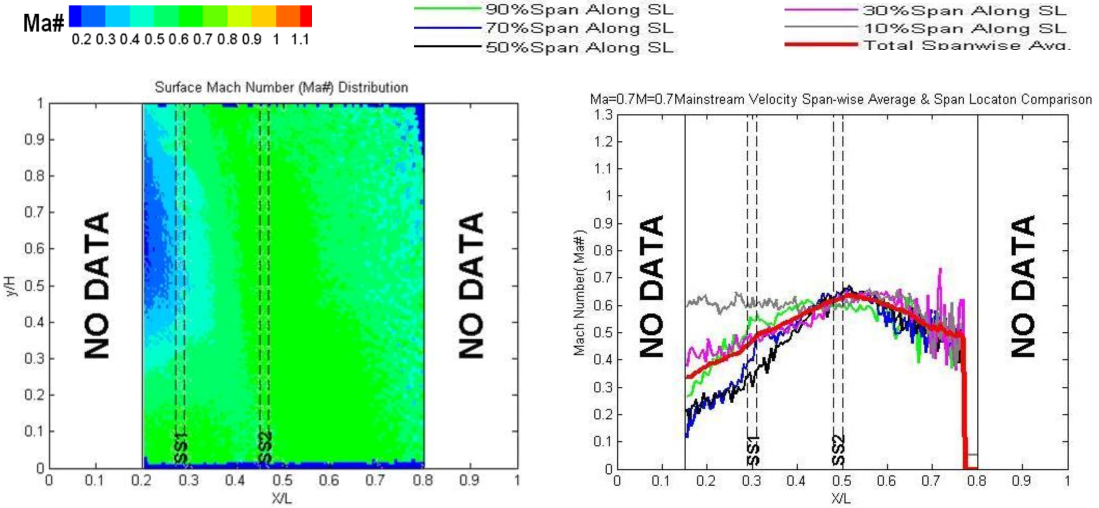

(a) Ma=0.7 Surface contour

(b) Ma=0.7 Span-wise average

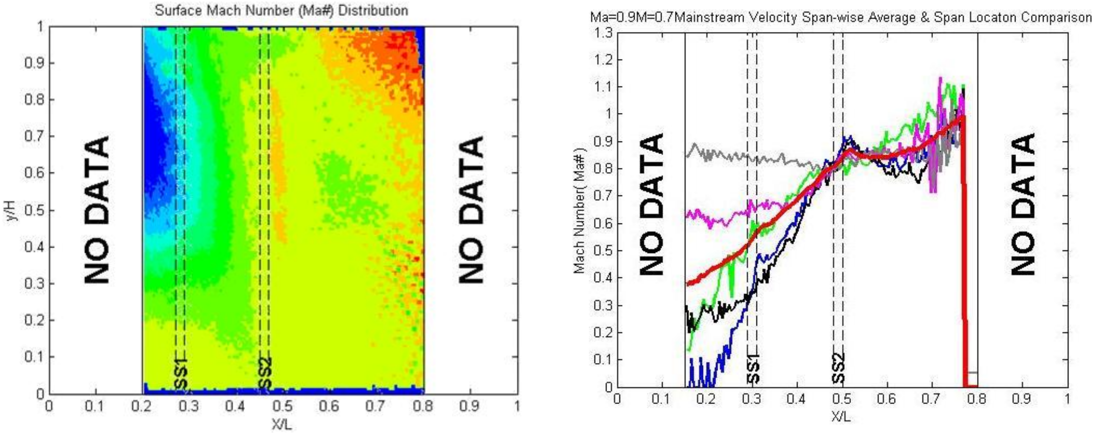

(c) Ma=0.9 Surface contour

(d) Ma=0.9 Span-wise average

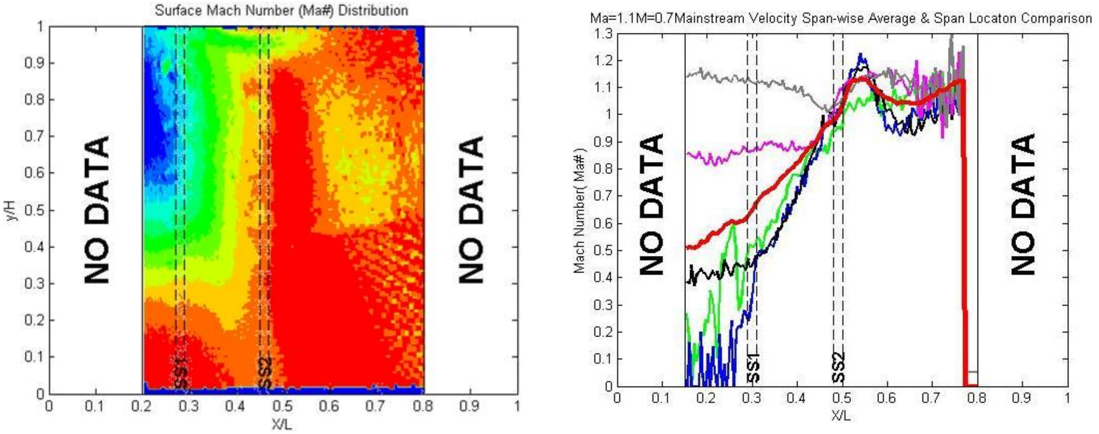

(e) Ma=1.1 Surface contour

(f) Ma=1.1 Span-wise average

Figure 11 Surface Mach number distribution for M=0.7

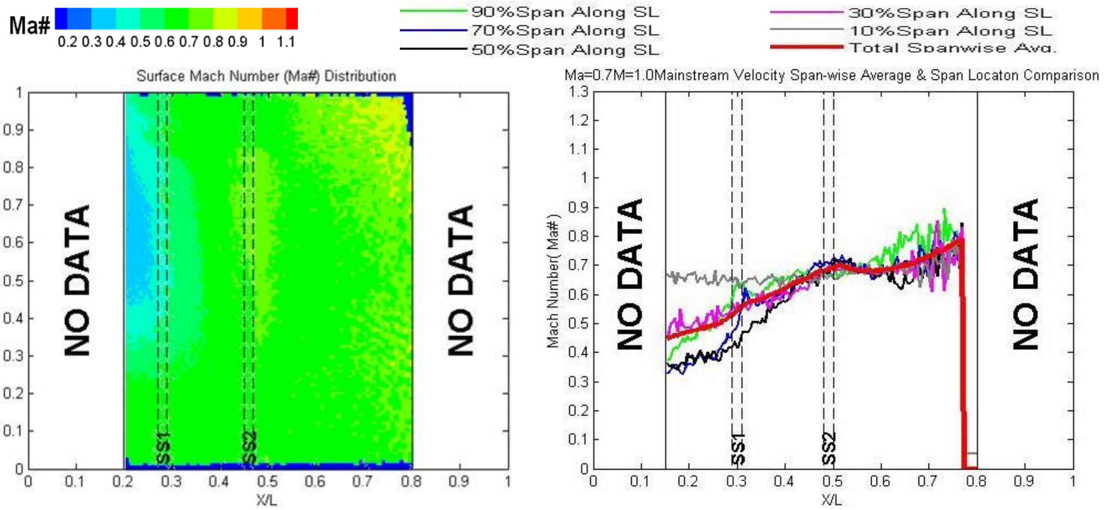

(a) Ma=0.7 Surface contour (b) Ma=0.7 Span-wise average

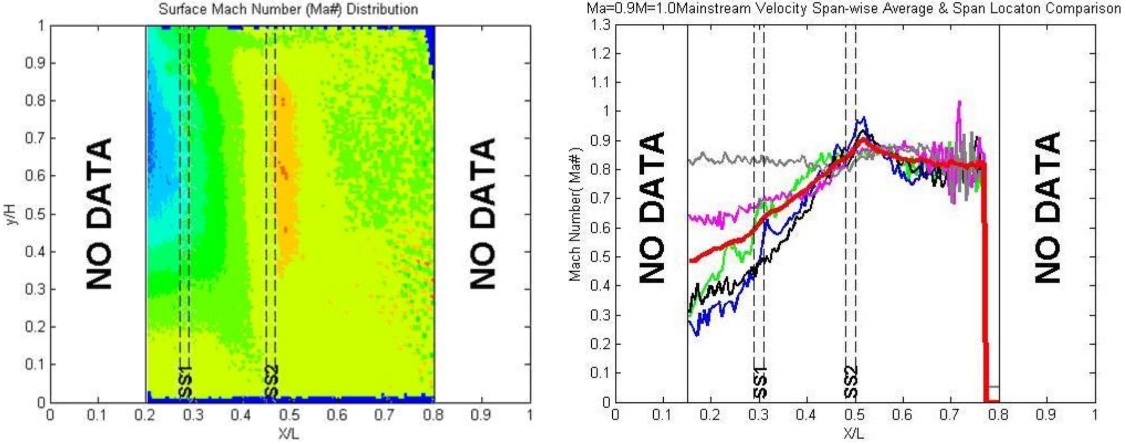

(c) Ma=0.9 Surface contour (d) Ma=0.9 Span-wise average

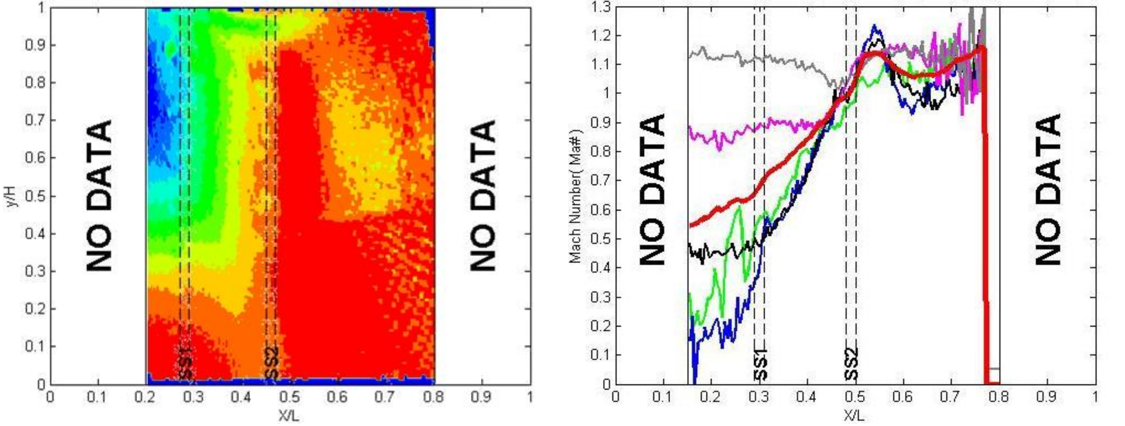

(e) Ma=1.1 Surface contour (f) Ma=1.1 Span-wise average

Figure 12 Surface Mach number distribution for M=1.0

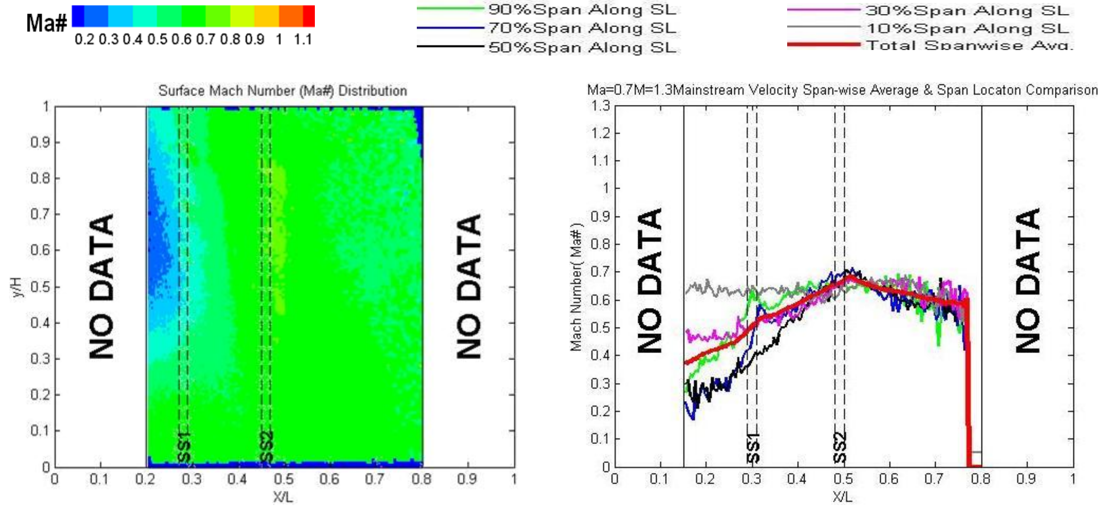

(a) Ma=0.7 Surface contour (b) Ma=0.7 Span-wise average

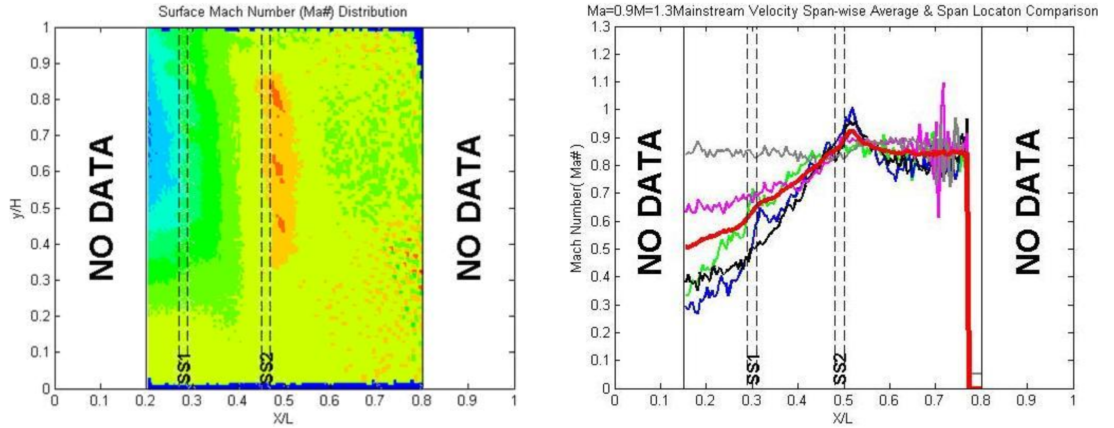

(c) Ma=0.9 Surface contour (d) Ma=0.9 Span-wise average

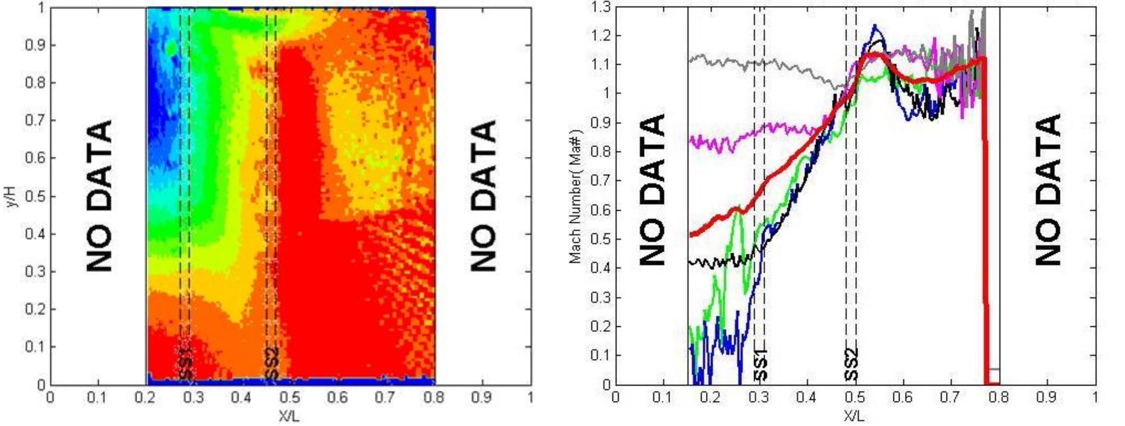

(e) Ma=1.1 Surface contour (f) Ma=1.1 Span-wise average

Figure 13 Surface Mach number distribution for M=1.3

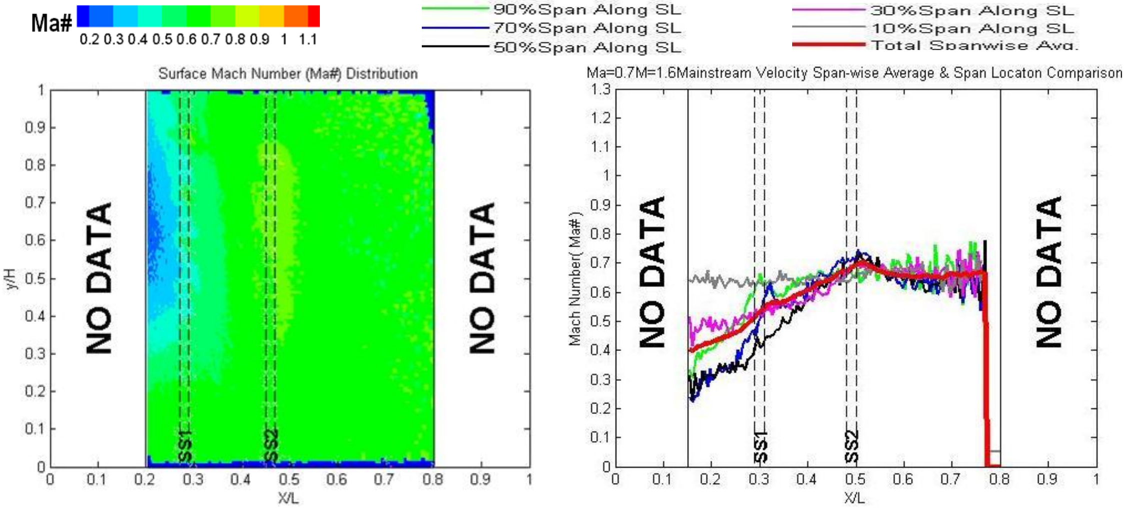

(a) Ma=0.7 Surface contour (b) Ma=0.7 Span-wise average

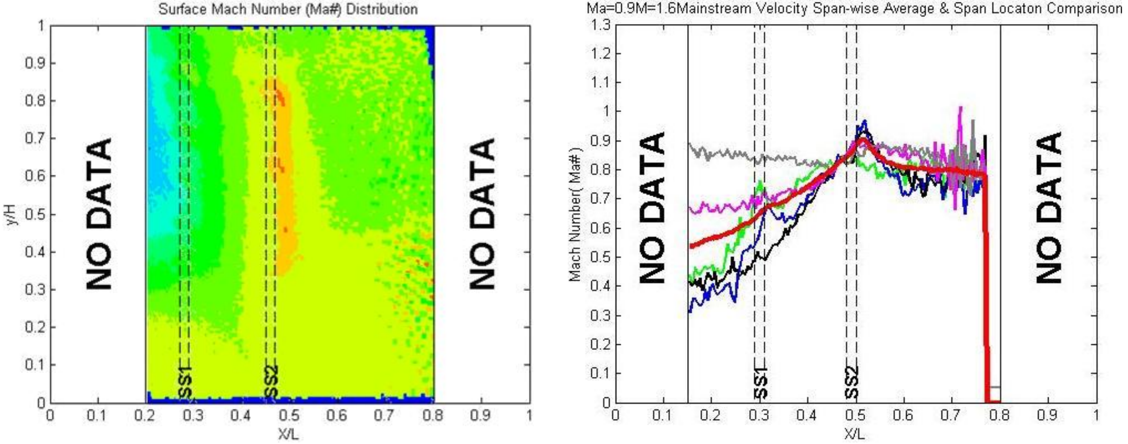

(c) Ma=0.9 Surface contour (d) Ma=0.9 Span-wise average

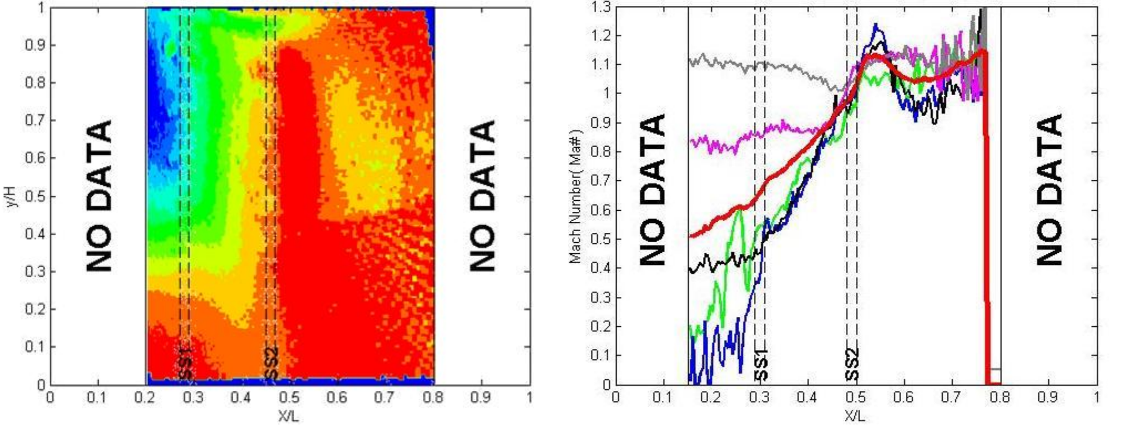

(e) Ma=1.1 Surface contour (f) Ma=1.1 Span-wise average

Figure 14 Surface Mach number distribution for M=1.6

At the right hand side of **Figs 11, 12, 13, and, 14**, the line plots illustrated the Mach number span wise average and various span height comparison for the corresponding case. The height is measured as percentage of the total vane span from the hub and the direction is along the stream line. The figures indicates that the vane surface Mach number distribution started diversely at data start point, and collide together near SS2 neighborhood.

II.F.2. Adiabatic Film Cooling Effectiveness

The adiabatic film cooling effectiveness distribution for all studied cases is listed in **Figs 15** to **26**. The actual inject coolant amount is listed in Table 2. In general, in most of line plots, the film cooling effectiveness at 10% span is relatively less compared with the other positions. As mentioned before, there are seven compound shaped holes for each row. However, from the contour plots, there are usually six and four traces for SS1 and SS2 respectively in most of the results. Therefore one can conclude that the amount of coolant discharge from each of the holes of both SS1 and SS2 are not uniform.

This coolant trace non-uniformity from both SS1 and SS2 may partially attribute by horseshoe vortex near the hub region and partially caused by the coolant plenum/ passage design. As indicated in the line plots, the film cooling effectiveness at 70% and 90% of the y/H are the first and second highest in all studied cases. Current plenums length are 64 mm and cross section are similar with the coolant passages; this may aid coolant stagnation at the tip side of the passage thereby more coolant to discharge from the upper half of the coolant configuration. Effectiveness recorded at upstream SS1 is due to coolants carry over from the leading edge rows. Consider channel radial angle effect, more coolants are cumulated at vane upper portion.

Table 2 Actual and target blowing ratio comparison for all density ratios

Table 2 (a) Actual and target blowing ratio comparison for DR=1.0

LOCATION	TARGET BLOWING RATIO (M)	MACH#=0.7		MACH#=0.9		MACH#=1.1	
		ACTUAL M	ERROR (%)	ACTUAL M	ERROR (%)	ACTUAL M	ERROR (%)
Leading Edge	0.7	0.6908	-1.31	0.6842	-2.25	0.7160	2.29
	1.0	1.0588	5.88	0.9674	-3.26	1.0294	2.94
	1.3	1.2610	-3.00	1.3121	0.93	1.3405	3.12
	1.6	1.6233	1.45	1.6008	0.05	1.6589	3.68
Suction Side 1	0.7	0.6888	-1.59	0.7034	0.49	0.6869	-1.88
	1.0	1.0525	5.25	1.0111	1.11	1.0442	4.42
	1.3	1.2690	-2.38	1.3378	2.91	1.3097	0.75
	1.6	1.5761	-1.49	1.6109	0.68	1.6473	2.96
Suction Side 2	0.7	0.7133	1.90	0.6931	-0.98	0.7300	4.28
	1.0	1.0328	3.28	1.0095	0.95	1.0220	2.20
	1.3	1.3240	1.85	1.3283	2.18	1.3159	1.22
	1.6	1.6012	0.07	1.6153	0.96	1.6339	2.12

Table 2 (b) Actual and target blowing ratio comparison for DR=1.5

LOCATION	TARGET BLOWING RATIO (M)	MACH#=0.7		MACH#=0.9		MACH#=1.1	
		ACTUAL M	ERROR (%)	ACTUAL M	ERROR (%)	ACTUAL M	ERROR (%)
Leading Edge	0.7	0.6935	-0.92	0.7026	0.37	0.7058	0.83
	1.0	1.0147	1.47	1.0330	3.30	1.0731	7.31
	1.3	1.3319	2.45	1.2934	-0.51	1.3137	1.06
	1.6	1.5850	-0.94	1.7482	9.26	1.6096	0.60
Suction Side 1	0.7	0.7184	2.63	0.7334	4.77	0.6858	-2.03
	1.0	1.0238	2.38	0.9514	-4.86	1.0434	4.34
	1.3	1.3040	0.31	1.2682	-2.45	1.3582	4.47
	1.6	1.6524	3.28	1.6031	0.19	1.6138	0.86
Suction Side 2	0.7	0.7063	0.91	0.6995	-0.07	0.6949	-0.72
	1.0	1.0249	2.49	0.9748	-2.52	1.0611	6.11
	1.3	1.2982	-0.14	1.3173	1.33	1.3413	3.17
	1.6	1.6159	0.99	1.6205	1.28	1.6665	4.15

Table 2 (c) Actual and target blowing ratio comparison for DR=2.0

LOCATION	TARGET BLOWING RATIO (M)	MACH#=0.7		MACH#=0.9		MACH#=1.1	
		ACTUAL M	ERROR (%)	ACTUAL M	ERROR (%)	ACTUAL M	ERROR (%)
Leading Edge	0.7	0.7193	2.76	0.7037	0.53	0.7238	3.40
	1.0	1.0005	0.05	1.0745	7.45	1.0209	2.09
	1.3	1.3607	4.67	1.3207	1.59	1.3099	0.76
	1.6	1.6775	4.84	1.6206	1.29	1.6334	2.09
Suction Side 1	0.7	0.7150	2.15	0.7365	5.21	0.6955	-0.65
	1.0	0.9998	-0.02	0.9954	-0.46	1.0661	6.61
	1.3	1.3214	1.65	1.3496	3.81	1.2932	-0.52
	1.6	1.6213	1.33	1.6011	0.07	1.5894	-0.66
Suction Side 2	0.7	0.6567	-6.19	0.6884	-1.65	0.7394	5.63
	1.0	1.0364	3.64	0.9623	-3.77	1.0250	2.50
	1.3	1.3024	0.18	1.2614	-2.97	1.3284	2.19
	1.6	1.6604	3.78	1.6029	0.18	1.5834	-1.04

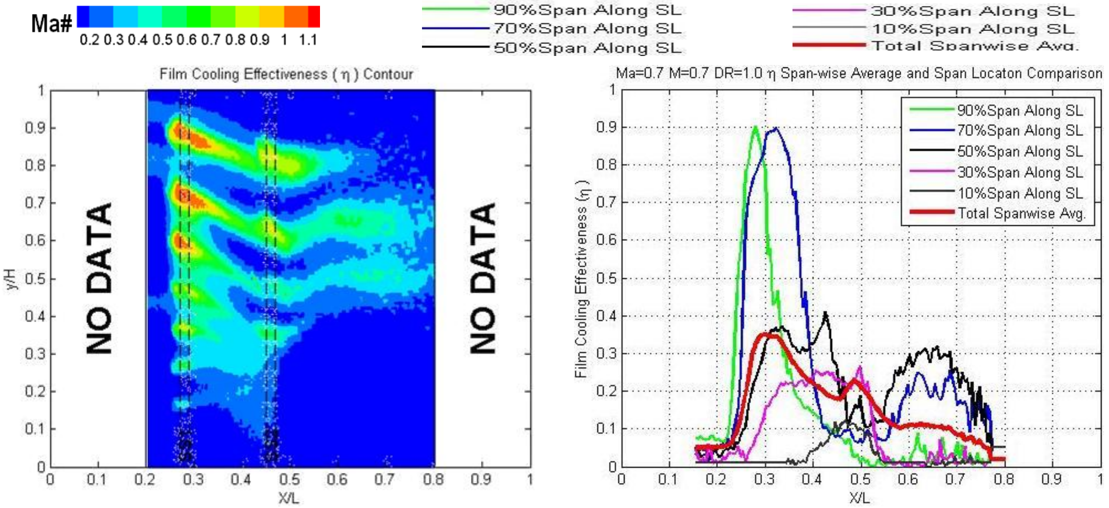

(a) Ma=0.7 Surface contour (b) Ma=0.7 Span-wise average

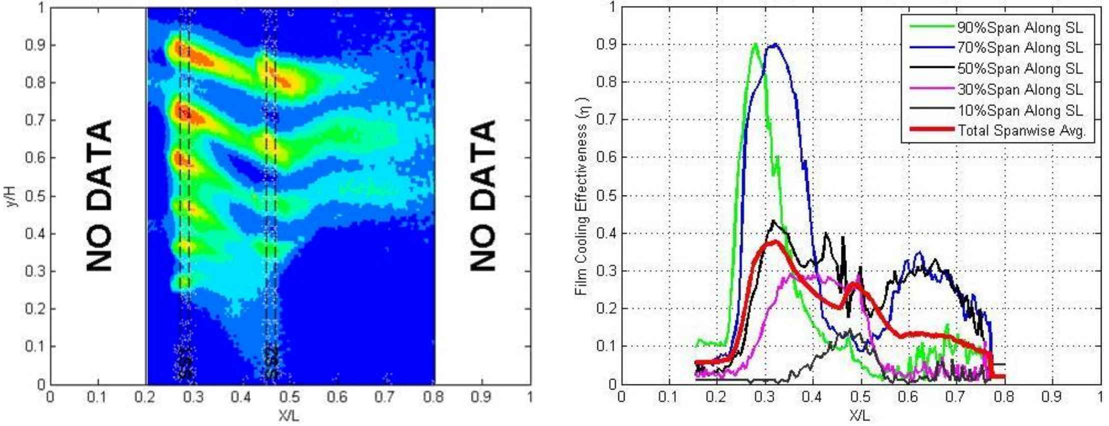

(c) Ma=0.9 Surface contour (d) Ma=0.9 Span-wise average

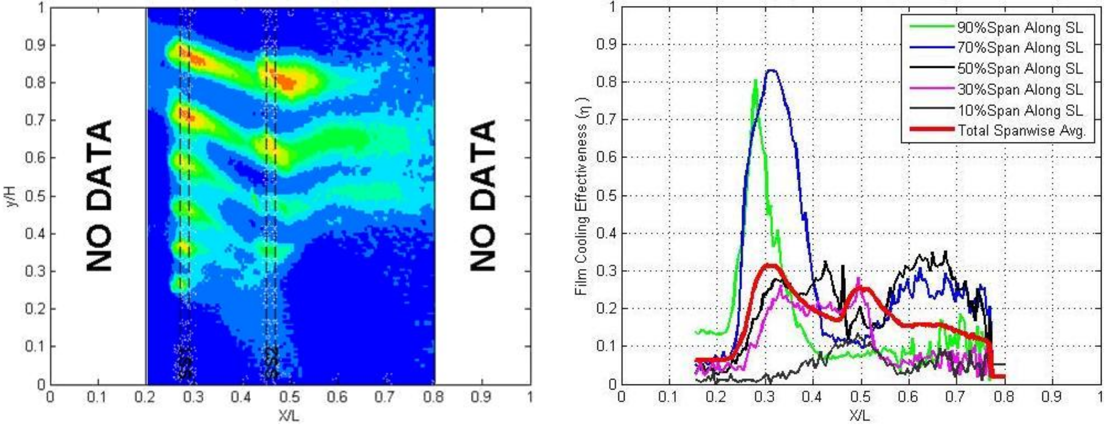

(e) Ma=1.1 Surface contour (f) Ma=1.1 Span-wise average

Figure 15 Film cooling effectiveness distribution for M=0.7 DR=1.0

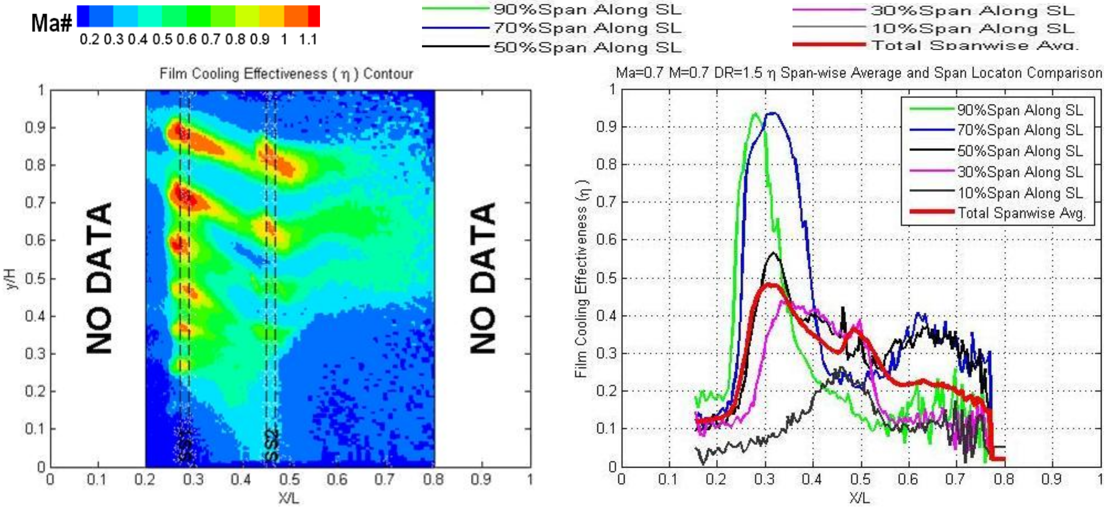

(a) Ma=0.7 Surface contour **(b) Ma=0.7 Span-wise average**

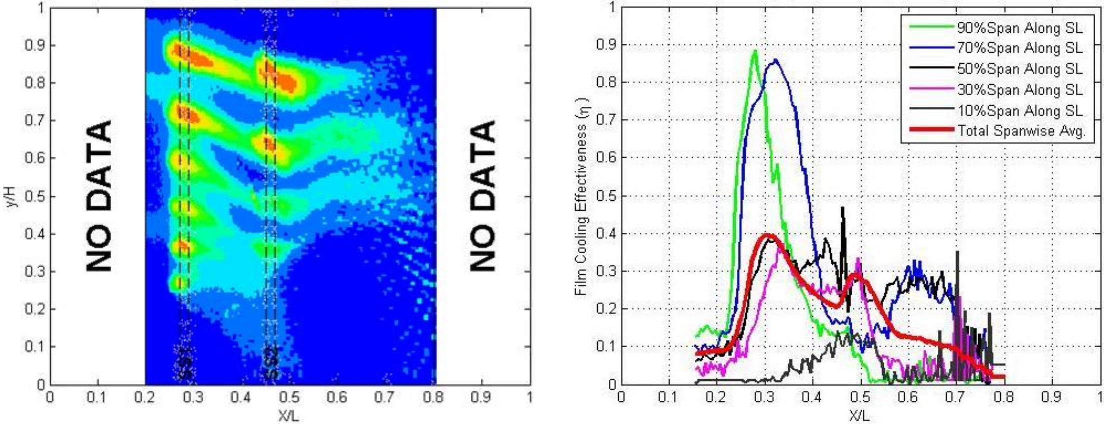

(c) Ma=0.9 Surface contour **(d) Ma=0.9 Span-wise average**

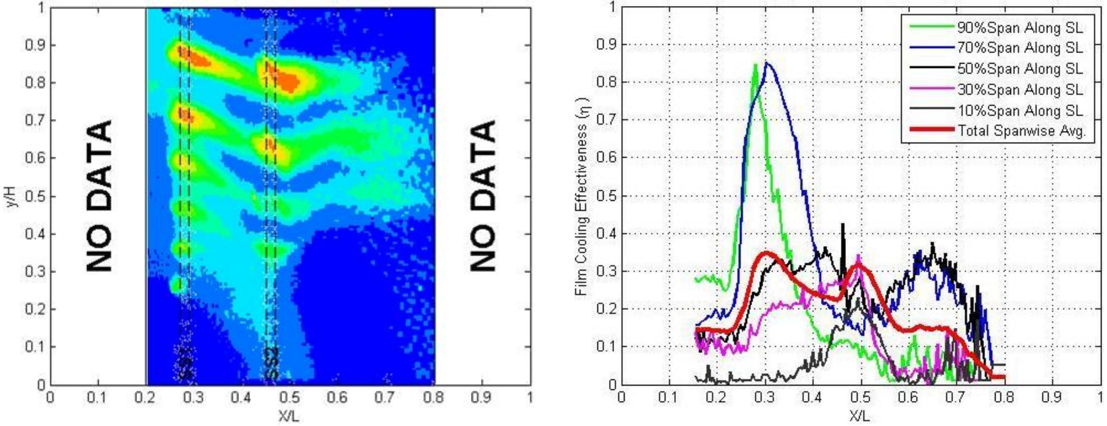

(e) Ma=1.1 Surface contour **(f) Ma=1.1 Span-wise average**

Figure 16 Film cooling effectiveness distribution for M=0.7 DR=1.5

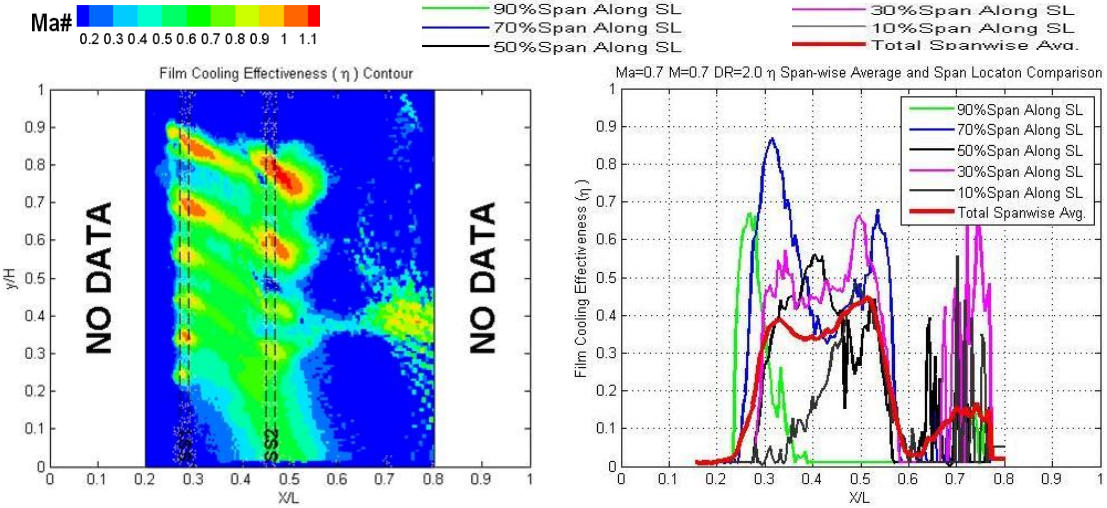

(a) Ma=0.7 Surface contour (b) Ma=0.7 Span-wise average

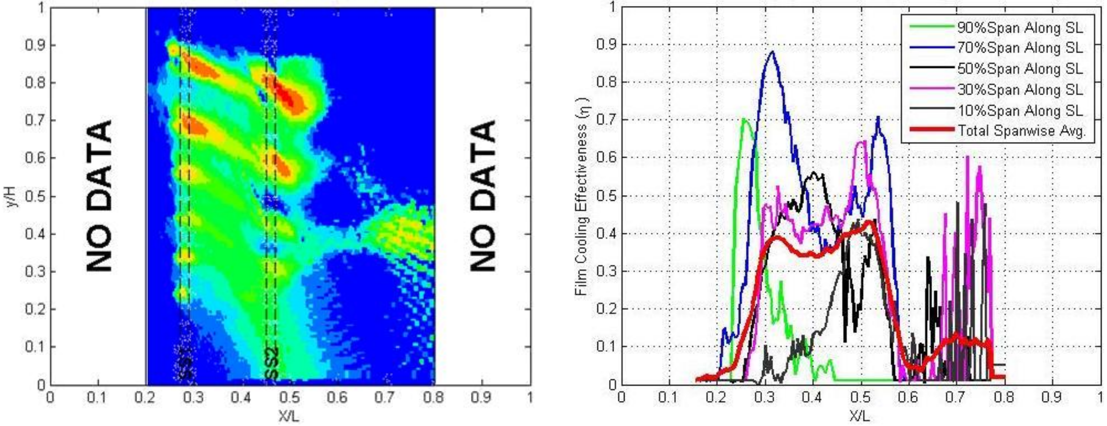

(c) Ma=0.9 Surface contour (d) Ma=0.9 Span-wise average

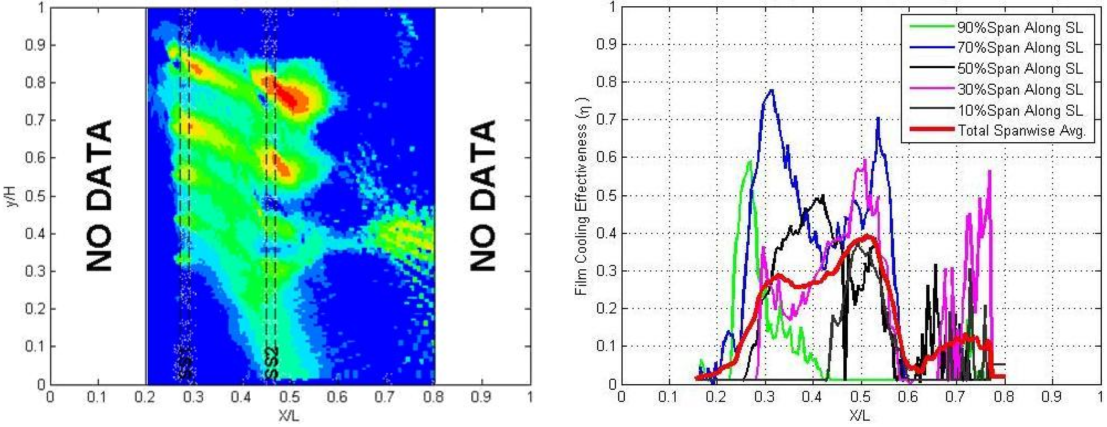

(e) Ma=1.1 Surface contour (f) Ma=1.1 Span-wise average

Figure 17 Film cooling effectiveness distribution for M=0.7 DR=2.0

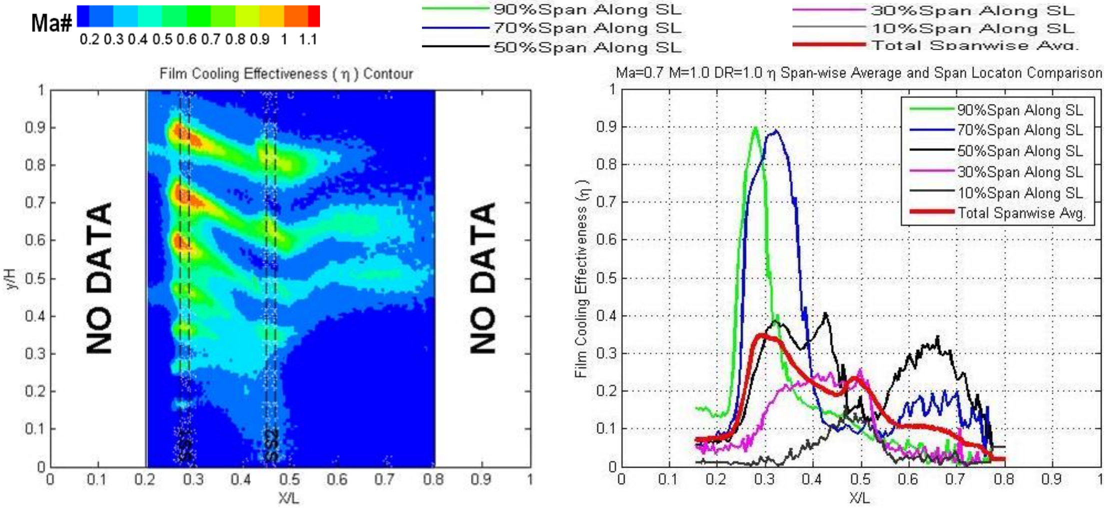

(a) Ma=0.7 Surface contour **(b) Ma=0.7 Span-wise average**

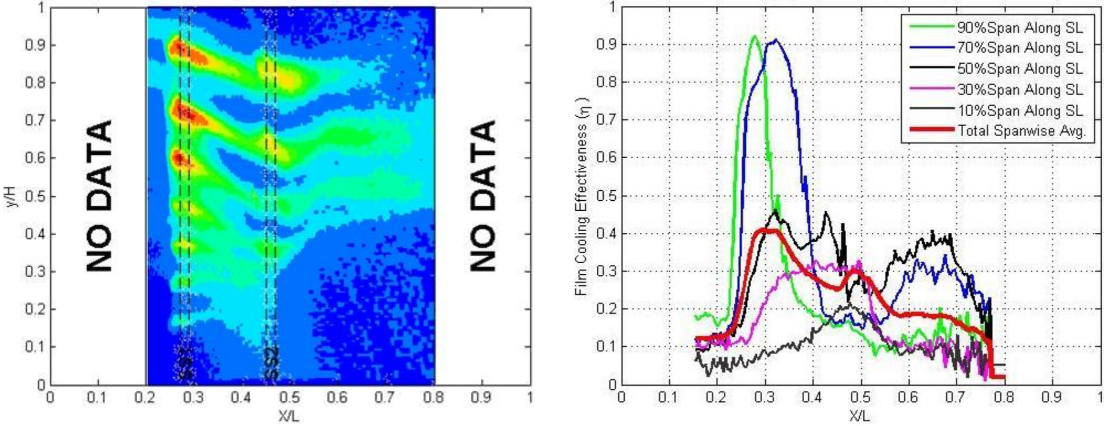

(c) Ma=0.9 Surface contour **(d) Ma=0.9 Span-wise average**

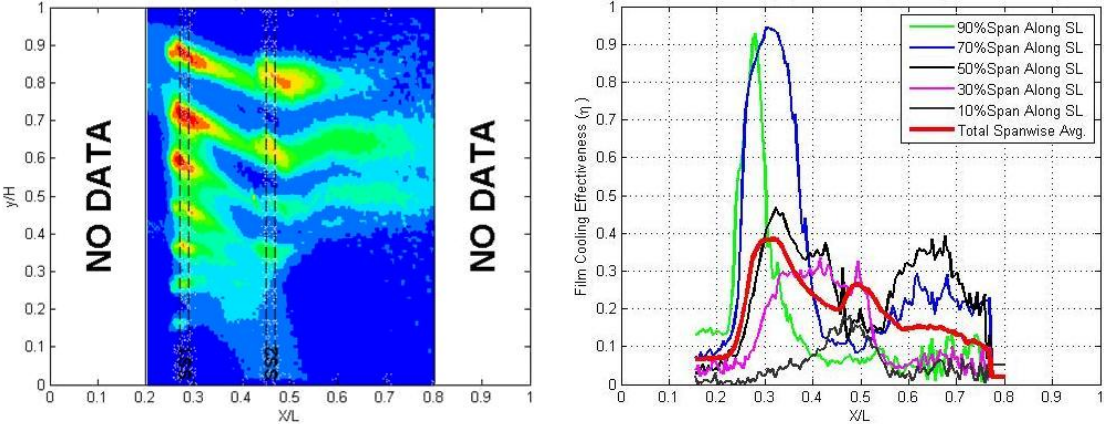

(e) Ma=1.1 Surface contour **(f) Ma=1.1 Span-wise average**

Figure 18 Film cooling effectiveness distribution for M=1.0 DR=1.0

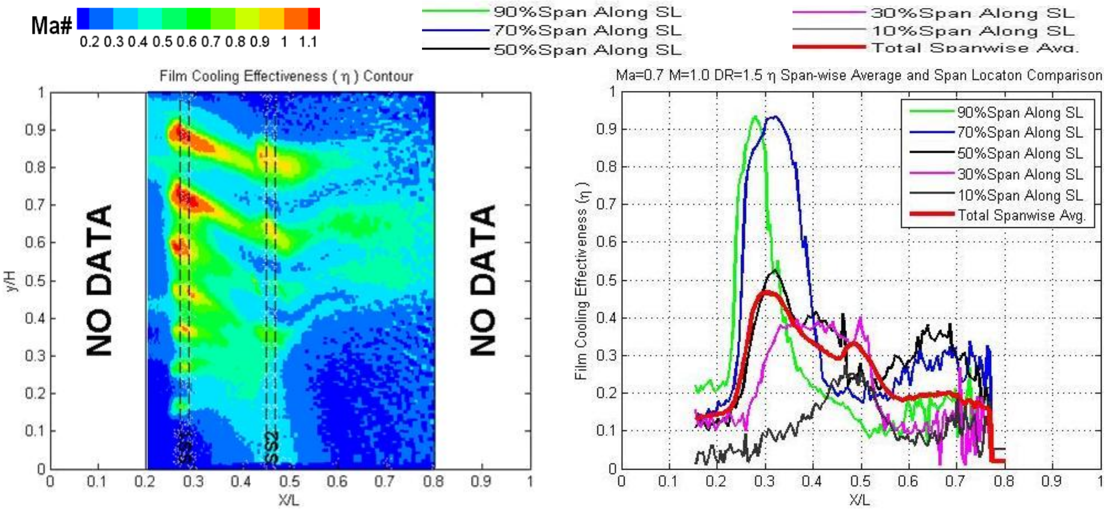

(a) Ma=0.7 Surface contour (b) Ma=0.7 Span-wise average

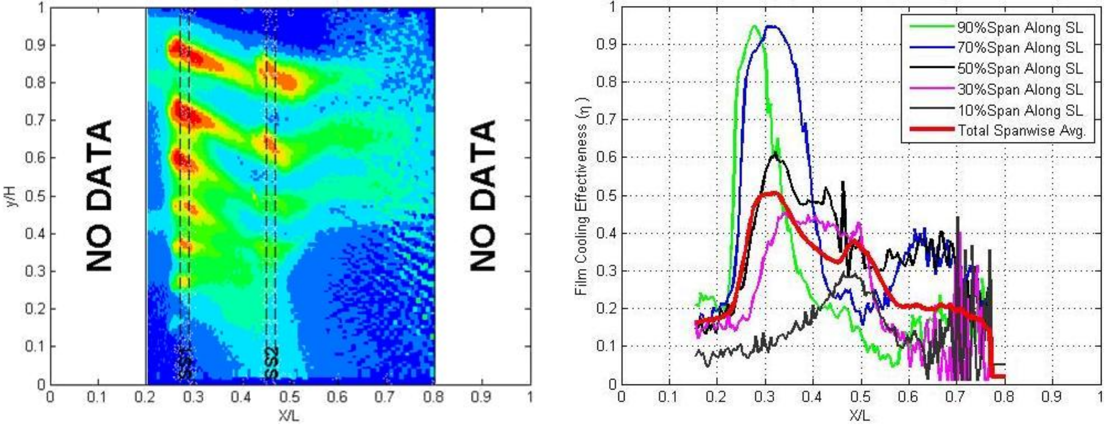

(c) Ma=0.9 Surface contour (d) Ma=0.9 Span-wise average

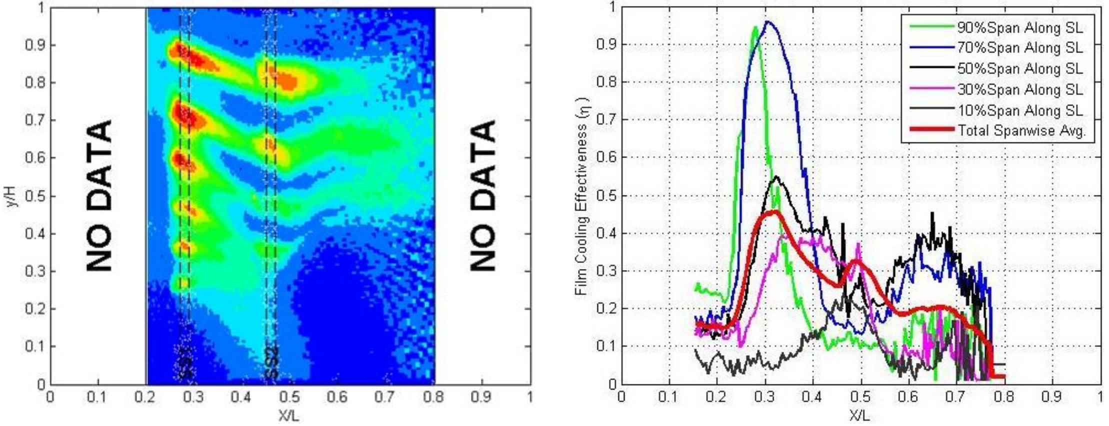

(e) Ma=1.1 Surface contour (f) Ma=1.1 Span-wise average

Figure 19 Film cooling effectiveness distribution for M=1.0 DR=1.5

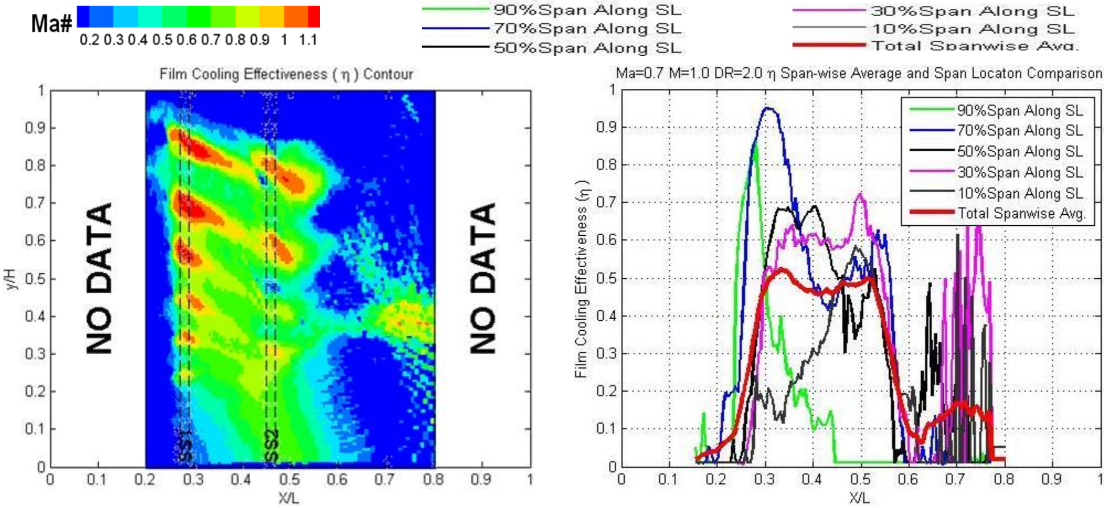

(a) Ma=0.7 Surface contour **(b) Ma=0.7 Span-wise average**

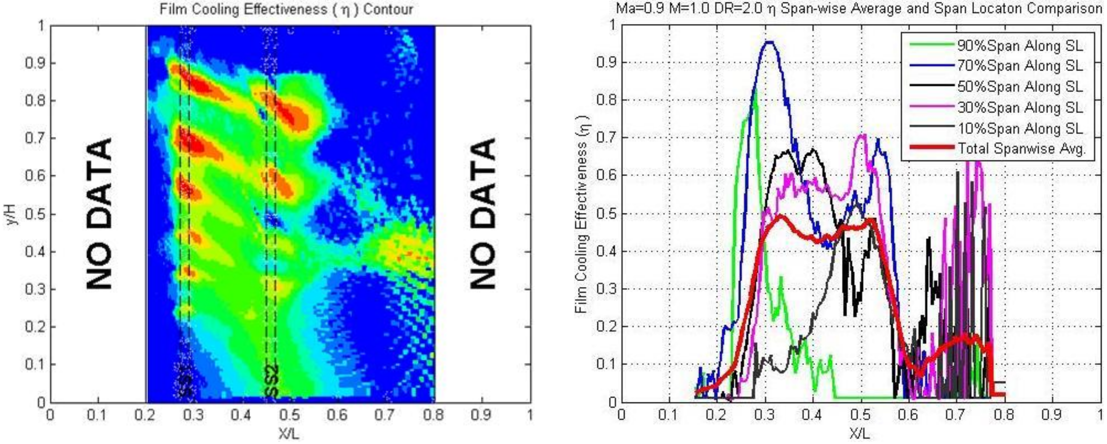

(c) Ma=0.9 Surface contour **(d) Ma=0.9 Span-wise average**

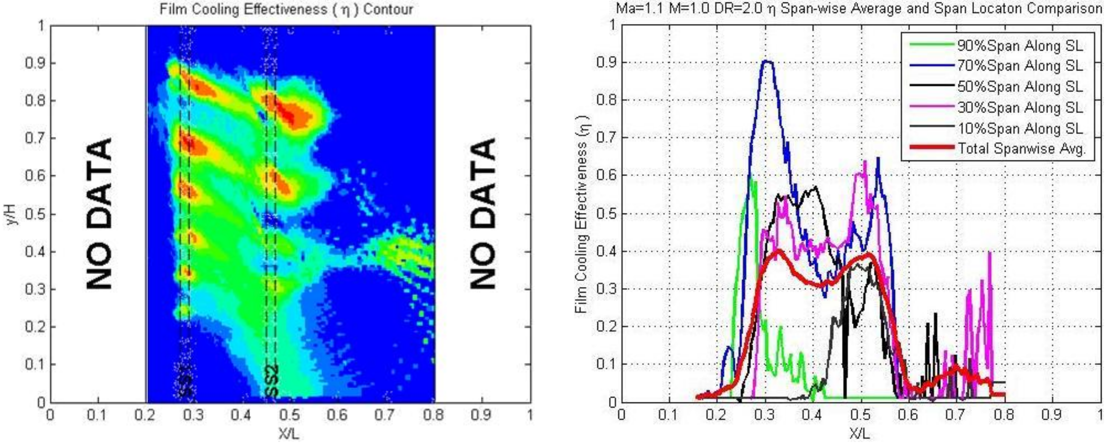

(e) Ma=1.1 Surface contour **(f) Ma=1.1 Span-wise average**

Figure 20 Film cooling effectiveness distribution for M=1.0 DR=2.0

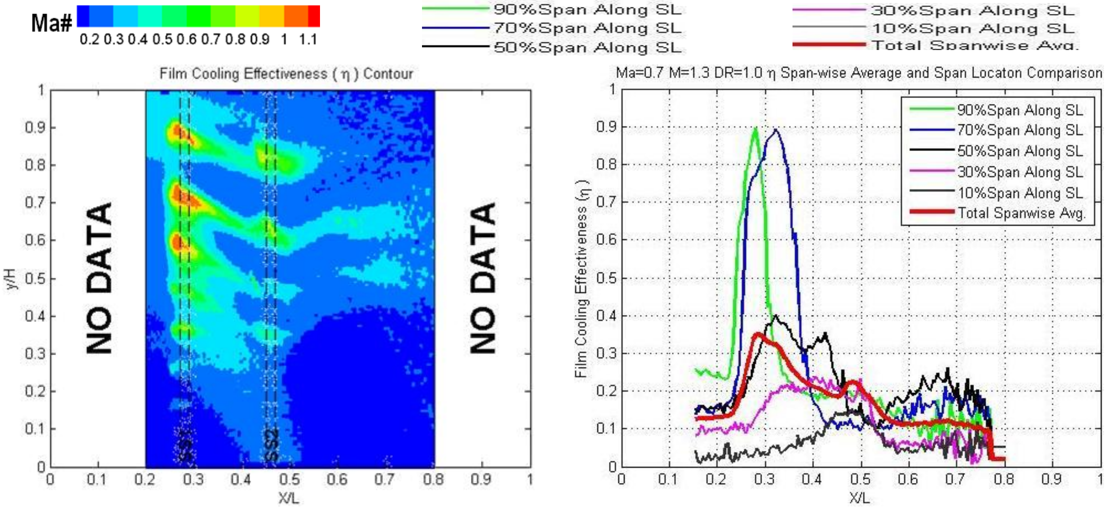

(a) Ma=0.7 Surface contour (b) Ma=0.7 Span-wise average

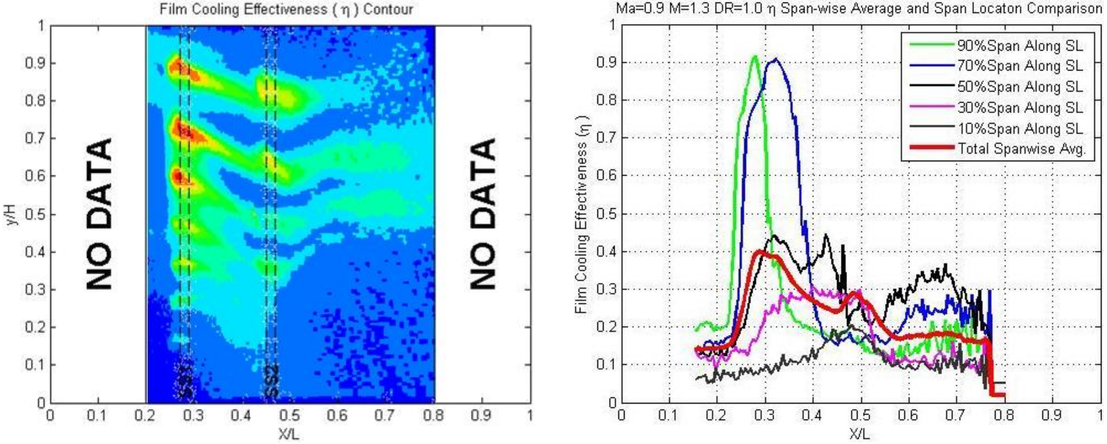

(c) Ma=0.9 Surface contour (d) Ma=0.9 Span-wise average

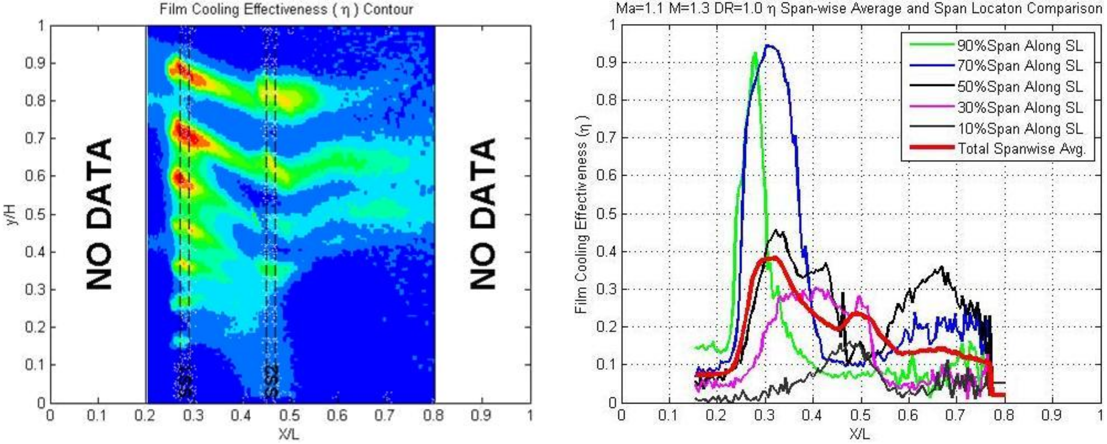

(e) Ma=1.1 Surface contour (f) Ma=1.1 Span-wise average

Figure 21 Film cooling effectiveness distribution for M=1.3 DR=1.0

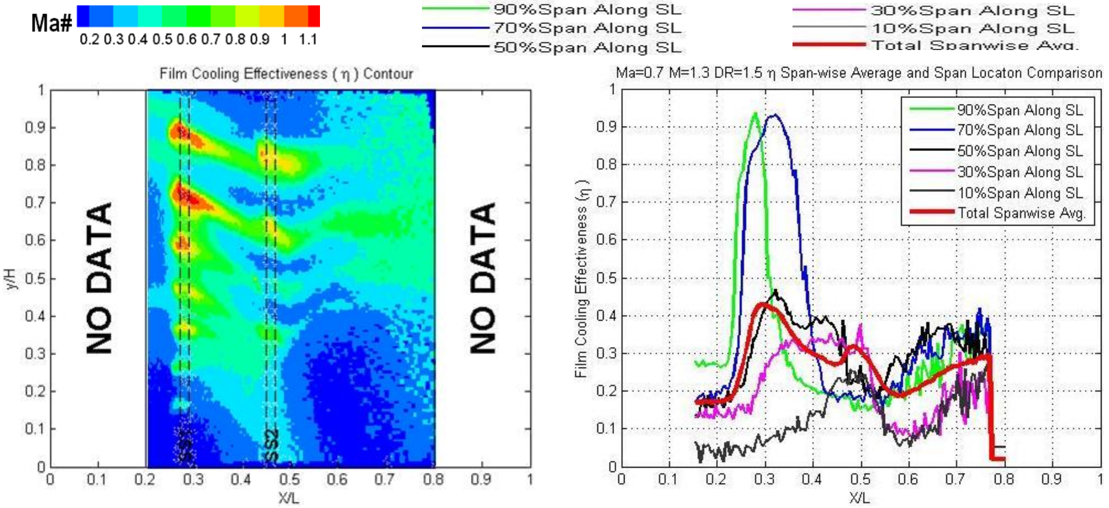

(a) Ma=0.7 Surface contour (b) Ma=0.7 Span-wise average

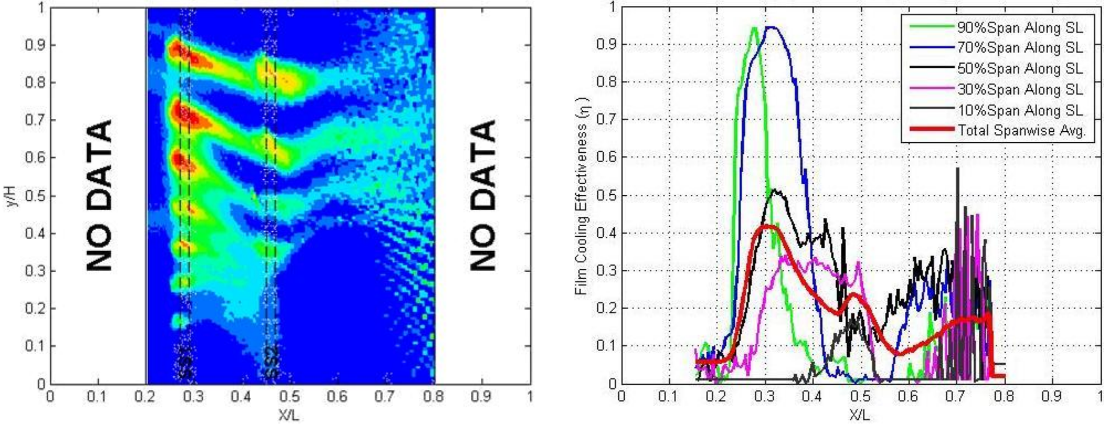

(c) Ma=0.9 Surface contour (d) Ma=0.9 Span-wise average

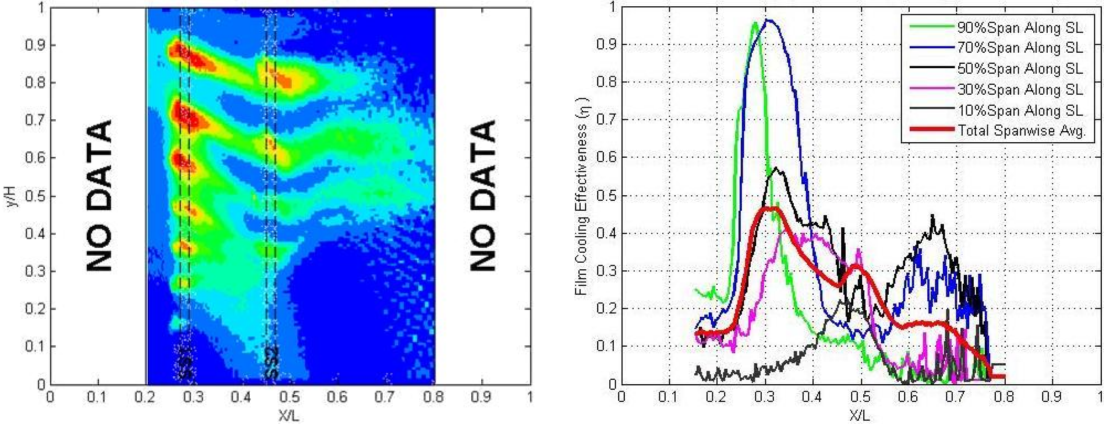

(e) Ma=1.1 Surface contour (f) Ma=1.1 Span-wise average

Figure 22 Film cooling effectiveness distribution for M=1.3 DR=1.5

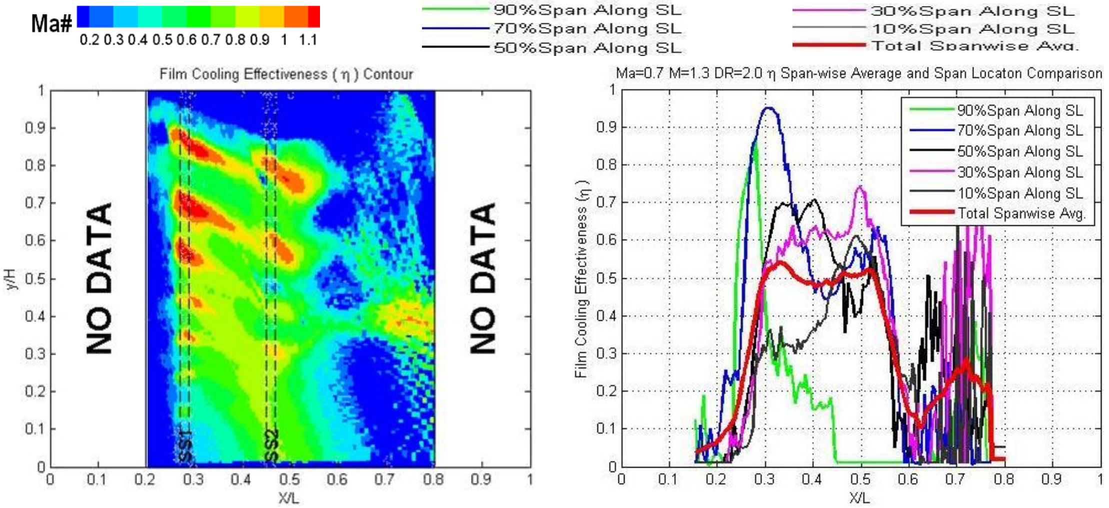

(a) Ma=0.7 Surface contour (b) Ma=0.7 Span-wise average

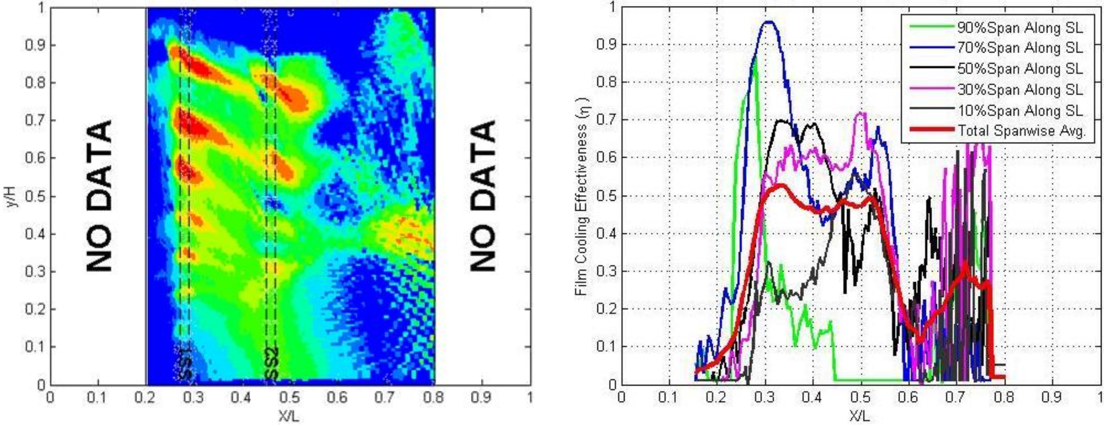

(c) Ma=0.9 Surface contour (d) Ma=0.9 Span-wise average

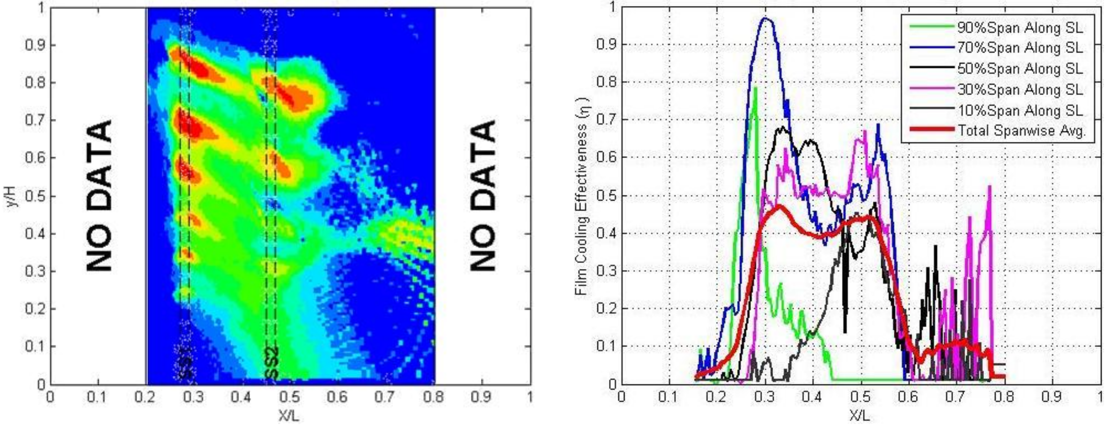

(e) Ma=1.1 Surface contour (f) Ma=1.1 Span-wise average

Figure 23 Film cooling effectiveness distribution for M=1.3 DR=2.0

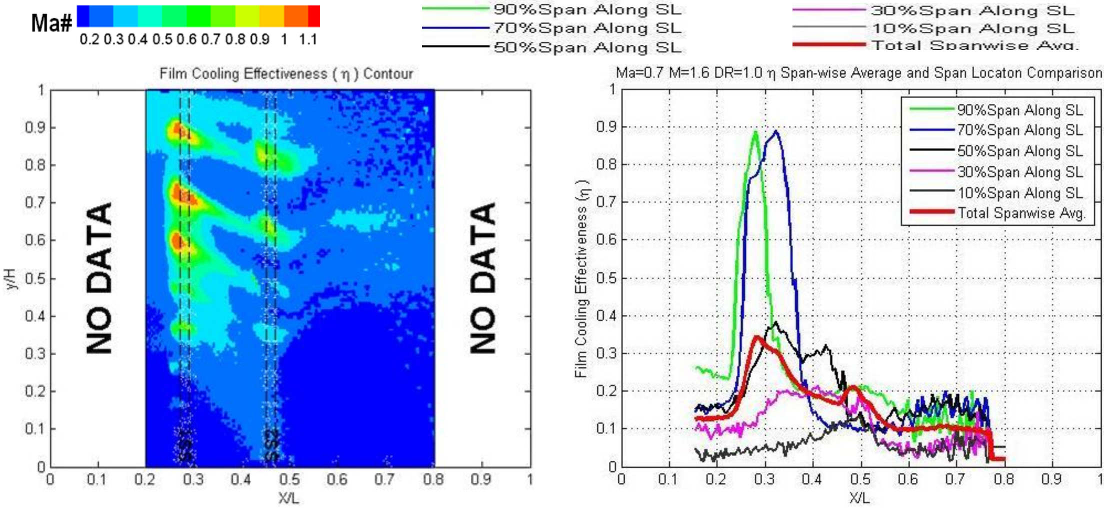

(a) Ma=0.7 Surface contour **(b) Ma=0.7 Span-wise average**

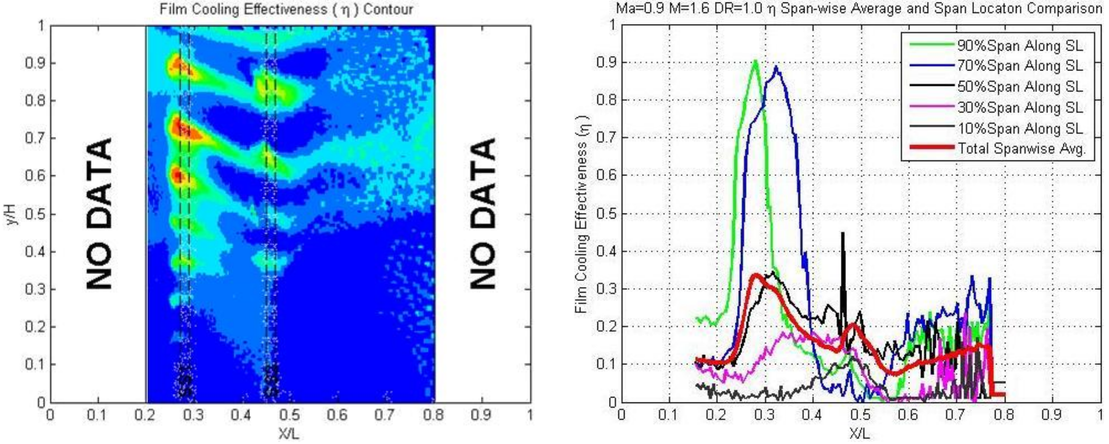

(c) Ma=0.9 Surface contour **(d) Ma=0.9 Span-wise average**

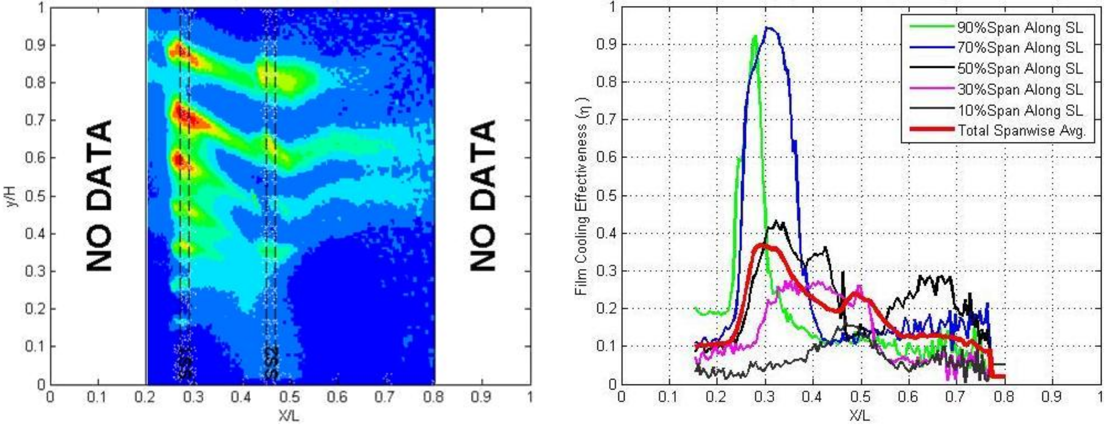

(e) Ma=1.1 Surface contour **(f) Ma=1.1 Span-wise average**

Figure 24 Film cooling effectiveness distribution for M=1.6 DR=1.0

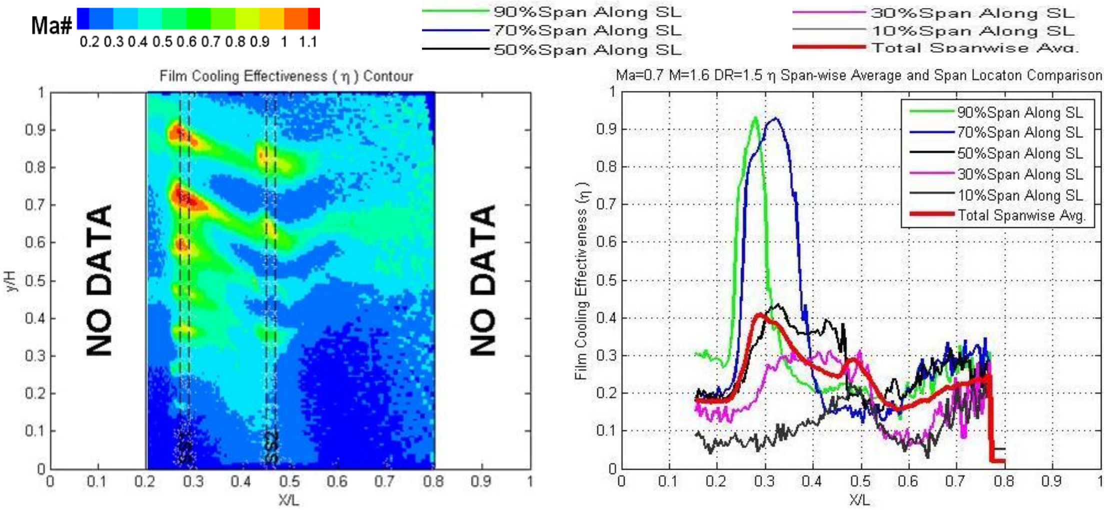

(a) Ma=0.7 Surface contour (b) Ma=0.7 Span-wise average

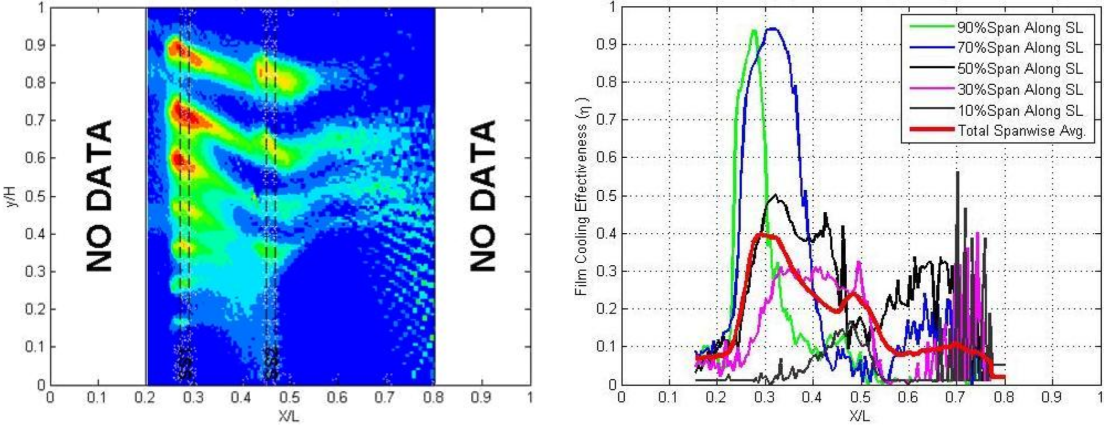

(c) Ma=0.9 Surface contour (d) Ma=0.9 Span-wise average

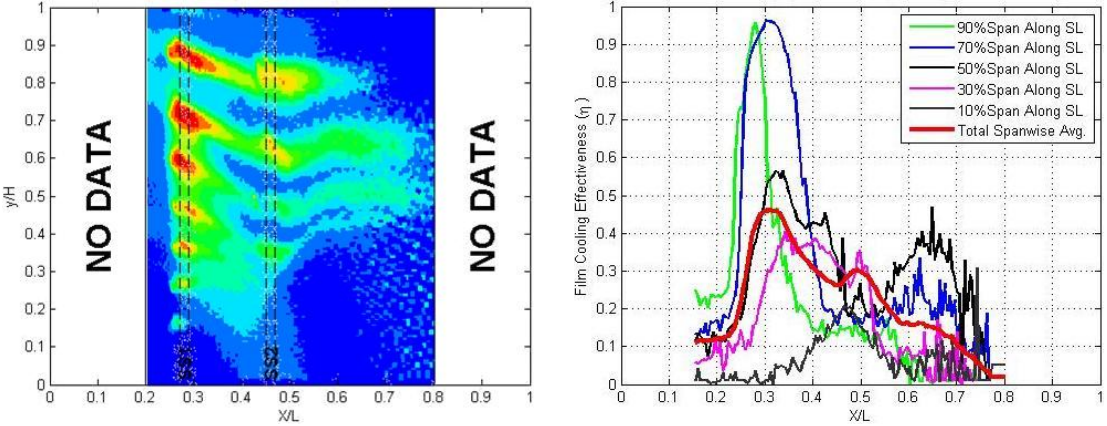

(e) Ma=1.1 Surface contour (f) Ma=1.1 Span-wise average

Figure 25 Film cooling effectiveness distribution for M=1.6 DR=1.5

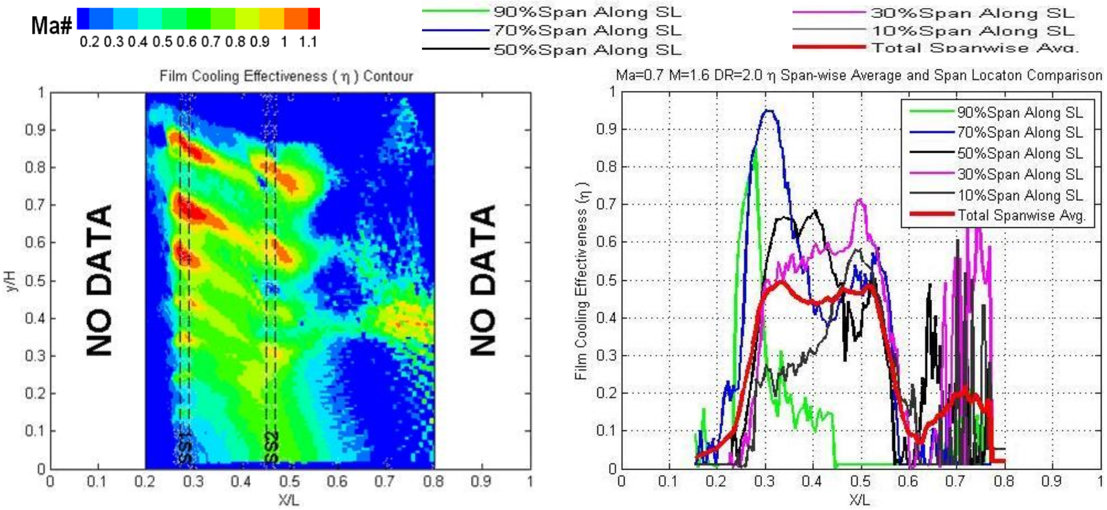

(a) Ma=0.7 Surface contour **(b) Ma=0.7 Span-wise average**

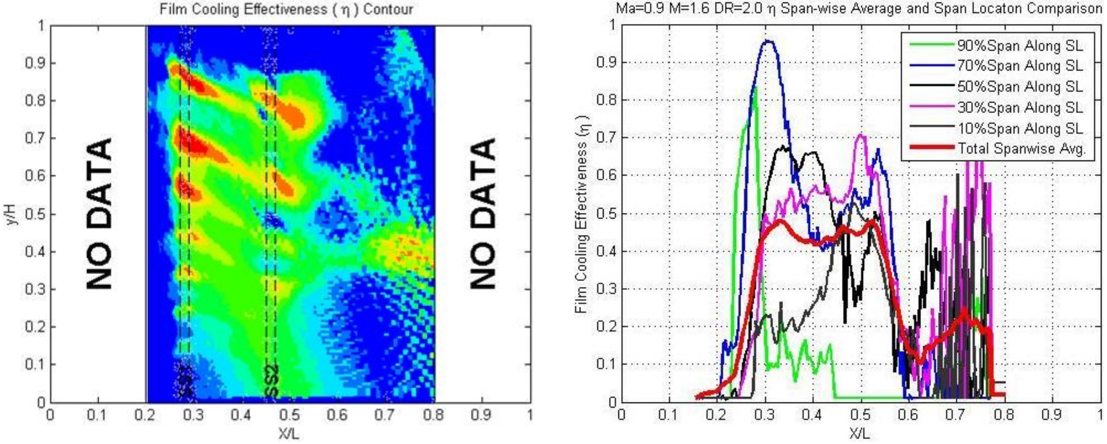

(c) Ma=0.9 Surface contour **(d) Ma=0.9 Span-wise average**

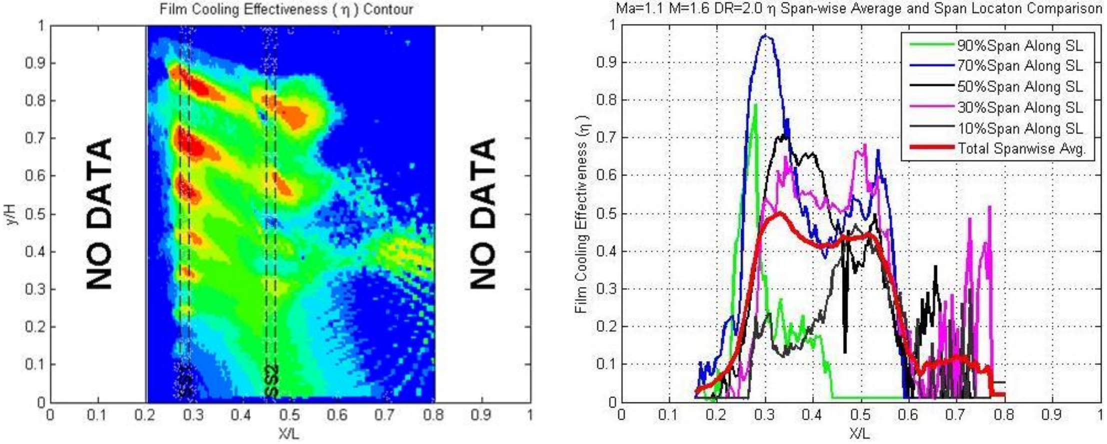

(e) Ma=1.1 Surface contour **(f) Ma=1.1 Span-wise average**

Figure 26 Film cooling effectiveness distribution for M=1.6 DR=2.0

II.F.3. Blowing Ratio (M) Effects

Following the coolant control concept illustrated in **Fig.9**, the actual blowing ratio can be tuned to desired value. The 'ε' is controlled to be less than 3%, however, due to instrument limitations the 'ε' can be as large as 5% only in few extreme cases. **Fig.27**, show the blowing and density ratio effects on the film cooling effectiveness contours at exit flow velocity Ma=0.7. Four blowing ratios studied M=0.7 (top 1st row), M=1.0 (2nd row), M=1.3 (3rd row), and M=1.6 (last row at figure bottom). Three density ratios by injecting three foreign gases as coolant, DR=1.0 (N_2, left column), DR=1.5 (CO_2, middle column), and DR=2.0 (85%Ar &15%SF_6, right column). From top row (low blowing ratio) to the bottom row (high blowing ratio) for all three densities in **Fig27**, it is evident that the film cooling distribution reduces with increasing blowing ratio. Similar trends were found in both transonic (Ma=0.9) and supersonic (Ma=1.1) flows conditions

II.F.4. Density Ratio (DR) Effects

Comparing **Fig.27**, the film cooling effectiveness is the greatest at the right (DR=2.0), than center (DR=1.5), than left column (DR=1.0). It is obvious that the film cooling effectiveness is positively correlated with density. In all cases, the DR=2.0 provided the superior coverage between SS1 and SS2 as well as the near hub portion around SS2 neighborhood. Consider the lowest blowing ratio case in the study (M=0.7), the film cooling effectiveness around SS1 first increased with density from DR=1.0 to 1.5, then decreases at DR=2.0. This is because for the same blowing ratio coolant jet velocity reduces as the density increases. For the vane surface downstream SS1, the film cooling effectiveness trend is similar compared with all other cases. Similar trends were found in both transonic (Ma=0.9, **Fig.28**) and supersonic (Ma=1.1, **Fig.29**) flow conditions.

For overall film cooling performance, DR=2.0 and DR=1.5 are superior in terms of magnitude and coverage respectively. For higher density ratio foreign gases, lower velocity required to achieve the same blowing ratio, and therefore reduces the momentum of the coolant. Coolant with lower momentum has more propensities to adhere to vane surface than higher momentum; as a result, with density ratio increased from 1.0 to 1.5, there is a visible increase in effectiveness, both in terms of the trace length and the trace width. However, for DR=1.5 to 2.0 the effectiveness increased significantly at the regions near film cooling configuration and shown less trace at the downstream.

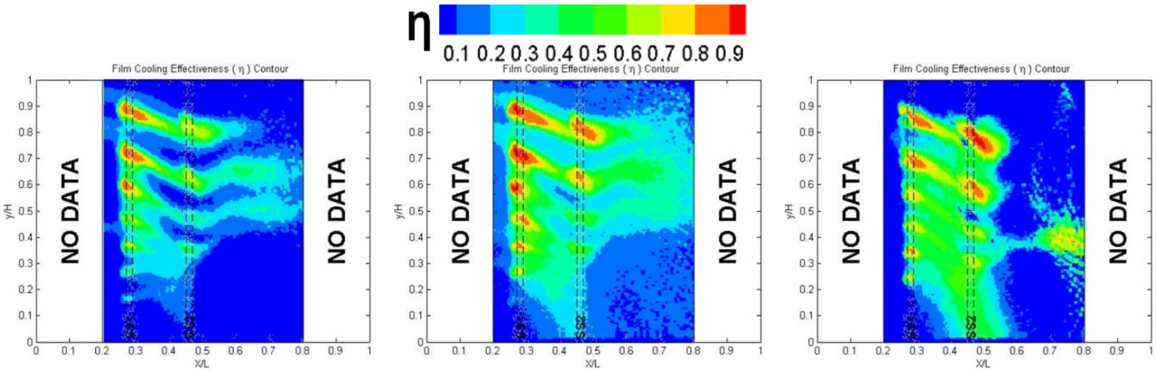

(a)M=0.7 DR=1.0 (b)M=0.7 DR=1.5 (c)M=0.7 DR=2.0

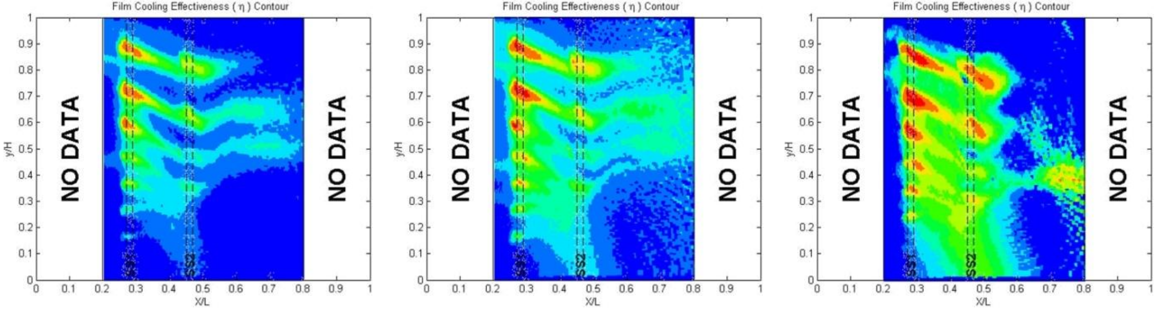

(d)M=1.0 DR=1.0 (e) M=1.0 DR=1.5 (f)M=1.0 DR=2.0

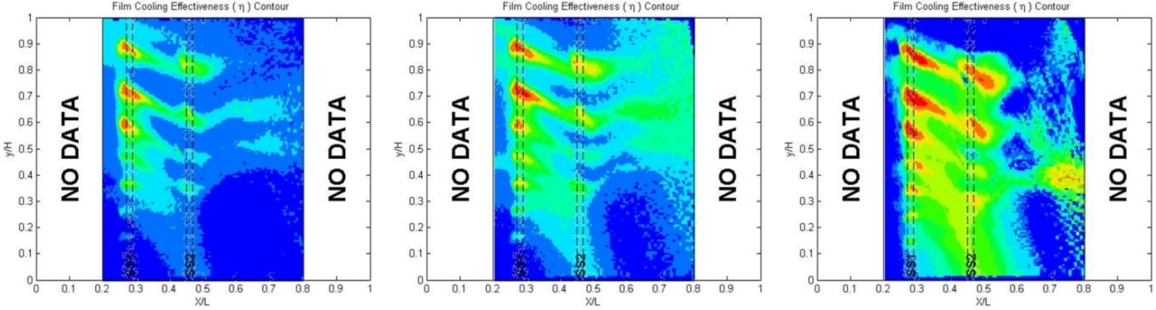

(g)M=1.3 DR=1.0 (h)M=1.3 DR=1.5 (i)M=1.3 DR=2.0

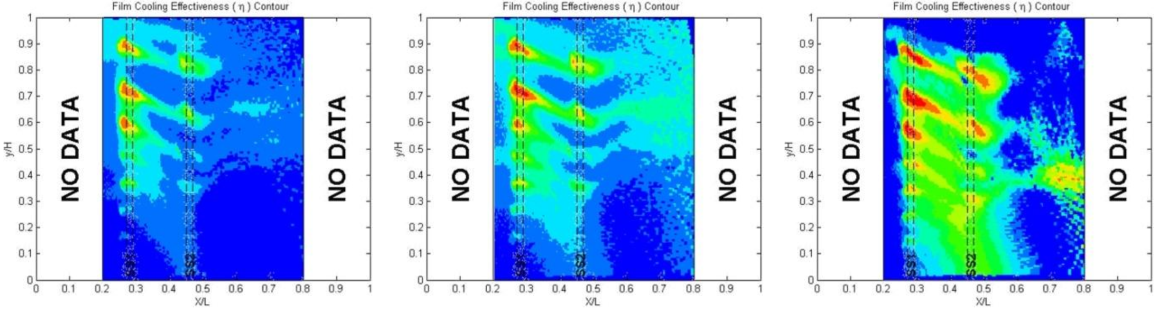

(j)M=1.6 DR=1.0 (k)M=1.6 DR=1.5 (l)M=1.6 DR=2.0

Figure 27 Blowing and density ratio effects on adiabatic effectiveness at Ma=0.7

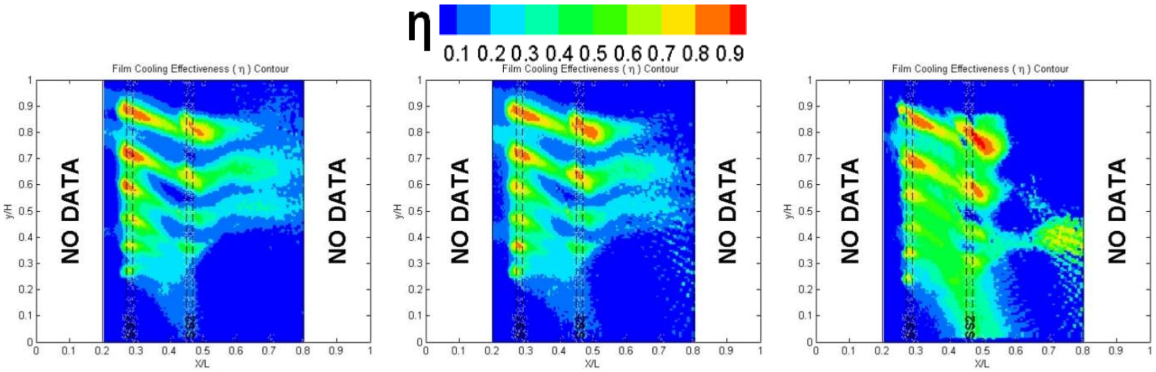

(a)M=0.7 DR=1.0 **(b)M=0.7 DR=1.5** **(c)M=0.7 DR=2.0**

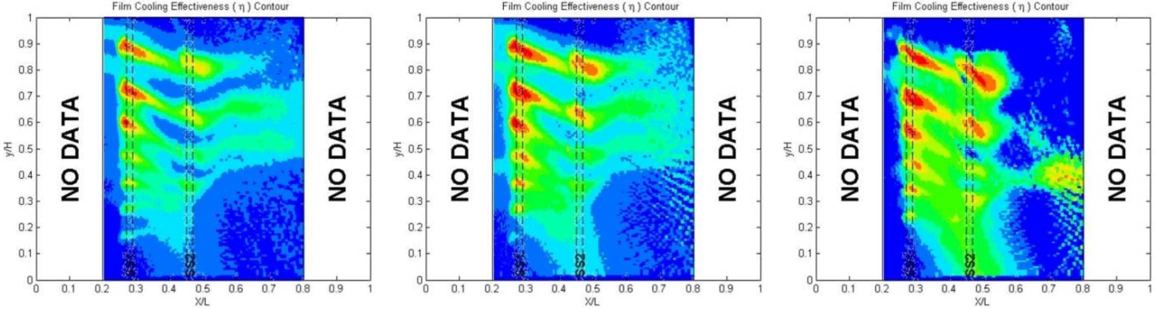

(d)M=1.0 DR=1.0 **(e) M=1.0 DR=1.5** **(f)M=1.0 DR=2.0**

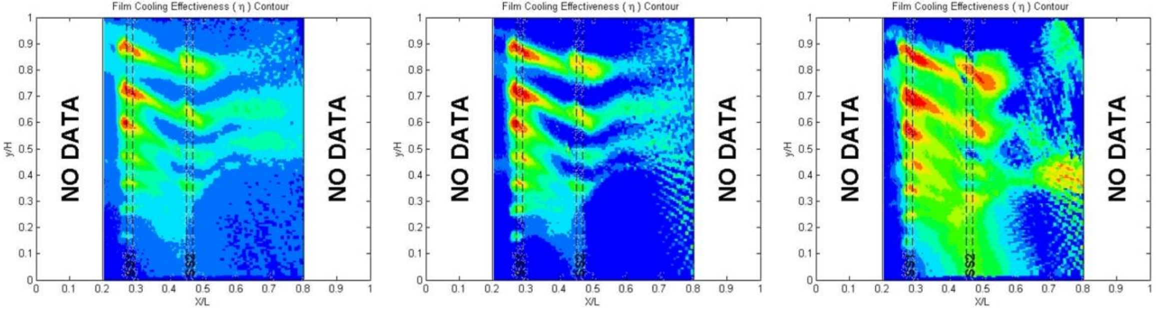

(g)M=1.3 DR=1.0 **(h)M=1.3 DR=1.5** **(i)M=1.3 DR=2.0**

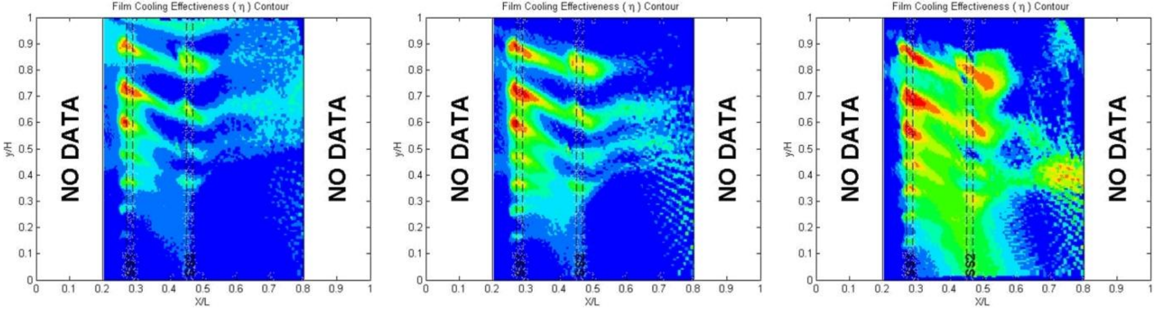

(j)M=1.6 DR=1.0 **(k)M=1.6 DR=1.5** **(l)M=1.6 DR=2.0**

Figure 28 Blowing and density ratio effects on adiabatic effectiveness at Ma=0.9

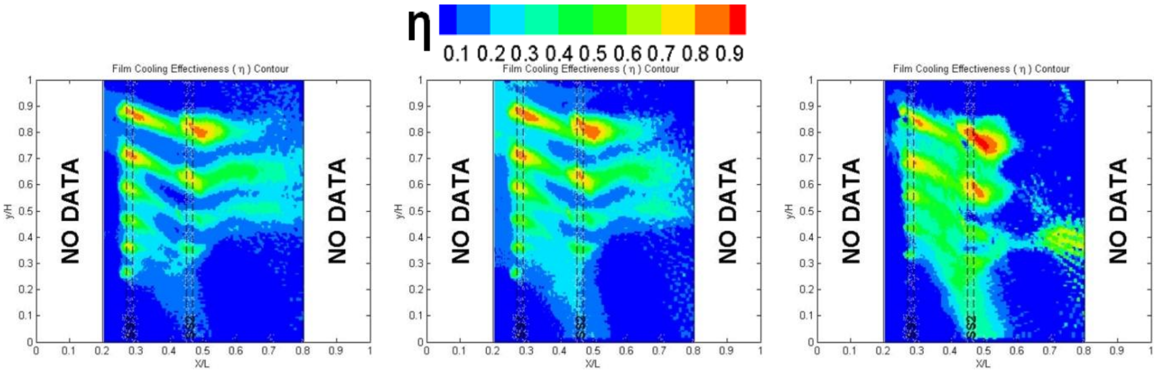

(a)M=0.7 DR=1.0 **(b)M=0.7 DR=1.5** **(c)M=0.7 DR=2.0**

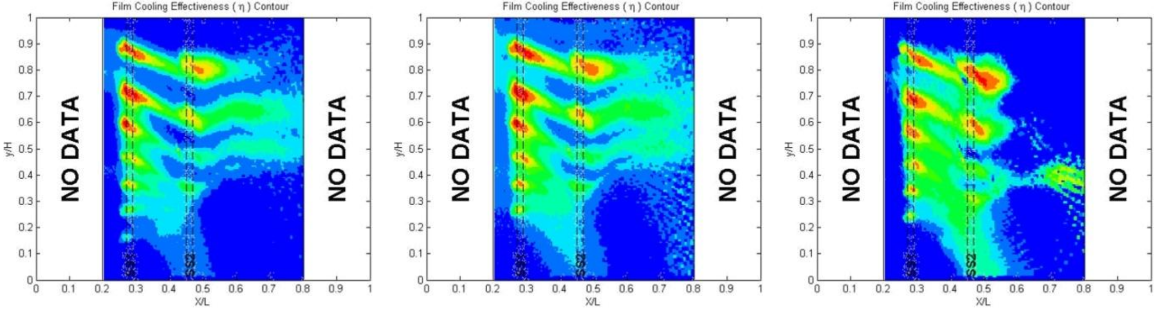

(d)M=1.0 DR=1.0 **(e) M=1.0 DR=1.5** **(f)M=1.0 DR=2.0**

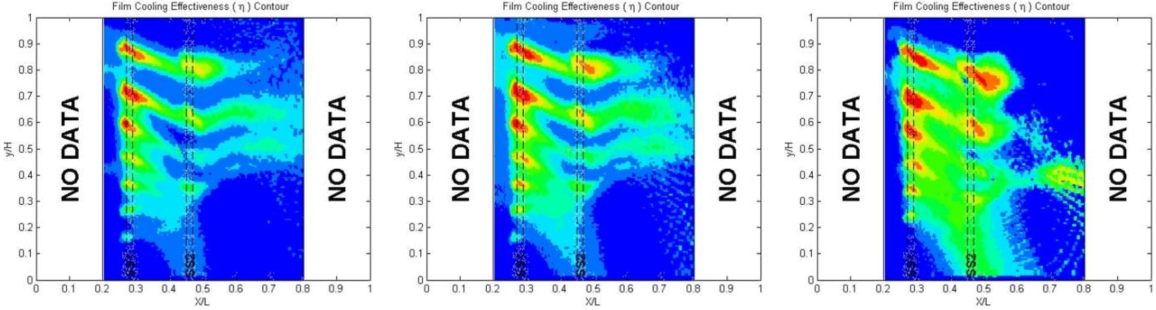

(g)M=1.3 DR=1.0 **(h)M=1.3 DR=1.5** **(i)M=1.3 DR=2.0**

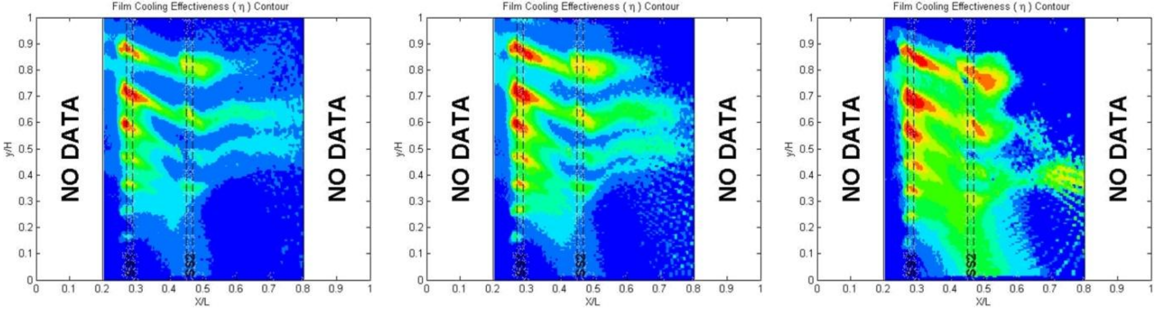

(j)M=1.6 DR=1.0 **(k)M=1.6 DR=1.5** **(l)M=1.6 DR=2.0**

Figure 29 Blowing and density ratio effects on adiabatic effectiveness at Ma=1.1

II.F.5. Effects of Exit Mach Number

Exit Mach number effects on adiabatic film cooling effectiveness distribution is demonstrated in **Figs.30** (DR=1.0)**, 31** (DR=1.5)**,** and **32** (DR=2.0)**.** Two blowing ratios, M=0.7 (upper row), M=1.6 (bottom row), and three Mach numbers listed from subsonic to transonic, followed by Ma=0.7 (left column), Ma=0.9 (middle column), and Ma=1.1 (right column) respectively.

Consider medium (DR=1.5) and low (DR=1.0) density ratios in subsonic mainstream flow (Ma#0.7), blowing ratio exerts a negative effect on film cooling effectiveness. And the cutback is more symbolic in DR=1.5. This is evident in left columns of **Fig.30and 31.** The film cooling traces reduces in length and thickness as the blowing ratio increases, especially at the near hole area around SS1 and SS2. This phenomenon is evidence of cooling jet lift off from the vane surface. On can conclude that at Ma=0.7, low and medium coolant jet lift off begin to occur when M>0.7. This trend is reversed in high density case.

In transonic flow (Ma#=0.9, center column), the trends for each densities are similar compared with subsonic case. In medium density coolant case (**Fig31**), the film cooling effectiveness again decreases with blowing ratio increasing and the difference enhanced when traveling from SS1 to SS2. In supersonic (Ma#=1.1) case. As listed in right columns in **Fig.30, 31 and 32**, for all densities studied, blowing ratio utilizes a positive effect on local film cooing effectiveness.

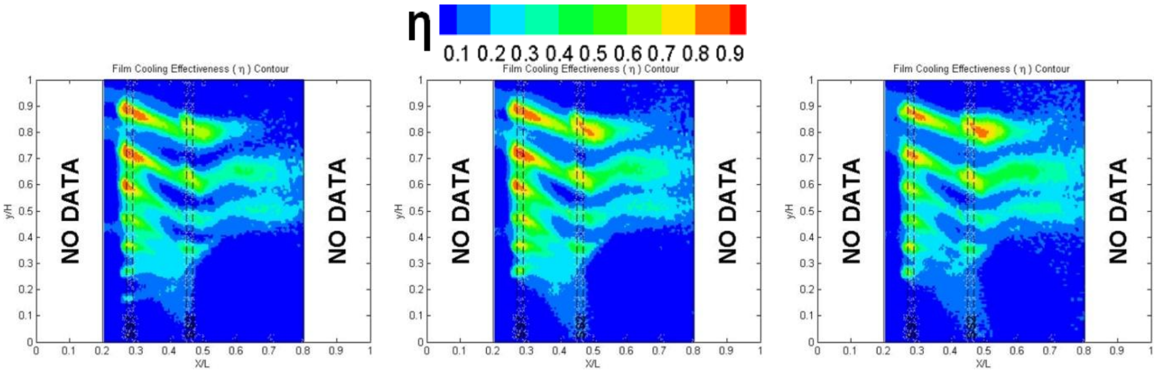

(a)Ma=0.7 M=0.7 (b)Ma=0.9 M=0.7 (c)Ma=1.1 M=0.7

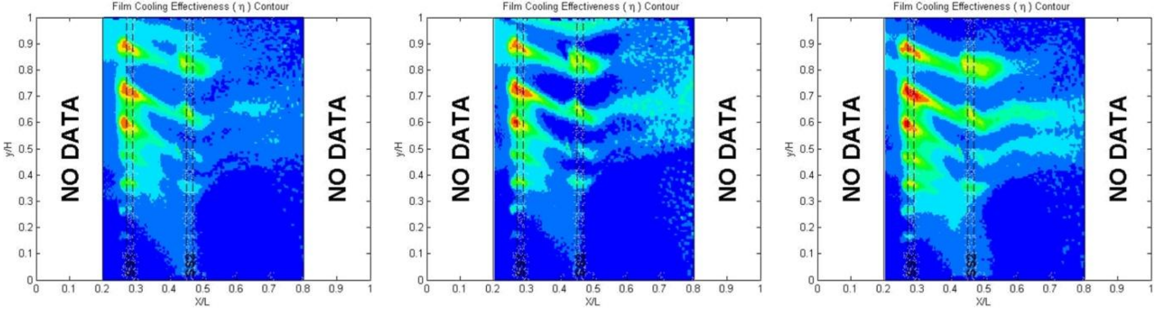

(d)Ma=0.7 M=1.6 (e)Ma=0.9 M=1.6 (f)Ma=1.1 M=1.6

Figure 30 Mach number effect on adiabatic effectiveness at DR=1.0

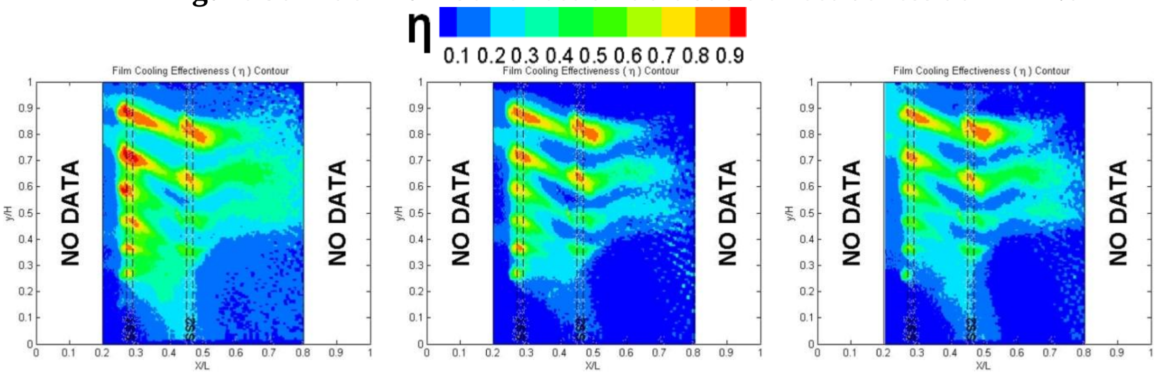

(a)Ma=0.7 M=0.7 (b)Ma=0.9 M=0.7 (c)Ma=1.1 M=0.7

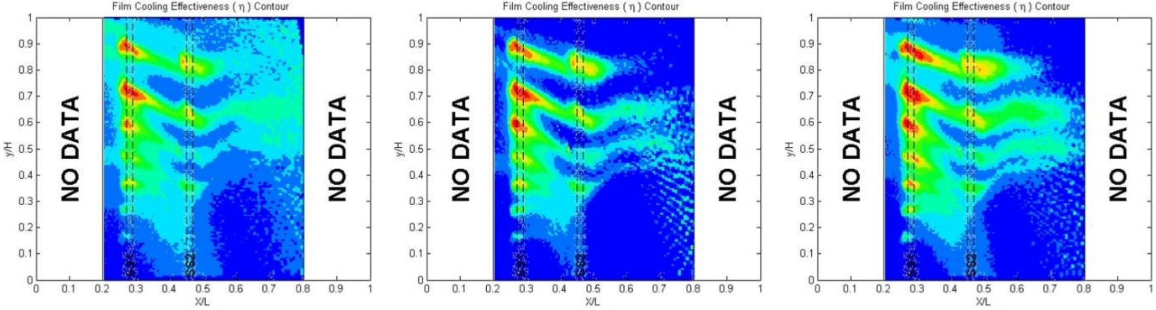

(d)Ma=0.7 M=1.6 (e)Ma=0.9 M=1.6 (f)Ma=1.1 M=1.6

Figure 31 Mach number effect on adiabatic effectiveness at DR=1.5

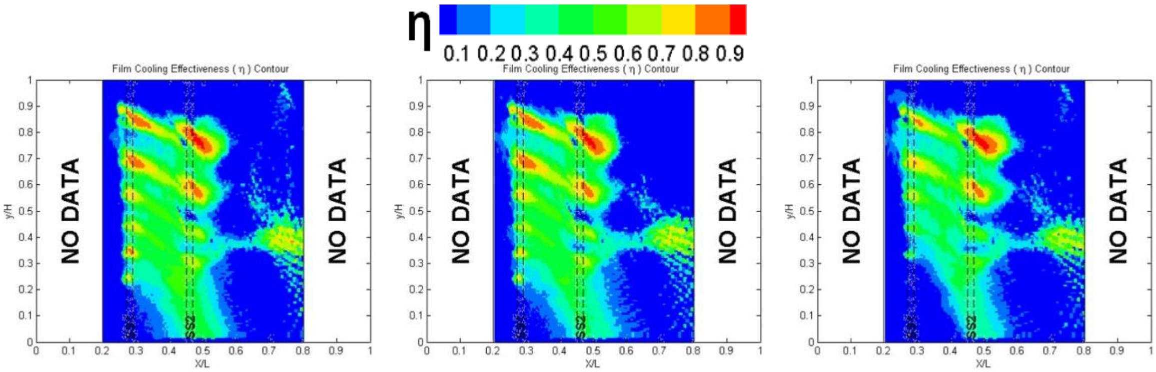

(b) Ma=0.7 M=0.7 **(b)Ma=0.9 M=0.7** **(c)Ma=1.1 M=0.7**

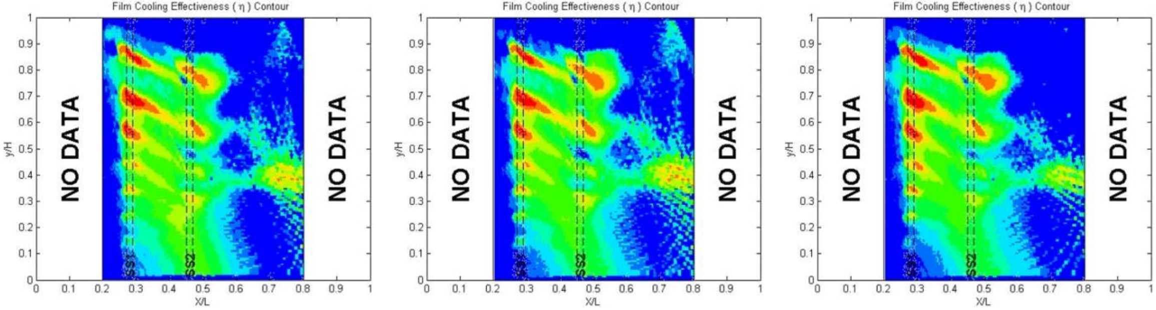

(d)Ma=0.7 M=1.6 **(e)Ma=0.9 M=1.6** **(f)Ma=1.1 M=1.6**

Figure 32 Mach number effect on adiabatic effectiveness at DR=2.0

II.F.6. Spanwise-Averaged Effectiveness

The results of all studied cases are plotted in **Fig.33** for M=0.7, 1.0, 13, and 1.6 respectively. This provides a clear physical understanding of film cooling effectiveness following stream line direction. Denser coolant is represented with solid lines; lighter coolant ejection is indicated by dashed lines. And green, blue and red lines for Ma=0.7, 0.9 and 1.1 respectively. Generally, the high density coolant provides significant higher level film cooling effectiveness compared with lower density ones; especially in the region between first (SS1)/ second (SS2) peaks and the downstream.

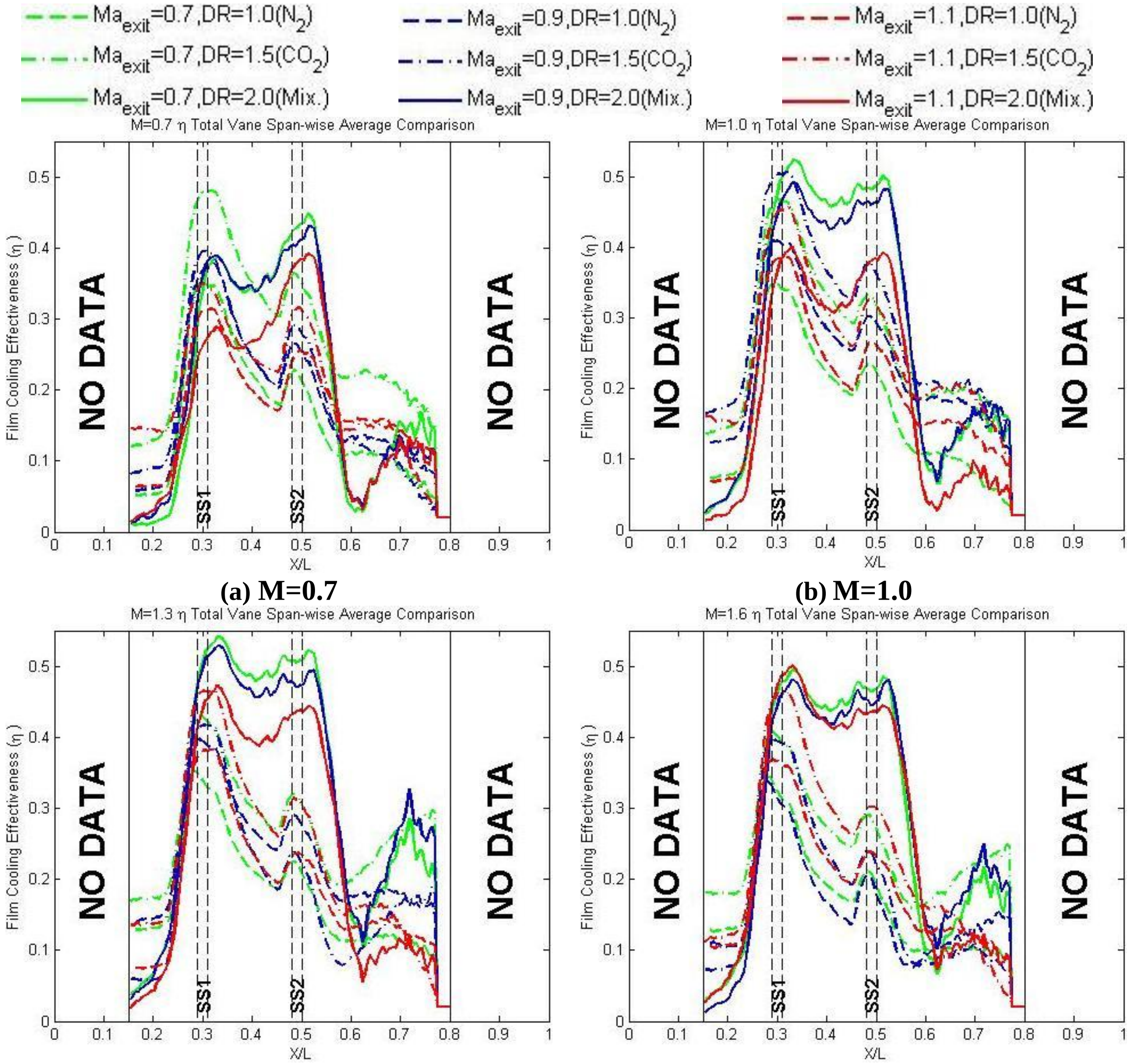

(a) M=0.7 **(b) M=1.0**

(c) M=1.3 **(d) M=1.6**

Figure 33 Spanwise-averge film cooling effectiveness as a function density ratio (DR) and Mach number (Ma)

For high density (DR=2.0) coolant in subsonic (Ma#=0.7) and transonic (Ma#=0.9), the film cooling effectiveness first increases with blowing ratio form M=0.7 to 1.3. However, the effectiveness drops close to M=1.0 level while further increase blowing ratio to 1.6. It is worthy to point out for high density coolant in supersonic (Ma#=1.1) flow, the film cooling effectiveness raised with blowing ratio monotonically. Yet the escalation from M=1.3 to 1.6 is relatively minimal. Around SS1 and SS2 neighborhood, in M=0.7, 1.0, and 1.3 cases, the reduction from Ma=0.9 to 1.0 is 2 to 3 times larger compared (around 20~25%) with Ma=0.7 to 0.9. At M=1.6 case, the Mach number effect around first and second peak area is almost negligible (4% reduce from Ma=0.7 to 1.1). More distinguished difference observed at the downstream at the potential shock region. The film cooling effectiveness slashed down to 50% and 30% of M=0.7 at M=1.0, 1.6 and M=1.3 cases.

Mach number effect with medium density ratio (DR=1.5) is more diverse. Film cooling effectiveness deceases with Mach number increase in lower blowing ratio (M=0.7). For higher (M=1.3 and 1.6) blowing ratios, the film cooling effectiveness distribution first decrease with Much number sub-trans sonic Mach number region. Also at SS1, the film cooling is inert. The film cooling effectiveness increased with Mach number in trans-supersonic range. The M=1.0 case shows a transition of trends. Since the Mach number utilized a positive effect in M=0.7~0.9 region, yet decreases to Ma=0.7 level at supersonic flow (Ma=1.1). Supersonic flow velocity in M=1.3 and 1.6 cases vastly shorten film cooling effectiveness at downstream. Since at the potential shock region, the coolant- mainstream mixing occurs even more vibrantly.

In low density (DR=1.0) high blowing ratio (M=1.6) case, the film cooling effectiveness decreased with Mach number increase. However, this trend is less obvious at the first (SS1) and second peak (SS2) in sub-trans sonic region. In supersonic mainstream, the Mach number exerts a positive effect on film cooling effectiveness. For other blowing ratios (M=0.7, 1.0, 1.3), film cooling ascends with Mach number at sub-trans sonic region and decreased in supersonic mainstream. The decreasing is more mild in the medium blowing ratio (M=1.0 and 1.3) cases since the value of Ma=1.1 fall between Ma=0.7 and 0.9.

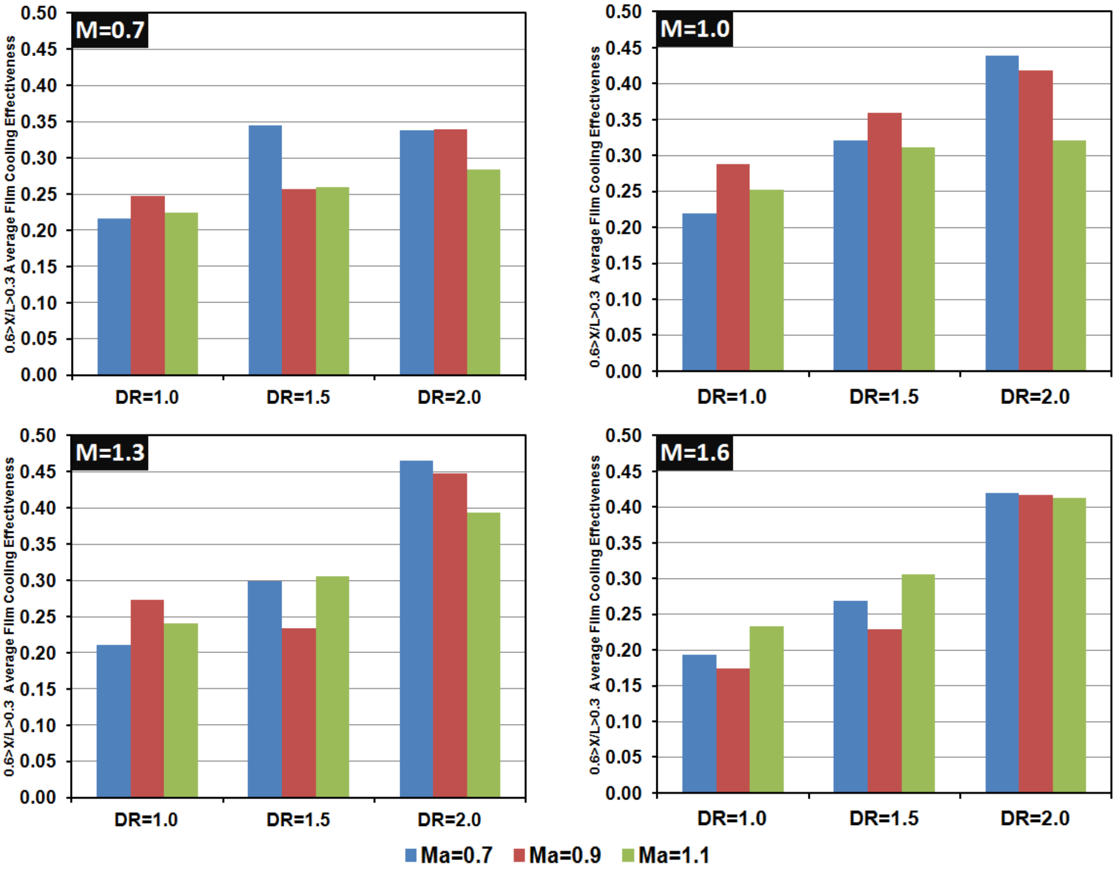

Figure 34 0.6>X/L>0.3 average film cooling effectiveness

In transonic flow, with medium and low density coolant jets, the film cooling effectiveness increases with blowing ratio from 0.7 to 1.0. However, the trend reverses while further increase blowing ratio to 1.3 and 1.6. This is due to the elevated mainstream velocity impedes coolant jets to detach from vane surface and delays the lift off to M=1.0~1.3. It is worthy to point out that this reduction in film cooling effectiveness can be as severe to make DR=1.0 M=1.6 results 15% lower than M=0.7.

Similar tendency found in supersonic (Ma#=1.1) case. The blowing ratio ranged from 0.7 to 1.0 utilizes a positive effect on film cooing effectiveness. When go beyond M=1.0, the difference in film cooling effectiveness is marginal for M=1.3 and 1.6 cases. The presence of Shockwave further hinders the jet lift off and contributes film cooling effectiveness.

II.F.7. Downstream Shock Effect

Fig34 displays overall average film cooling effectiveness for region (0.6>X/L>0.3) in which contains the first (SS1) and second (SS2) peaks. It is clearly that in this region, DR= 2.0, in all blowing ratios, the Mack number exerts a monotonic negative effect to film cooling. Generally, DR=2.0 is the optimum coolant when comparing the film cooling effectiveness between all coolant ratios and almost in all mach numbers; it is even superior in high blowing ratio and Mach number case. Due to less mixing the coolant jet has higher possibility to adhere the vanes surface. These findings are consistent with Ligrami [15] and Liu [36] that denser coolant performs better, typically at higher blowing ratio in transonic flow.

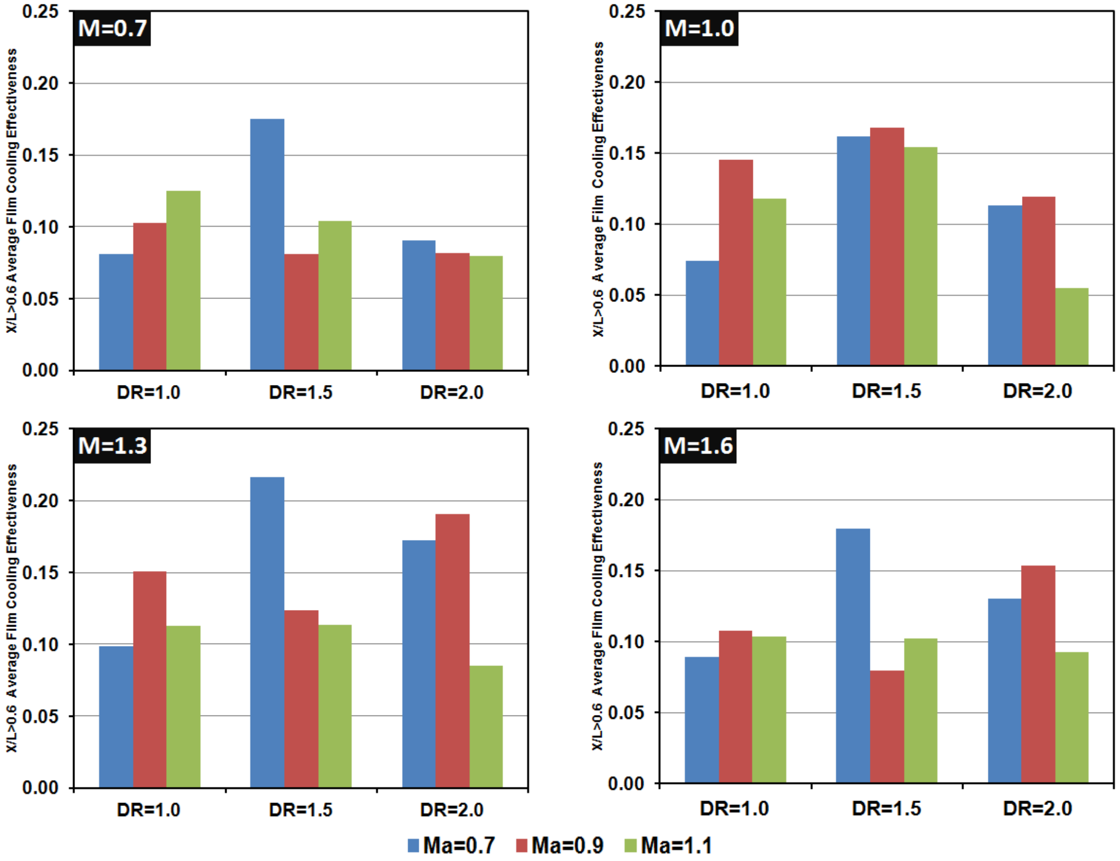

Figure 35 X/L>0.6 average film cooling effectiveness

Fig 35 displays the overall average film cooling effectiveness for portion between second and third peak (X/L=60~80, potential shock region). The trends are more diverse compared with 0.6>X/L>0.3, and magnitude shirks to20~30%. Regardless mainstream Mach number, DR=1.5 coolant provides the best film cooling effectiveness at M=0.7, 1.0, and 1.6 cases. DR=2.0 performs the best at M=1.3. With most blowing ratios, the film cooling first increases with Mach number than significantly drops at supersonic flow velocity. Regardless all parameters studied, in all DR=2.0 cases, a steep valley (around X/L=0.63) in film cooling effectiveness is observed after the second peak **(Fig33)**. The phenomenon is not as noticeable in DR=1.0 and 1.5 cases. At Ma=1.1 for all blowing ratios, the third peak of film cooling at downstream of DR=2.0 are the least compared all density ratios.

II.G. Conclusion

Pressure sensitive paint is used to measure adiabatic film-cooling effectiveness on a transonic turbine vane suction surface. Three important parameters; exit Mach number (subsonic to transonic), coolant blowing, and density ratios are examined for film cooling effectiveness. The key highlights are presented below:

1) PSP method produces well defined coolant trace on the vane suction side surface even with heavier foreign gases at transonic condition.
2) Blowing ratio exerts a complex effect on film cooling effectiveness. In lower Mach number and density side, the negative trend is more obvious. The trend reverses while consider high density coolant at supersonic flow. The cases in between is more like the transition; the increasing blowing ratio contributed the film cooling effectiveness till a certain value then turn to hinder the film cooling.
3) Denser coolants prevent film cooling jets to lift-off, resulting in a higher film cooling effectiveness. DR=2.0 and DR=1.5 are the optimum coolant density in terms of whole vane and downstream (potential shock) region film cooling effectiveness respectively.

4) Exit Mach number exerts a negative effect on cooling effectiveness in high density ratio cases. However, at close-to engine condition (M=1.6, DR=2.0) case, near the cooling configuration the effect is marginal. However, the effect at downstream is more severe.

CHAPTER III

HEAT TRANSFER IN ROTATING SERPENTINE COOLANT PASSAGE WITH RIBBED WALLS AT LOW MACH NUMBERS[*]

Gas turbines are used for aircraft propulsion and land-based power generation or industrial applications. Thermal efficiency and power output of gas turbines increase with increasing turbine rotor inlet temperatures (RIT). Current advanced gas turbine engines operate at turbine RIT (1500°C) far higher than the melting point of the blade material (1000°C); therefore, turbine blades are cooled by compressor discharge air (650°C). Since this extraction from compressor air incurs a penalty on the thermal efficiency and power output of the gas turbine engine, it is important to fully understand and optimize the cooling technology for a given turbine blade geometry under engine operating conditions. Gas turbine blades are cooled both internally and externally as shown in **Figure 36** by Han and Huh [38]. Internal cooling is achieved by passing the coolant through several rib-turbulated serpentine passages inside of the blade. Both jet impingement and pin-fin cooling are also used as a method of internal cooling. External cooling is also called film cooling. Internal coolant air is ejected out through discrete holes to provide a coolant film to protect the outside surface of the blade from hot combustion gases. The engine cooling system must be designed to ensure that the maximum blade surface temperatures and temperature gradients during operation are

---

[*] Reprinted with permission from Shang-Feng Yang, Je-Chin Han, Salam Azad, and Ching-Pang Lee, Heat transfer in rotating serpentine coolant passage with ribbed walls at low mach numbers, ASME Journal of Thermal Science and Engineering Application (2014) Paper No: TSEA-14-1056. Copyright© 2015 by Siemens Energy, Inc.

compatible with the allowable blade thermal stress for the life of the design. The major parameters that would affect internal cooling passage heat transfer have been identified as channel aspect ratio, channel shape, 180-deg sharp turn, entrance geometry, rib configuration, Reynolds number, rotation number, and buoyancy parameter [Han et al.] [1]. This study focuses on the heat transfer enhancement of serpentine internal cooling ribbed passages on a 1:1 full scaled rotating blade-shaped model.

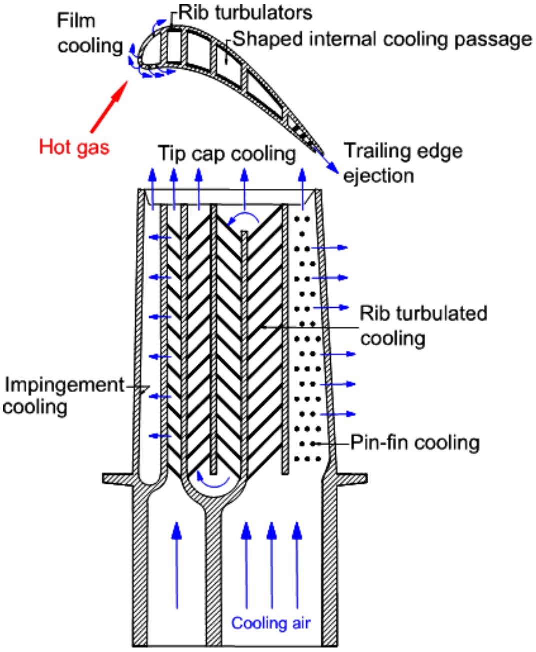

Figure 36 Common internal cooling techniques in advanced gas turbine blades

III.A. Literature Survey

III.A.1. Channel Aspect Ratio Effect

The internal cooling channels near the blade leading edge have been modeled as narrow rectangular channels with AR=1:4 and 1:2. The cross-section of the cooling channels changes along the cord length of the blade due to the blade profile. In the middle of the blade, the channels are closer to square in shape. Towards the trailing edge, the channels have wider aspect ratios of AR=2:1 and 4:1. An experimental study on the effects of the buoyancy parameter in various aspect ratio channels was performed by Fu et al. [39]. The study considered five different aspect ratio channels (AR=1:4, 1:2, 1:1, 2:1, and 4:1) with a fully developed flow inlet condition. The results showed that the overall levels of heat transfer enhancement (Nu/Nuo) for all the ribbed channels of different aspect ratios were comparable. However, significant differences arose in the pressure losses incurred in each of the channels. The 1:4 channel incurred the lowest pressure penalty; therefore, the thermal performance of the 1:4 channel was superior to the 1:2, 1:1, and 2:1 channels. In addition, they found that rotation has more effect on 1:4 and 1:2 channels as compared with 4:1 and 2:1 aspect ratio channels.

III.A.2. Rib Configuration Effect

The internal coolant passages are mostly modeled as short, square or rectangular channels with various aspect ratios. The heat transfer augmentation in rectangular coolant passages with rib turbulators primarily depends upon the rib turbulators' geometry, such as rib size, shape, distribution, flow-attack-angle, and the flow Reynolds number. Rib turbulators disturb only the near-wall flow for heat transfer enhancement. Therefore, the pressure drop penalty caused by rib turbulators is affordable for the blade internal cooling designs. There have been many basic studies by Han et al. [40-43] to understand the heat transfer augmentation versus the pressure drop penalty by the flow separation caused by rib-turbulators. In general, repeated ribs, used for coolant passages with a channel aspect ratio varying from ¼ (near blade leading edge) to 4 (near blade trailing edge), are nearly square in cross-section with a typical relative rib height of 5-10% of the coolant channel hydraulic diameter, a rib spacing-to-height ratio varying from 5 to 15, and a rib flow-attack-angle around 30° to 60°. In addition, smaller gas turbine blades have larger blockage ribs with 10-20% rib height-to-hydraulic diameter ratio at closer spacing with 3 to 5 rib spacing-to-height ratio reported by Taslim et al. [44]. Figure 37 displays the typical turbine blade internal cooling channel with rotation-induced vortices. More recently Rallabandi et al. [45] performed systematic experiments to measure heat transfer and pressure losses in a stationary square channel with round/sharp edged ribs at a wide range of Reynolds numbers ranging from 30,000 to very high flows of Re=400,000. These high Reynolds are typical of land based turbines.

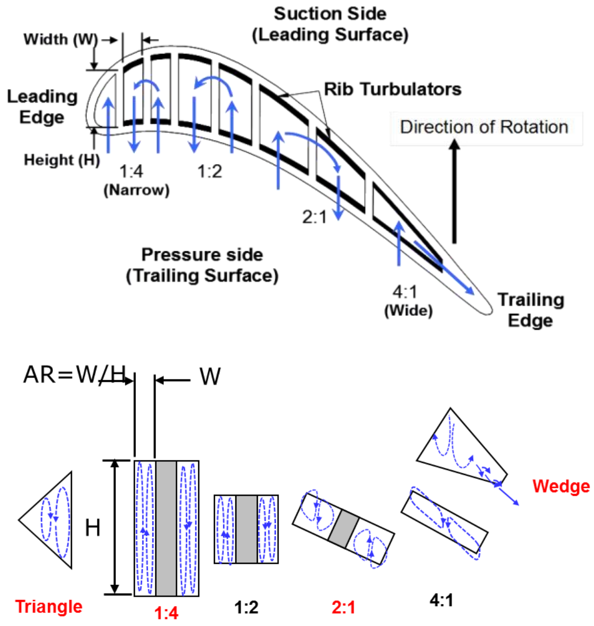

Figure 37 Typical turbine blade internal cooling channels (different tilt angle and aspect ratio) with rotation-induced vortices

III.A.3. Rotation Effect

Rotation induces Coriolis and centrifugal forces which produce cross-stream secondary flow in the rotating coolant passages; therefore, heat transfer coefficients in rotor coolant passages are very much different from those in non-rotating frames. Figure 2 shows the schematic of rotation-induced secondary flow vortices in various rotating channels by Han and Huh [38]. One important finding from recent studies is that rotation can greatly enhance heat transfer on one side of the cooling channel and reduce heat transfer on the opposite side of the cooling channel due to rotating-induced secondary flow, depending on the radial outflow or inflow of the cooling passages. Without considering rotational effect, the coolant passage would be over-cooled on one side while over-heated on the opposite side. For example, the heat transfer coefficient can enhance 2-3 times on the trailing surface and reduce up to 50% on the leading surface for the first-pass radial outward flow passage; however, the reverse is true for the second-pass radial inward flow passage due to the flow direction change. Results also show that the heat transfer difference between leading and trailing surfaces is greater in the first-pass than that in the second-pass due to the centrifugal buoyancy opposite to the flow direction by Wagner et al. [46] and Johnson et al. [47]. The effects of surface heating on rotating coolant channel heat transfer were reported by Han et al. [48] and Zhang et al. [49].

III.A.4. Channel Orientation Effect

Since the turbine blade is curved, the rotor blade cooling passage can have different channel orientations with respect to the rotating plane. Johnson et al. [50] studied the effects of rotation on the heat transfer for smooth and 45° ribbed serpentine channels with channel orientations of 0° and 45° to the axis of rotation. They found that the effects of Coriolis and buoyancy forces on heat transfer in the rotating channel are decreased with the channel at 45° compared to the results at 0°. This implies that the difference in heat transfer coefficient between leading and trailing surfaces due to rotation will be reduced when the channel has an angle to the axis of rotation. Dutta and

Han [51] used high performance broken V-shaped ribs in rotating two-pass square channels to study the effect of channel orientation on heat transfer. They concluded that the broken V-shaped ribs are better than the 60° angled ribs; the parallel 45° angled ribs are better than the crossed 45° angled ribs. In general, the difference between leading and trailing wall heat transfer coefficients is reduced for the channel with a 45° angle to the axis of rotation. The combined effects of high rotation number, channel shape, orientation, and aspect ratio on rotor coolant passage heat transfer with various high performance rib turbulators were also reported [52-55]. Results show that the channel shape, orientation, and aspect ratio significantly change local heat transfer coefficient distributions in rotor coolant passages with rib turbulators.

III.A.5. Sharp 180-deg Turn Effect

The internal cooling passages of the gas turbine blade are connected by 180 degree turns. This allows the cooling medium to make multiple pass through the blade so that maximum cooling potential is realized. Liu et al [55] and Huh et al [56][58] considered heat transfer in rectangular channels connected by a sharp 180 degree turn for the two different aspect ratio ducts. They found the stark difference in heat transfer behavior in the second half of the turn of the two channels. The heat transfer in the 1:4 channel increases on both the leading and the trailing surfaces, however, the leading heat transfer enhancement is greater since the Coriolis force changes direction because the flow is radially inward. The 2:1 channel shows only a modest increase of heat transfer and the effect of rotation levels off even at the higher rotation numbers. The effect of the sharp 180° turn is quite different for these two channels.

III.A.6. Developing Flow Entrance Effect

Most research topics about internal heat transfer in rotating channels published in open literature laid their basis on fully developed flow. However, due to limited spaces in actual gas turbine blades, the internal coolant flow experienced severe effects contributed by entrance geometry. Clearly, when taking entrance effects into account, the heat transfer characteristics differ from that of fully developed flow. And entrance effect becomes the latest topic in rotating channel internal heat transfer study. Wright et al. [59] studied three entrance geometries with a wide channel aspect ratio (AR = 4:1) channel. They determined that the entrance effects significantly enhance the heat transfer and the effect is stronger in smooth channels than in ribbed channels. Moreover, they pointed out the entrance geometry effect decays while the rotation number rises. Liu et al. [57] studied heat transfer under high rotation numbers ranged from 0.0 (stationary) to 0.65 in an AR=1:4 narrow aspect ratio channel. The sharp bend entrance geometry resulted in relatively high heat transfer in first passage compared to Fu et al. [60] (fully developed flow at the entrance). Liu et al. [57] also pointed out this sharp bend entrance also reduced the rotation effect in the first passage. However, due to strong turn effect, the entrance effect diluted in the second passage.

III.B. Objectives of this Study

The typical coolant passage Reynolds numbers are varied from 100,000 to 200,000 for large land-based power generation gas turbine blades and vanes. The new designs aim at reducing cooling flow rate, therefore, coolant passage Reynolds numbers can be as low as 40,000 to 50,000. Based on typical turbine operation conditions, the corresponding coolant passage Mach numbers can be as low as 0.02 which is far below from the current practical design value around 0.1. Most published coolant passage heat transfer data were conducted at Mach numbers around 0.1. It is critical to evaluate the potential impact of low Mach numbers on coolant passage heat transfer at reduced Reynolds number flows for rotating and non-rotating conditions. In addition, from the brief review of open literature, the majority of heat transfer studies are simulated by scaled down flow channel models. Due to limitations of laboratory facilities, little information was available in 1:1 scaled real blade-shaped coolant passage at simulated engine cooling flow rotation conditions. The objectives of the current study are as follows:

1. Provide heat transfer information under stationary and rotating condition for real serpentine-shaped ribbed channels in a real sized model of a land-based gas turbine blade.
2. Evaluate the potential impact of low Mach numbers on coolant passage heat transfer at reduced Reynolds number flows for rotating and non-rotating conditions.
3. Study the rotation effect on heat transfer enhancement on channel mid-span as well as before and after the tip and hub turn regions at high rotation number conditions.
4. Develop correlations for the Reynolds Numbers useful for predicting heat transfer enhancement under non-rotating conditions.
5. Develop correlations for the rotation numbers useful for predicting heat transfer enhancement under rotating conditions.

III.C. Experimental Setup

The operating rotation speed of a gas turbine can be up to several thousands of rpm. This rotation speed causes dramatic changes in the internal cooling channel flow field. The drastic differences between stationary and rotation conditions are due to rotation induced Coriolis and buoyancy force. Rotation number is defined as the ratio of the Coriolis force to the bulk inertia force and is used to quantify this rotation effect. Blades designed for land based gas turbine engines are physically larger in size compared with aviation purpose. Since the hydraulic diameters of internal passages are much larger in a land based gas turbine blade, this leads to a significantly higher Reynolds number (of up to 500,000) flow in internal passages. Reaching actual engine operating condition (several thousands of rpm) in a laboratory rotation experiment setup is a tremendous challenge. However, through the rotation number concept, simulating engine operation conditions in laboratory facilities is possible. Increasing coolant gas density is one approach to achieve high rotation numbers similar to engine condition in a laboratory facility. Compressed Freon R-134a vapor is selected as the coolant gas in this study rather than compressed air due to molecular weight. The molecular weight of Freon R-134a is almost four times larger than air, and it can serve purpose better when compressed to same pressure. For a fixed gas flow rate (Reynolds number) and hydraulic diameter, an increased density will lead to a decrease in velocity. A decreased velocity will further increase the rotation number. In order to simulate engine operation condition, the experiments for this study were conducted with R-134a vapor at a pressure of 358.53 kPa (52.0 psi) (gauge). The nominal Reynolds numbers tested in first passage ranged from 30,000 to 70,000 with an increment of 10,000. At each Reynolds number, the rotational speed varied from 0 (stationary) to 300 rpm. For the current study, first passage rotation numbers of 0.6 and 0.25 can be achieved at 300 rpm with Reynolds number of 30,000 and 70,000 respectively.

III.C.1. Full Scale Rotation Facility

Figure 38 shows the full scale rotating facility assembly used to conduct the experiment for current study. A 74.6 kW (100hp) electric motor is connected via belt to the drive shaft which spins the aluminum rotation arm (100cm in radius). In order to minimize structure vibration level during rotation, on the rotation arm, counterweights positioned at opposite side to the test section pressure vessel are used as balance. Freon R-134a vapor mass flow rate is measured and controlled by Micro-Motion CMF050 Coriolis mass flow meter and Badgar Meter control valve (both not shown).

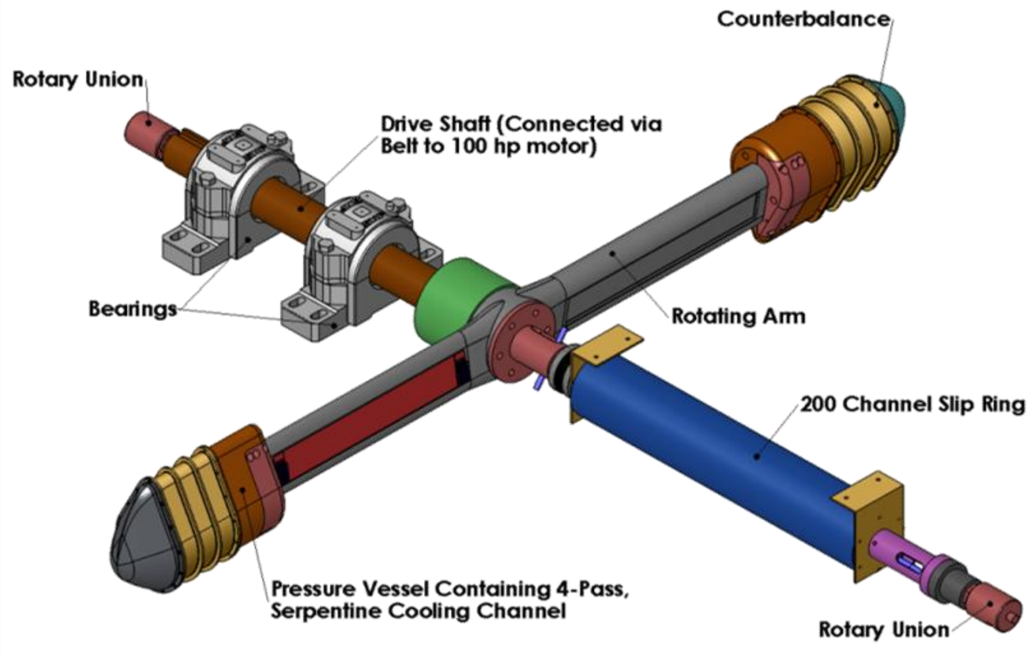

Figure 38 Schematic of rotating facility

The R134a vapor enters the rotating facility via rotary union on drive shaft side. The vapor passes through the hub and into the bore of the rotating arm. Copper tubes were used to direct the vapor flow from the arm to the test section housing. After R134a flow passes through the test section, the vapor leaves the pressure vessel. The heated R134a vapor is then directed, by means of copper tubing through the bore of 200-channel slip rings to the rotary union. Steel pipes are connected to the exit rotary union and circulate refrigerant vapor back to the 2.052 kW (70,000BTUH) air-cooled condensing unit.

III.C.2. Test Section Configuration

For the present study, a three passage serpentine channel test section was used in experiments. As illustrated in **Figure 39(a)**, there are five regions in each passages, a total of fifteen sequential regions compose the test section. Regions 1 to 5 compose the first, 6 to 10 the second and 11 to 15 the third passage. Most of the regions are surrounded by copper plate instrumentation in four sides, namely, leading (suction), trailing (pressure), and two divide walls. They are regions 5, 6 (first turn), 10, 11 (second turn) and 15 (third turn for channel exit). Copper plates in all regions are thermally insulated from each other, and regions are also thermally insulated from other regions. Each passage has a different trapezoidal shape, this results in three hydraulic diameters in corresponding passages.

As illustrated in **Figure 39(b)**, four silicon heaters are installed for each passage, each of them directly contact with four or five copper plates. Red circles and blue squares denote heater positions for leading and trailing surfaces in all three passages. While black triangles and green squares illustrate heater positions on the first and second divide wall surfaces. The green garolite is selected for test section model material due to easiness for machining, high structural strength, good thermal resistance, and low thermal conductivity. The test section is secured inside of an aluminum pressure vessel which attached to an aluminum rotating arm (100 cm radius of rotation). As shown in **Figure 38**, a similar dummy pressure vessel served as counterbalance is installed on the opposite side of the rotating arm. The three–pass serpentine configuration built in test section simulates the internal cooling channels in a real land- based gas turbine blade. As indicated in **Figure 39(b)**, the hydraulic diameters are 19.05 mm (0.75 in), 17.02 mm (0.67 in), and 11.68 mm (0.46 in) in the first, second and third passages respectively.

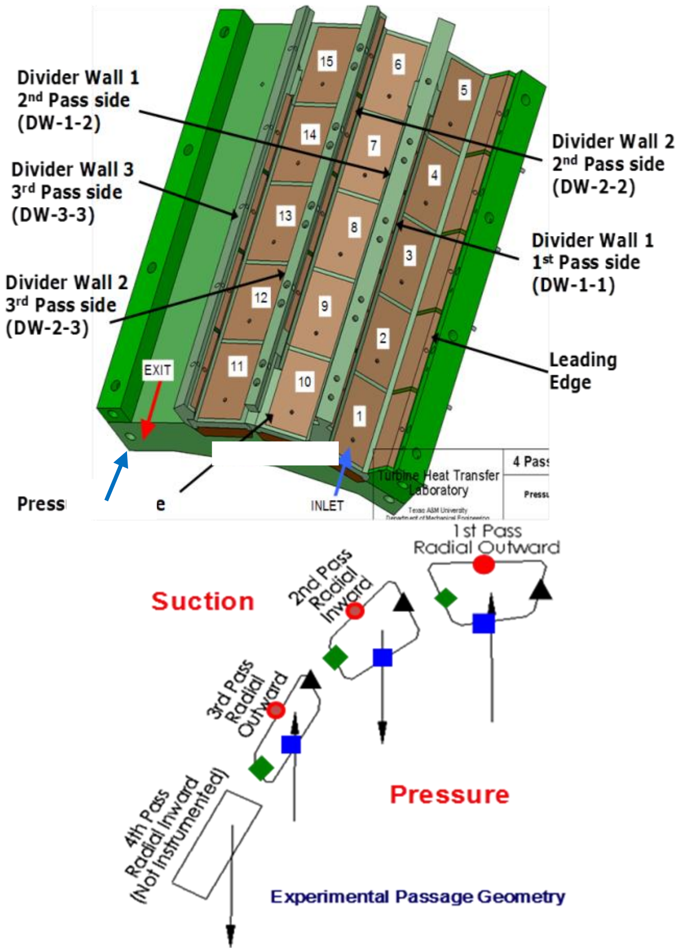

(

Figure 39 Flow passage characteristics (a) internal view of test section on pressure surface, (b) cross section view of serpentine internal flow channels.

As illustrated in **Figure 40**, the rib pitch to height ratio (*P/e*) in this study is designed to be 10, since it is a typical value employed by gas turbine designers and was well studied by numerous open literatures. Furthermore, using the same rib height, the channel blockage ratios (e/D_h) are 0.081, 0.091, and 0.133 at the first, the second and third passages respectively. Parallel 45° angled ribs are placed on both pressure and suction walls with a staggered pattern. All data reported in this study corresponded to these geometry parameters.

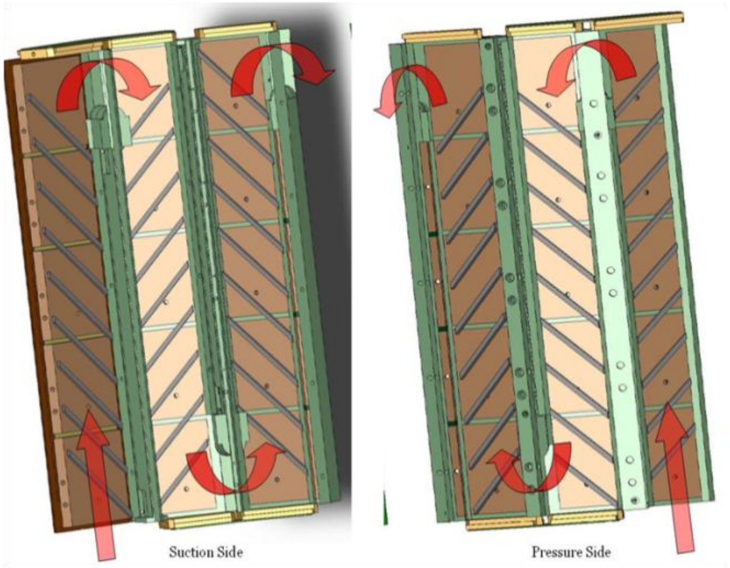

Figure 40 Schematic view of serpentine internal coolant passages with 45° angled rib arrangement.

III.C.3. Working Fluid

The reason for refrigerant R134a to be selected as working fluid in this research was mainly based on density. The density at designed test condition is 18 kg/m^3, and Prandtl number (Pr) is 0.8, both characteristics are comparable with that compressed air at gas turbine operating condition. R134a has less hazard issues as it is inert and non-combustible at room temperature. R134a flow in this study is composed by two flow loops, a primary boiler loop and a secondary heat exchanger loop; schematic R134a flow loop is shown in **Figure 41.**

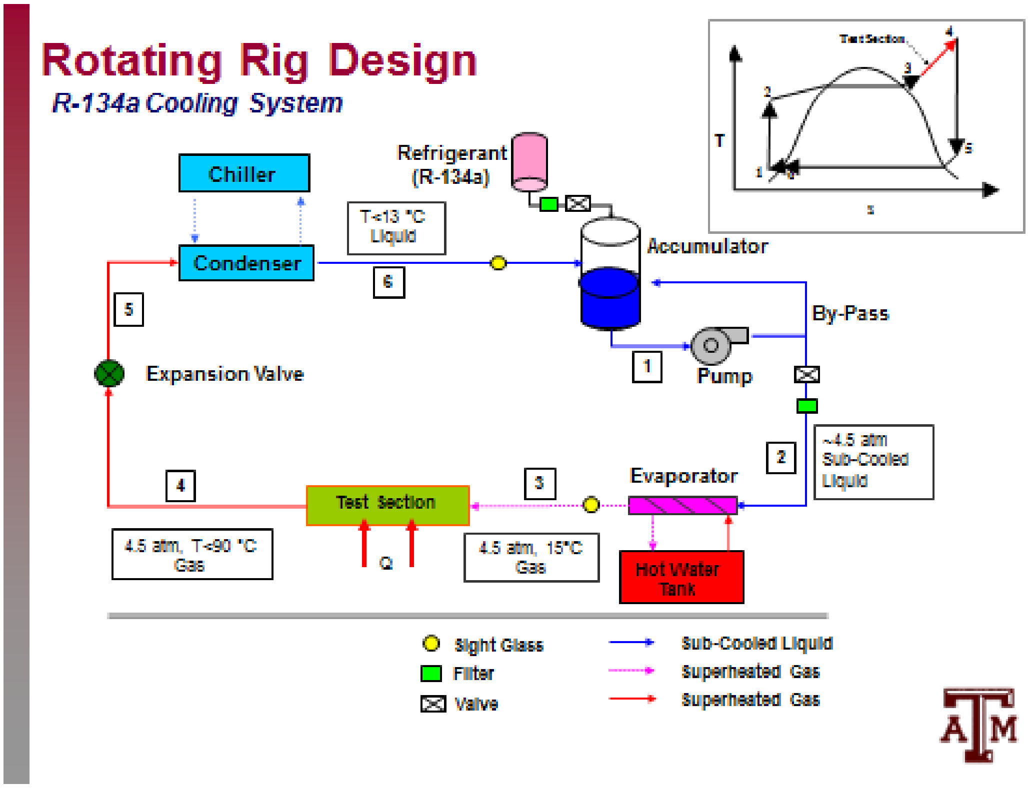

Figure 41 Refrigerant R134a vapor working loop schematic.

The R134a vapor circulated through test section is generated by the primary boiler loop. After passes through test section, this vapor than circulates through a condenser where heat is extracted from vapor via a non-contact heat exchanger. The working fluid employed in secondary heat exchanger loop is also R134a. The purpose of the secondary loop is to absorb energy from R134a circulated in primary loop that condensed in the condenser. Table 3 displays the actual Reynolds and Mach number of each nominal case in each channel.

Table 3 Nominal and actual Reynolds numbers in internal cooling study

Nominal Case	Reynolds Number	30k	40k	50k	60k	70k
1^{ST} Passage	Reynolds Number	30.8k	41.5k	49.5k	62.0k	70.0k
	Mach Number	0.0066	0.0089	0.0106	0.0132	0.0149
2^{ND} Passage	Reynolds Number	33.9k	45.7k	54.5k	68.2k	77.0k
	Mach Number	0.0081	0.0109	0.0130	0.0162	0.0183
3^{RD} Passage	Reynolds Number	35.7k	48.1k	57.3k	71.8k	81.0k
	Mach Number	0.0125	0.0168	0.0200	0.0251	0.0283

R134a flow rate that circulates through test section was monitored by both a Coriolis flow-meter at upstream test section and a rotameter located downstream. Flow rates reported by both the flow meters have also been cross-checked by each other. The correlation followed a linear trend, which coincides with common understandings. Working fluid pressure is controlled to 365.42 kPa (53.0 psi) (gauge) immediately upstream of the upstream rotary union using a PID controller. And the R134a temperature is controlled to 15.56 °C (60° F) to minimize ambient external water-vapor condensation on fluid pipe-related issues. Flow rate is controlled through a PID actuated needle valve and this value is set to be in a range from 0.47 kg/min to 1.0 kg/min resulting in a range of Reynolds numbers from 32,000 to 70,000. Rotating speed of this study was kept at 300 rpm. It was also calibrated in terms of controller input frequencies. Special efforts on balancing the assembly were necessary to ensure the safety of the test section, the signal (TC) and power transmitting cables, the housing and operating personnel.

III.C.4. Data Acquisition

T-type (copper-constantan) thermocouples are embedded at geometry centers in each copper plate. The Biot number (Bi) is a dimensionless parameter defined as a ratio of internal thermal (conduction) resistance to surface film (convection) resistance. A small Bi value implies the heat conduction inside the copper plate is much faster than heat convection away from the surface and the temperature gradient is negligible. In ensuring these copper plates are isothermal for experimental considerations, the Biot number for all copper plates work out to less than 0.1. The thermocouples as well as the heater wires are soldered to feed-through wires which are routed to the stationary frame through a 200 channel slip-rings assembly positioned along the rotation axis. The thermocouples are designed to record real time temperature information in each region, while the heater wires are to provide necessary electric power for energizing individual heaters present in test section. The input power to each heater is controlled by input voltage, and the control was performed by an external variable transformer set. A Labview based program and a NI SCXI chassis/ terminal block assembly are used to acquire and record temperature data from thermocouples. Table 4 displays the actual rotation number for each nominal case in each channel.

Table 4 Rotation number studied for nominal Reynolds numbers.

Nominal Reynolds Num.	30k	40k	50k	60k	70k
1^{ST} Passage	0.5320	0.4367	0.3503	0.2882	0.2511
2^{ND} Passage	0.3888	0.3191	0.2560	0.2106	0.1835
3^{RD} Passage	0.1716	0.1408	0.1130	0.0930	0.0810

III.D. Data Reduction

III.D.1. Heat Transfer Enhancement

This study investigates regionally averaged heat transfer coefficient (h) at various locations in the full scale rotation facility. Silicone rubber heaters are used to generate heat which is dissipated within the test section. The resistance of each heater (R) is measured before each run. The electrical potential (V), supplied across each heater is controlled by individual variable transformer and is measured by a multi-meter. The thermal power ($Q_{in,}$) introduced by heaters can be determined.

(5) $Q_{in} = V^2/R$

Each heater provides constant heat flux along its length. Changing the voltage input across the heater changes the steady state temperature measured on each copper plate. Since heat transfer coefficients vary from region to region, it is not possible to control the temperature recorded for each plate to a constant and identical value. The electric potentials across the heaters are actively controlled to ensure that the temperatures at central regions for each pass correspond to 65°C. For example, the leading and trailing walls may have a constant heat flux respectively, but they are at different value of constant heat flux in order to keep the temperatures at a central region for each pass correspond to 65°C. The 65°C is arbitrary chosen as a reference to prevent the test model from burnout.

In current study, the regionally averaged heat transfer coefficient is calculated using the net heat transferred from the heated cooper plate (Q_{net}), the heat transfer surface area of the copper plate (A), the regionally averaged temperature of the copper plate (T_w), and the local bulk mean temperature of the working fluid flow in the channel (T_b). Therefore, the regionally averaged heat transfer coefficients for a copper plate can be defined as

(6) $h = (Q_{net} /A)/(T_w - T_b)$

The net heat transferred from the copper plate to the working flow can be calculated as

(7) $Q_{net} = Q_{in} - Q_{loss}$

To determine the external heat losses (Q_{loss}) escaping from the test section during each experiment, two steady state heat loss calibration tests are performed. In order to minimize natural convection effects during heat loss calibration tests, an insulating material was placed inside of flow channel. A heat loss calibration test is successful when the total power input to the test section reaches equilibrium with the environment (wall temperatures converged to a steady constant value). The researchers studied the Q_{loss} at two temperatures; one lower than the range encountered in the test, and one higher. Based on results of both temperatures, a heat loss characteristic is obtained for each of the copper plates. The heat loss occurs in experiment, is then determined by interpolating between the two sets of calibration data. Heat loss tests were performed under both stationary and 300 rpm.

The regionally averaged wall temperature (T_w) is directly measured by the thermocouple embedded in the blind hole on the backside of each copper plate. Since copper has a very high thermal conductivity, the temperature of each copper plate is assumed to be uniform. Two thermocouples are used to measure the R134a flow temperature at channel inlet and exit respectively.

The local bulk mean temperature (T_w) is based on energy balance method. Eq. (8) illustrate the concept of determine the bulk mean temperature by energy method. For a given region i ($1 \leqq i \leqq 15$) the energy balance equation is

$$(8)\ \left(T_{b,out} - T_{b,in}\right)_i = \sum_i Q_{net} / \left(m \cdot c_p\right)$$

As listed in Eq. (8), $T_{b,in}$ and $T_{b,out}$ indicate the bulk mean temperature at the inlet and exit of region *i,* respectively. The net heat transferred to the working fluid, from all copper plate-heater surfaces at region *i*, is divided by the product of mass flow rate (m) and the specific heat (c_p) of the of working fluid. Thus, for the first region at the channel inlet (region 1), $T_{b,in}$ is the actual working fluid temperature measured by the channel inlet thermocouple. Heat energy is added to the working fluid in region =1 from all four surrounding surfaces. This resulted in working fluid bulk mean temperature to increase at the exit of region =1. At the exit of region=1, the bulk mean temperature is denoted as $T_{b,out}$, which is the inlet temperature for region=2. The local bulk mean temperature (T_b) in region *i* is determined as the average of both $T_{b,in}$ and $T_{b,out}$.

The Dittus-Boelter/McAdams correlation for heating ($T_w > T_b$) is used in this study to provide a basis of comparison in stationary cases. The correlation from Kays et al. [61] served the purpose of calculating the Nusselt number (Nu_0) for fully developed turbulent flow through a smooth stationary pipe. Therefore, Nu/Nu_0 ratio, the parameter used to present heat transfer enhancement results of stationary cases in this study is given as

$$(9)\quad \left(\frac{Nu}{Nu_0}\right) = \left(\frac{h \cdot D_h}{k}\right)\left(\frac{1}{0.023\,\mathrm{Re}^{0.8}\,\mathrm{Pr}^{0.4}}\right)$$

In Eq. (9), h is calculated through Eq. (6). All refrigerant 134a properties are based on the energy balance method of the working fluid bulk temperature with a Prandtl number (*Pr*) of 0.8. And the Nu/Nu_0 ratio is correlated against Reynolds number (*Re*) for stationary cases.

In order to isolate the effect of rotation and to eliminate the Reynolds number effect, data for rotating conditions is presented as a ratio: Nu/Nu_s, where Nu_s is the measured stationary Nusselt number for the same Reynolds number. In this study, the Nu/Nu_s ratio is correlated against rotation number (*Ro*) for rotation cases.

III.D.2. Uncertainties

The main source of error in determining the Reynolds number (*Re*) is the resolution of the Coriolis flow-meter to measure the mass-flow rate (0.01 lb/min, 0.004536 kg/min) and temperature measurements to estimate the properties of R134a accurately. Reynolds numbers (*Re*) are thus estimated with an error of less than 1%. The error estimate for the Nusselt number (*Nu*) is 4%. The error estimate for the Nusselt number (*Nu*) enhancement due to rotation (Nu/Nu_s) is 6%. The measured resistance of the heaters is found to change less than 0.5% for the operating range of temperatures.

III.E. Result and Discussions

III.E.1. Stationary Channel Results

The serpentine channel has the largest cross-section in the radial outward flow (first passage), then radial inward flow (second passage), and radial outward flow (third passage). The Reynolds numbers (*Re*) based on the first passage cross-section varied from 30,000 to 70,000, the Mach numbers from 0.0066 to 0.0149. **Table 4** shows the Reynolds number and Mach number gradually increase from the first passage to the third passage. Results acquired for stationary channels are reported for the leading and trailing surfaces of the interested regions. They are the mid-region of each channel (regions 3, 8, and 13), as well as the regions before and after the tip and hub turns (regions 5 and 6, 10 and 11). **Figure 42** shows the mid-region results as Nu/Nu_0 vs. Reynolds number and **Figure 43** shows the tip and hub turn results.

A large volume of open literature exists on the subject of roughened channel heat transfer. Through **Fig42 and 43**, the study generally followed the trends in open literature, i.e., the 45 degree angled rib turbulators increase the heat transfer to around 2-3 times of the Dittus-Boelter correlation. According to **Figures 42 and 43**, it is clear that this study (green color) coincided with high Reynolds numbers data (yellow color) at Re = 70,000. The high Reynolds numbers data (Re = 75,000-165,000) were reported by Rallabandi et al. [62]. The high Reynolds number study was finished with the same method on the same experiment setup. Correlations were generated by combining both sets of data for the stationary channel. For the first passage, the Nu/Nu_0 enhancement declines as the Reynolds number increased from 30,000 to 70,000 and then levels off after 70,000 to 165,000. Results for Re=50,000 (Nu/Nu_0 =2.9) and 70,000 (Nu/Nu_0 =2.6) were 10% and 20% lower than those for Re=30,000 (Nu/Nu_0 =3.2) respectively. Similar results were noticed for the second and the third passages.

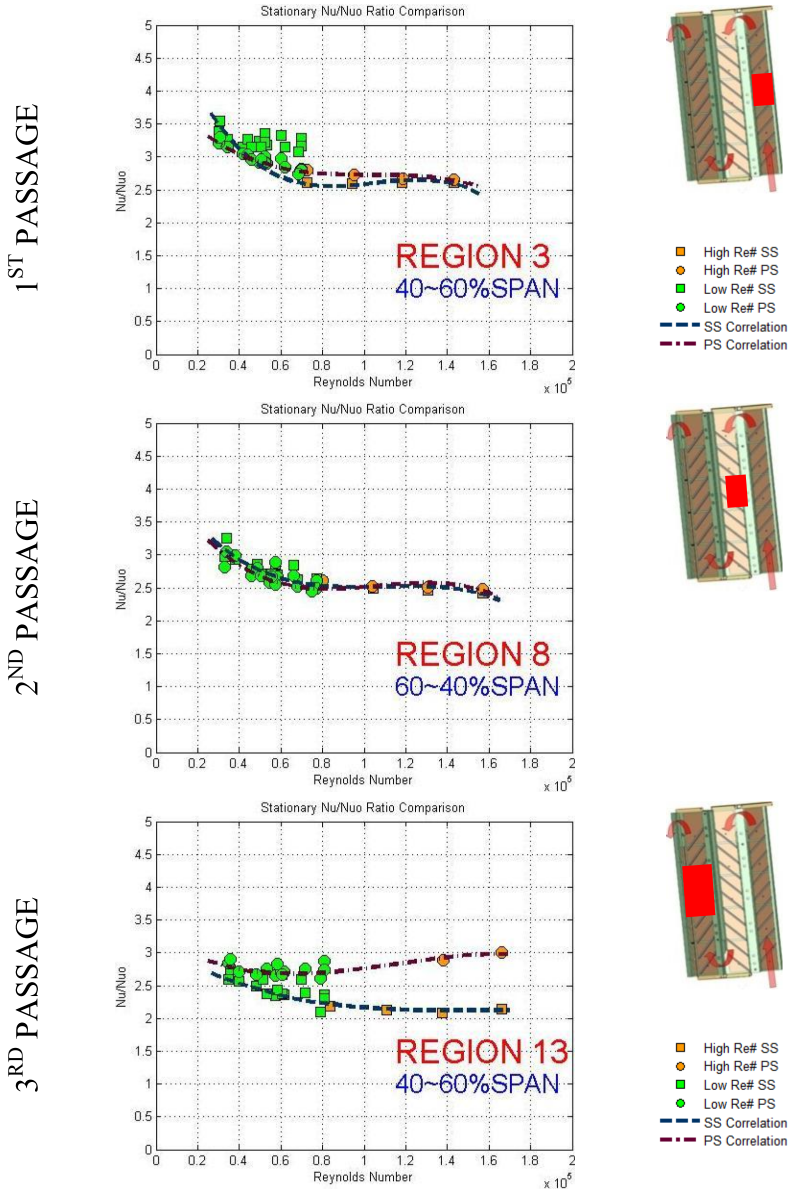

Figure 42 Re effect: variation of Nu/Nu$_0$ at channel mid-regions.

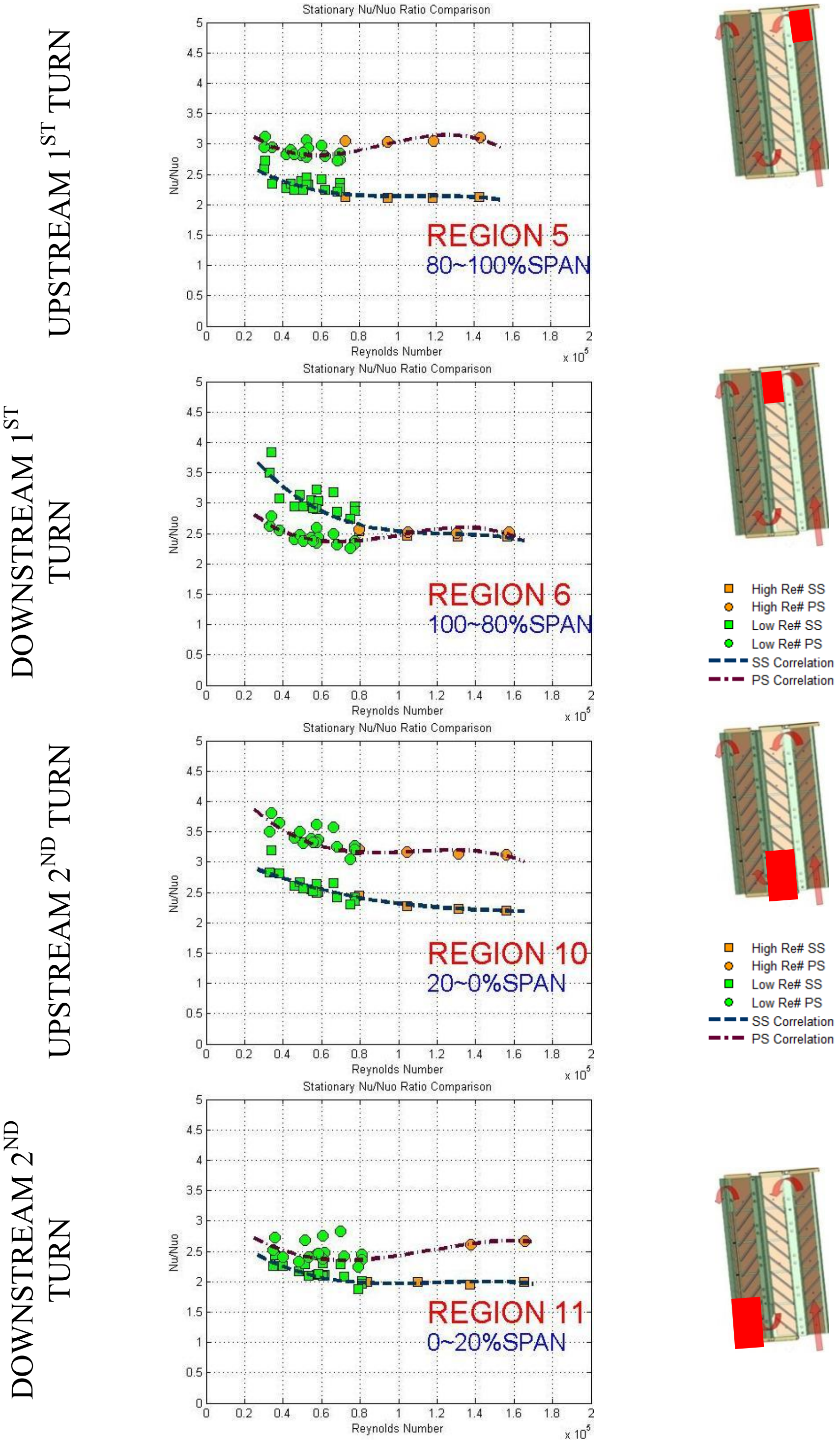

Figure 43 Re effect: variation of Nu/Nu_0 at channel tip and hub turn regions.

Since the channel in consideration is a ribbed channel, and the Reynolds numbers are also high, these two reasons contribute in a significant high turbulence level in the flow passages. The high turbulence level results in a relatively short development length and a relatively constant heat transfer coefficients between leading wall (SS, suction side) and trailing wall (PS, pressure side). However, heat transfer coefficients between leading wall and trailing wall can be very different in the tip turn regions (5, 6) and hub turn regions (10, 11) since these regions are connected by different channel cross-sections through a sharp U-turn.

Asymmetry in the Nu/Nu_0 results between the pressure and suction sides can be attributed to three factors: (1) geometry, trapezoidal cross section of the channel results in a deviation in symmetry from the rectangular channel case; (2) staggered rib configurations; and (3) vortices triggered by relative angularity and change in cross section (as indicated in Fig.8, before and after each turns) between the first, second and third passages.

III.E.2. Rotating Channel Results

For rotating channel, both Coriolis and rotation induced buoyancy forces are present in a serpentine rotating passage, the internal flow field as well as heat transfer enhancements are thus altered. For comparison, **Figure 44** displays the Nusselt Number enhancement along stream-wise region number for leading (suction) and trailing (pressure) surfaces for Re= 50,000 stationary and 300 rpm cases.

As indicated in **Figure 44**, for 300 rpm rotation, the trailing surface shows an increase in heat transfer; the second passage shows a relative suppression on heat transfer on the trailing surface. The trend in the third passage is similar to that in the first passage. This effect is attributed to the Coriolis force: for radially outward passages, an enhancement in heat transfer is seen on trailing surfaces and vice-versa radially inward passages. Han et al. [40] documented a large body of open literature which explains this effect in detail. The flow passage in this study was to simulate an actual internal cooling configuration of commercial land base gas turbine blade in full scale. As illustrated in **Figure 40**, between the passages, the non-parallel turns, varying hydraulic diameter and aspic ratio, as well as the trapezoid shaped passage cross-sections introduced a combine effect to the heat transfer phenomena. And these are the reasons that the results of present study deviated from the documented literatures.

Similar data have been obtained at the stationary and 300 rpm for Reynolds numbers ranging from 30,000 to 70,000. **Table 4** shows the relations between Reynolds number, and rotation number in the first, second, and third passage, respectively.

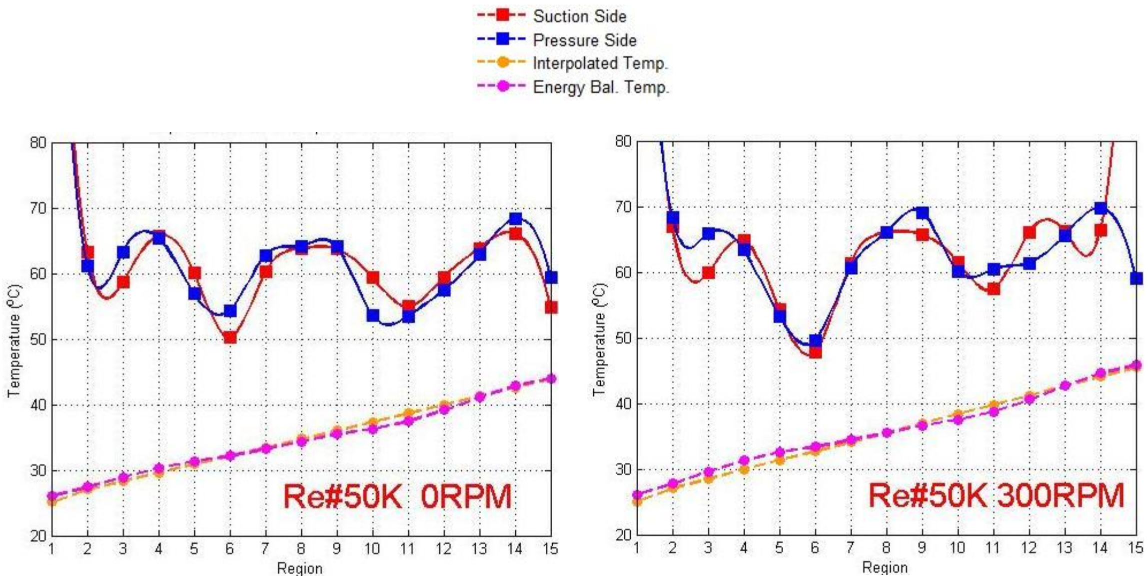

(a) Stationary case Temp. (b) Rotation case Temp.

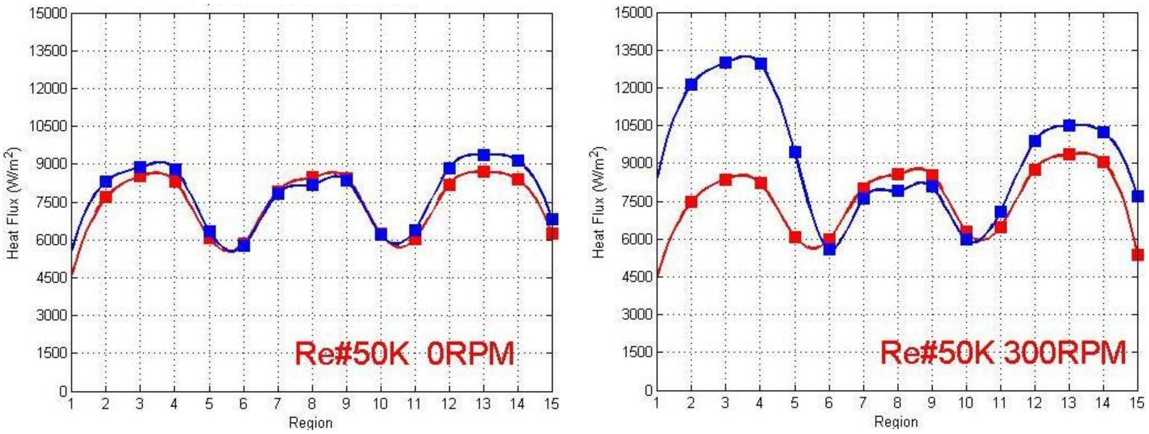

(c) Stationary case heat transfer (b) Rotation case heat transfer

Figure 44 Effect of rotation on the variation of internal Nu/Nu_0 along the three passage serpentine channel

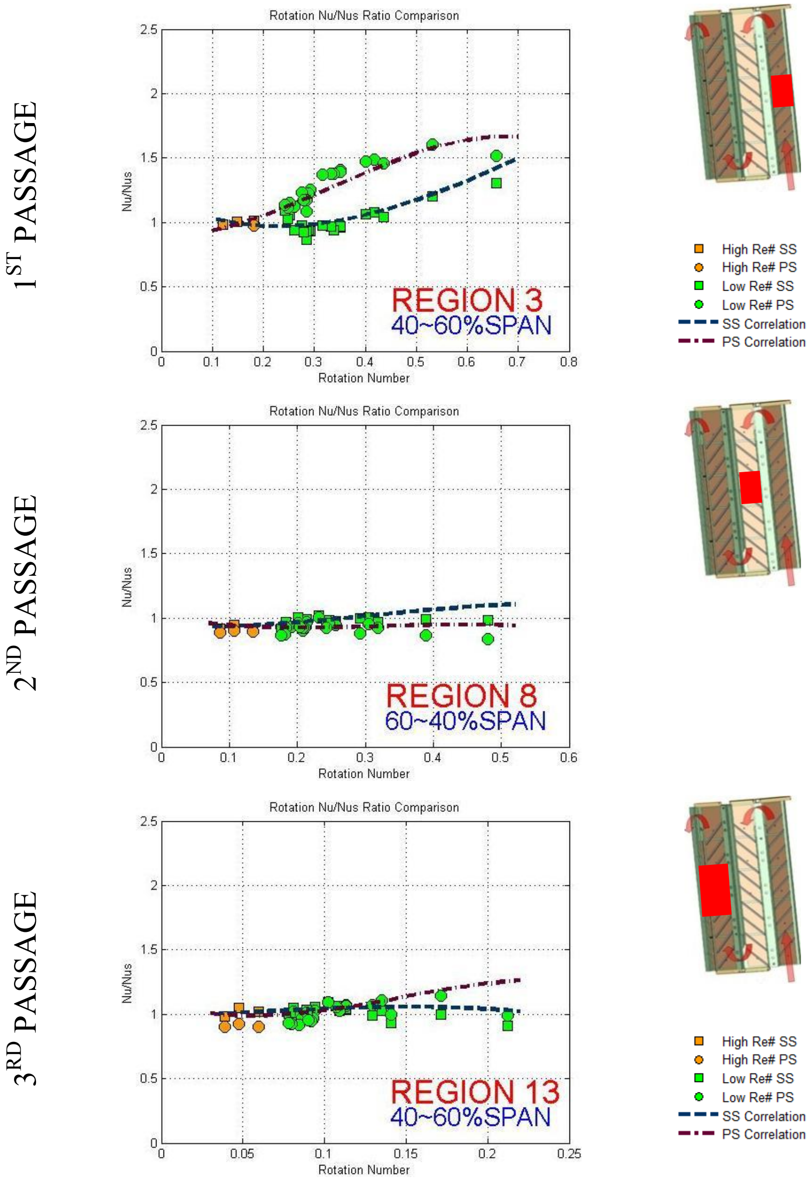

Figure 45 Ro effect: variation of Nu/Nu_s at channel mid-regions.

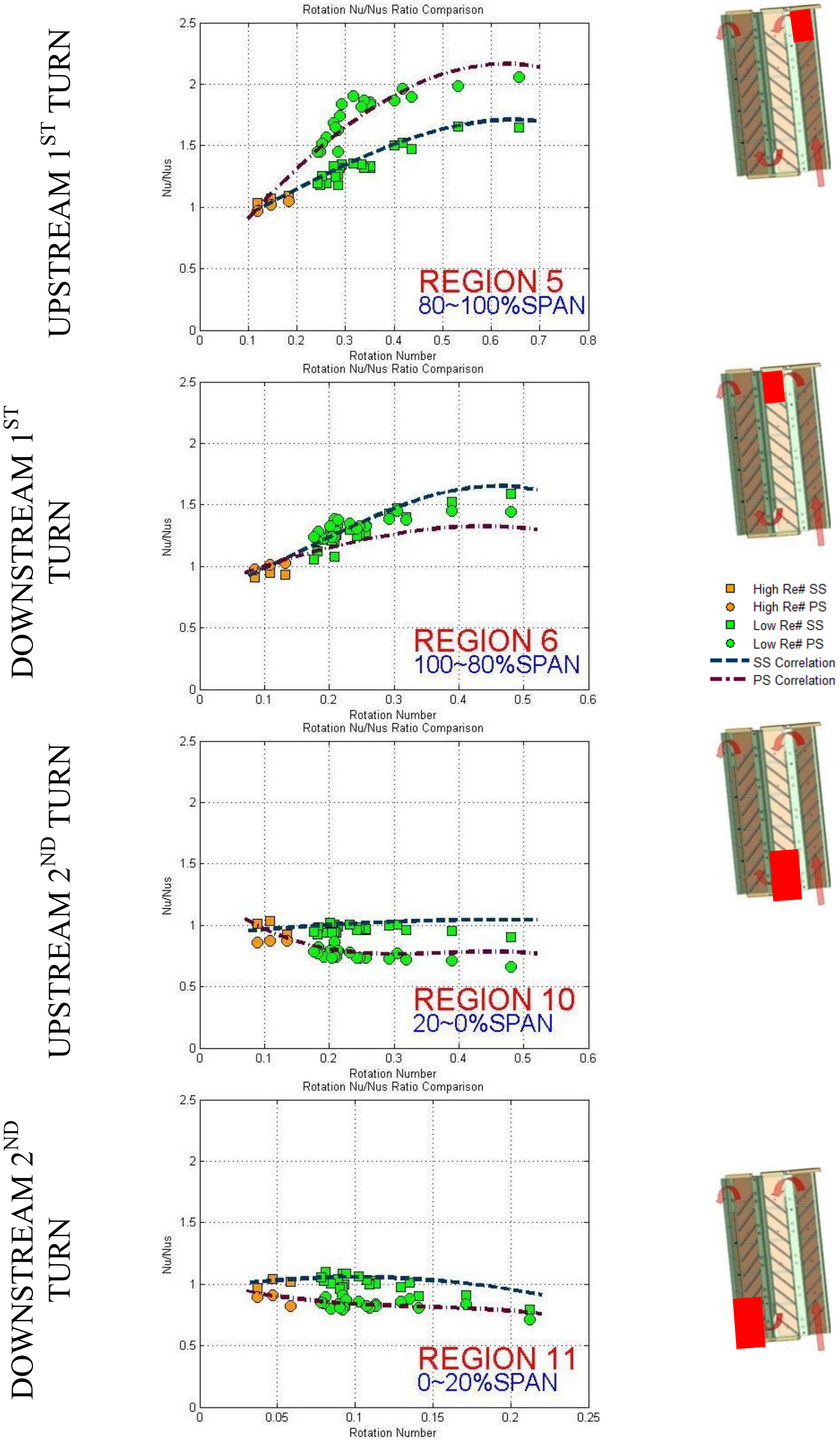

Figure 46 Ro effect: variation of Nu/Nu_s at channel tip and hub turn regions.

The Coriolis force creates a pair of counter-rotating vortices whose net effect is to ‘thin’ out the boundary layer on one side while thicken the boundary layer on the other side. In radially outward passages (1^{st} and 3^{rd} passages) an increase in Nusselt numbers (*Nu*) due to rotation is observed on the trailing surfaces.

The effect of rotation, in the first passage is to increase the heat transfer coefficients on both leading (SS, suction side) and trailing (PS, pressure side) surfaces as shown in **Figure 45** region 3, except there is a drop on leading surface heat transfer at Ro around 0.3. It is also true for the leading and trailing surfaces before and after tip turn regions (5 and 6 shown in **Figure 46)**. However, in the second passage (**Figure 45** region8), and before and after hub turn (**Figure 46** regions 10 and 11), the effect of rotation is to suppress the local heat transfer on both leading and trailing surfaces. This can be attributed to the effect of sharp hub turn connecting the second and third passage which has very different cross-section, shape and orientation. In addition, since the centrifugal force acts radially outward (i.e. heavier fluid particles are pushed outwards) in a rotating frame, the buoyancy force acts in the same direction to bulk coolant inward flow. The buoyancy parameter *Bo* is proportional to the square of rotation number *Ro* and the temperature difference between coolant and wall at a given channel location/region [48]. Therefore, local buoyancy force increases with increasing rotation number and wall-to-coolant temperature difference in the cooling passage. Warmer (i.e. lighter) fluid pockets are subjected to a net force which acts radially inward in all the 3 passages.

In the first and third passages, the buoyancy force (directed radially inward) is opposing to the bulk fluid flow. In the second pass, the buoyancy force aligns itself with the bulk fluid flow. A survey of literature [64, 65] indicates that a reduction in heat transfer coefficient is indeed expected in turbulent internal flow-fields when buoyancy is aligned with bulk flow. This phenomenon is attributed to an augment in turbulence suppression due to an increase in momentum aligned to the bulk flow direction in warm fluid pocket. In particular, heat transfer coefficients on the pressure side (trailing wall) in the hub turn region (10 and 11 in **Figure 46**) reduce up to 25% at Ro around 0.2. These hub turn regions are important for design consideration.

III.E.3. Heat Transfer Enhancement Correlations

Figures 42, 43, 45 and 46 also show the correlations that have been developed for both leading (suction side, SS) and trailing (pressure side, PS) surfaces at each region. These correlations are useful to predict the heat transfer enhancement under stationary and rotation conditions. However, since all data acquired in this study is based on the three passage internal cooling geometry provided by Siemens Energy Inc. It is worthy to point out the usage of these correlations should be limited to similar geometry, and inflow condition.

III.E.3.1. Stationary Heat Transfer Enhancement Correlations

A third order polynomial (Eq.10) was employed to fit the stationary Nu/Nu_0 against Reynolds number (*Re*) data. The coefficients are shown in **Table 5**.

$$(10) \quad \frac{Nu}{Nu_0} = a_0 + a_1 \mathrm{Re} + a_2 \mathrm{Re}^2 + a_3 \mathrm{Re}^3$$

Table 5 Stationary correlation formulae

REGION	FLOW SPAN	SURFACE	a_0	$a_1 x10^{-5}$	$a_2 x10^{-10}$	$a_3 x10^{-16}$
R3	OUT FLOW 40~60%	SUCTION	5.39	-8.65	8.56	-27.09
		PRESSURE	4.05	-3.81	3.68	-11.88
R5	OUT FLOW 80~100%	SUCTION	3.16	-2.86	2.66	-8.13
		PRESSURE	3.91	-4.50	5.70	-20.71
R6	IN FLOW 100~80%	SUCTION	4.84	-5.47	4.32	-11.58
		PRESSURE	3.66	-4.58	5.06	-16.69
R8	IN FLOW 60~40%	SUCTION	4.26	-4.96	4.63	-14.14
		PRESSURE	4.28	-5.52	5.46	-17.11
R10	IN FLOW 20~0%	SUCTION	3.26	-1.66	0.87	-1.59
		PRESSURE	4.81	-4.86	4.64	-14.28
R11	OUT FLOW 0~20%	SUCTION	3.03	-2.82	2.42	-6.66
		PRESSURE	3.34	-3.26	3.29	-9.50
R13	OUT FLOW 40~60%	SUCTION	3.12	-1.92	1.23	-2.58
		PRESSURE	3.24	-1.97	2.09	-5.99

Table 6 Rotation correlation formulae

REGION	FLOW SPAN	SURFACE	a_0	a_1	a_2	a_3
R3	OUT FLOW 40~60%	SUCTION	1.17	-1.82	4.60	-1.89
		PRESSURE	0.88	0.06	495	-4.91
R5	OUT FLOW 80~100%	SUCTION	0.73	2.02	0.77	-2.38
		PRESSURE	0.44	4.98	-2.77	-1.25
R6	IN FLOW 100~80%	SUCTION	0.77	1.78	4.74	-9.63
		PRESSURE	0.83	1.75	-0.22	-2.72
R8	IN FLOW 60~40%	SUCTION	0.94	-0.20	2.26	-2.39
		PRESSURE	1.01	-0.96	3.39	-3.45
R10	IN FLOW 20~0%	SUCTION	0.92	0.50	-0.42	-0.17
		PRESSURE	1.33	-4.81	13.12	-11.27
R11	OUT FLOW 0~20%	SUCTION	0.96	1.91	-9.16	-2.40
		PRESSURE	1.04	-3.81	23.27	-53.45
R13	OUT FLOW 40~60%	SUCTION	0.98	0.54	2.69	-19.52
		PRESSURE	1.08	-3.68	41.00	-93.33

III.E.3.2. Rotation Heat Transfer Enhancement Correlations

Heat transfer enhancement *Nu/Nus* is correlated against rotation number (*Ro*). Eq.11 shows the formula and **Table 6** shows the coefficients.

$$(11)\quad \frac{Nu}{Nu_s} = a_0 + a_1 Ro + a_2 Ro^2 + a_3 Ro^3$$

III.F. Conclusions

In the A significant amount of heat transfer coefficient data is obtained on a 1:1 scaled turbine blade with internal coolant passages similar with real design conditions. Results obtained reflect the complicated nature of flow-field (effects of angled ribbed wall, channel shape and orientation, tip and hub turns, rotation, etc.). Stationary and rotation heat transfer enhancement correlations were provided regionally in terms of Reynolds number (*Re*) and rotation number (*Ro*) respectively.

From the research work performed in this study, the following observations and conclusions can be made.

1. Using Freon R134a vapor as a working fluid, the non-dimensional Reynolds numbers and rotation numbers corresponding to actual engine cooling conditions can be more easily simulated due to its higher density.
2. For stationary serpentine channel, heat transfer coefficients between leading wall and trailing wall are very different before and after the tip turn as well as before and after the hub turn. This is because the channel cross-section, shape and orientation are

very different in the tip and hub turns and cause asymmetric flows after the sharp turns.

3. Rotation enhances heat transfer coefficients in the first passage radial outward flow as well as in the regions before and after the tip turn. However, rotation reduces heat transfer in the second passage radial inward flow as well as in the regions before and after the hub turn. This is attributed to the buoyancy effect in the hub turn region.
4. For stationary serpentine passage, heat transfer correlation has been developed for Reynolds numbers from 30,000 to 170,000. For rotating serpentine passage, heat transfer correlation has been developed for rotation numbers from 0.0 to 0.6.
5. Low Mach number concern: Special attention on region 10 (2nd passage inflow span 20-0%): Re = 54475, Ma = 0.0142, Ro = 0.256, Nu/Nu_s on suction wall = 0.9654, Nu/Nu_s on pressure wall = 0.7354, this implies that rotation might decrease heat transfer coefficients up to 25% on pressure side near hub turn inlet region. Similar trend was also obtained at region 11 (3rd passage outflow span). Designers should be cautious that rotation might cause heat transfer reduction in the hub turn region over a wide range of low Mach number internal flows.

CHAPTER IV

SUMMARY

The pressure sensitive paint is a reliable and efficient tool in adiabatic film-cooling effectiveness measurement. Blowing ratio in lower Mach number and density side, the negative trend on film cooling effectiveness is more obvious. However, the trend reverses while consider high density coolant at supersonic flow. High density coolants prevent film cooling jets to lift-off, resulting in a higher film cooling effectiveness. DR=2.0 and DR=1.5 are the optimum coolant density in terms of whole vane and downstream (potential shock) region film cooling effectiveness respectively. Exit Mach number exerts a negative effect on cooling effectiveness in high density ratio cases. However, at close-to engine condition (M=1.6, DR=2.0) case, near the cooling configuration the effect is marginal.

In the internal serpentine coolant passage study, this research experimentally proved that the rotation does not always contribute the heat transfer in a positive way. Results indicated rotation enhances heat transfer coefficients in the first passage radial outward flow as well as in the regions before and after the tip turn. However, the rotation reduces heat transfer in the second passage radial inward flow as well as in the regions before and after the hub turn. This is one of the major founding in turbine blade internal cooling passage research. Employing gasus Freon R134a as working fluid is another spot light of this work. Since the high Reynolds numbers and low rotation numbers corresponding to actual engine cooling conditions can be more easily simulated due to its density.

REFERENCES

1. Han, J. C., Dutta, S., and Ekkad, S. V., 2001 *Gas Turbine Heat Transfer and Cooling Technology*, Taylor & Francis, New York, 2001, Chapter 3.
2. Goldstein, R. J., 1971, ‘‘Film Cooling,’’ *Advances in Heat Transfer*, Academic Press, San Diego, Vol. 7, pp. 321-379.
3. Bunker, R. S., 2005 “A review of shaped hole turbine film-cooling technology,” *Journal of Heat Transfer*, Vol.127, n4, pp. 441-453
4. Bogard, D. G.. and Thole,K. A., 2006, ‘‘Gas Turbine Film Cooling,’’ *Journal of Propulsion and Power*, Vol. 22, n2, pp. 249-270.
5. Han, J.C., and Rallabandi, A. P., 2010, ‘‘Turbine Blade Film Cooling Using PSP Technique,’’ *Frontiers in Heat and Mass Transfer*, Vol. 1, n1, pp. 1-21.
6. Goldstein, R.J., Eckert, E.G., and Burggraf, R., 1974, “Effects of Hole Geometry and Density on Three Dimensional Film Cooling,” *Int. J. of Heat and Mass Transfer*, **17**, pp. 595–606.
7. Thole, K., Gritsch, M., Schulz, A., and Wittig, S., 1996, ‘‘Flowfield Measurements for Film Cooling Holes With Expanded Exits,’’ *ASME Paper No.96-GT-174*.
8. Gritsch, M., Schulz, A., and Wittig, S., 1997, ‘‘Adiabatic Wall Effectiveness Measurements of Film-Cooling Holes With Expanded Exits,’’ *ASME Paper No.97-GT-164.*
9. Yu, Y., Yen, C.-H., Shih, T. I.-P., Chyu, M. K., and Gogineni, S., 1999, ‘‘Film Cooling Effectiveness and Heat Transfer Coefficient Distributions around

Diffusion Shaped Holes,'' *ASME Paper* No. 99-GT-34.

10. Schmidt, D. L., Sen, B., and Bogard, D. G., 1994, ''Film Cooling With Compound Angle Holes: Adiabatic Effectiveness,'' *ASME Paper* No. 94-GT-312.
11. Ekkad, S., Zapata, D., and Han, J., 1997, ''Film Effectiveness Over a Flat Surface With Air and CO_2 Injection Through Compound Angle Holes Using a Transient Liquid Crystal Image Method,'' *Journal of Turbomachinery,* Vol. 119, pp. 587.
12. Wright, L. M., Gao, Z., Varvel, T. A., and Han, J. C., 2005, ''Assessment of Steady State PSP, TSP, and IR Measurement Techniques for Leading Edge Film Cooling,'' *Proceedings of the ASME Summer Heat Transfer Conference.*
13. Goldstein, R. J., and Jin, P., 2001, "Film Cooling Downstream of a Row of Discrete Holes With Compound Angle," *Journal of Turbomachinery,* Vol. 123, pp. 222-230.
14. Ito, S., Goldstein, R. J., Eckert, E. R. G., 1978, ''Film Cooling of a Gas Turbine Blade,'' *Journal of Engineering for Power,* Vol. 113, pp. 476-481.
15. Liu, K., Yang, S. F., and Han, J. C., 2014, ''Influence of Coolant Density on Turbine Blade Film Cooling with Axial and Compound Shaped Holes,'' *J. Heat Transfer* 2014; 136(4):044501-044501-5 HT-12-1441.
16. Li, S. J., Yang, S. F., and Han, J. C.,2013, "Effect of Coolant Density on Leading Edge Showerhead Film Cooling Using the Pressure Sensitive Paint Measurement Technique," *J. Turbomach.* 136(5), 051011-051011-10. TURBO-13-1145.
17. Liu, K., Yang, S. F., and Han, J. C., 2014, ''Influence of Coolant Density on

Turbine Platform Film Cooling with Stator-Rotor Purge Flow and Compound Angled Holes,'' *J. Thermal Sci. Eng. Appl.* 2014; 6(4):041007-041007-9. TSEA-13-1182.

18. Goldstein, R.J., Eckert, E.G., Eriksen, V.L., and Ramsey, J.W., 1970, "Film Cooling Following Injection Through Inclined Circular Tubes," *Israel Journal of Technology*, **8**, pp. 145-154.
19. Cho, H.H., Rhee, D.H., and Kim, B.G., 2001, "Enhancement of Film Cooling Performance Using a Shaped Film Cooling Hole with Compound Angle Injection,"*JSME International Journal*, Series B, **44**, No. 1, pp. 99-110.
20. Mhetras, S., and Han, J.C., 2006 "Effect of Unsteady Wake on Full Coverage Film-Cooling Effectiveness for a Gas Turbine Blade," *AIAA Paper No. AIAA-2006-3404*.
21. Narzary, D.P., Gao, Z., Mhetras, S., and Han, J.C., 2007 "Effect of Unsteady Wake on Film-Cooling Effectiveness Distribution on a Gas Turbine Blade with Compound Shaped Holes," *ASME Paper* No. GT2007-27070.
22. Gao, Z., Narzary, D.P., Mhetras, S., and Han, J.C., 2008, "Full-Coverage Film Cooling for a Turbine Blade With Axial-Shaped Holes," *Journal of Thermophysics and Heat Transfer*, Vol. 22, n1, pp. 50-61.
23. Pedersen, D.R, Eckert, E.R.G., and Goldstein, R.J., 1997, "Film Cooling with Large Density Differences Between the Mainstream and Secondary Fluid Measured by the Heat-Mass Transfer Analogy," *ASME Journal of Heat Transfer,* **99**, pp. 620-627.

24. Sinha, A.K., Bogard, D.G., and Crawford, M.E., 1991, “Film Cooling Effectiveness Downstream of a Single Row of Holes with Variable Density Ratio,” *ASME Journal of Turbomachinery*, **113**, pp 442-449.
25. Ethridge, M. I., Cutbirth, M. J., Bogard, D. G., 2001, ‘‘Scaling of Performance for Varying Density Ratio Coolants on an Airfoil With Strong Curvature and Pressure Gradient Effects, ’’ *Journal of Turbomachinery,* Vol. 123, pp. 231-237.
26. Furukawa, T. and, Ligrami, P. M., 2002, ‘‘Transonic Film Cooling Effectiveness from Shaped Holes on a Simulated Turbine Airfoil,’’ *Journal of Thermophysics and Heat Transfe*, Vol. 16, pp. 228-237.
27. Kodzwa, P. M., and Eaton, J. K., 2010, ‘‘Film Effectiveness Measurements on the Pressure Surface of a Transonic Airlfoil,’’ *Journal of Propulsion and Power*, Vol. 26, n4, pp. 837-847.
28. Kodzwa, P. M., and Eaton, J. K., 2013, ‘‘Heat Transfer Coefficient Measurements on the Film Cooled Pressure Surface of a Transonic Airlfoil,’’ *J. Turbomach.* 135(6), 061011, TURBO-11-1097.
29. Nicoll, W., and Whitelaw, J., 1967, “The Effectiveness of the Uniform Density, Two-Dimensional Wall Jet (Two-Dimensional Wall Jets Effectiveness Measurements and Calculation Procedure for Injection Conditions),” *Int. J. Heat Mass Transfer*, Vol. 20, pp. 623-639.
30. Kadotani, K., and Goldstein, R. J., 1979, ‘‘On the Nature of Jets Entering a Turbulent Flow Part A: Jet-Mainstream Interaction,*’’ASME J. Eng. Power*, **101**,pp. 459–465.

31. Kadotani, K., and Goldstein, R. J., 1979, “On the Nature of Jets Entering a Turbulent Flow Part B: Film Cooling Performance,” *ASME J. Eng. Power*, **101**, pp.466–470.
32. Mehendale, A.B., and Han, J.C., 1992, “Influence of High Mainstream Turbulence of Leading Edge Film Cooling Heat Transfer,” ASME *J. Turbomach*, **114**, pp. 707-715.
33. Burd, S. W., Kaszeta, R. W., and Simon, T. W., 1998, “Measurements in Film Cooling Flows: Hole L/D and Turbulence Intensity Effects,’’ASME *J. Turbomach*, **120**, pp. 791–797.
34. McLachlan, B., and Bell, J., 1995, “Pressure-Sensitive Paint in Aerodynamic Testing,” *Exp. Therm. Fluid Sci.*, 10, pp. 470–485.
35. Jones, T., 1998, “Theory for the Use of Foreign Gas in Simulating Film Cooling,” *Int. J. Heat Mass Transfer*, Vol. 20, pp. 349-354.
36. Charbonnier, D., Ott, P., Jonsson, M., Cottier, F., and Kobke, T., 2009, “Experimental and Numerical Study of the Thermal Performance of a Film Cooled Turbine Platform,” ASME Paper No. GT2009-60306.
37. Narzary, D. P., Liu, K., Rallabandi, A. P., and Han, J. C., 2010, “Influence of Coolant Density on Turbine Blade Film-Cooling Using Pressure Sensitive Paint Technique,” ASME Paper No. GT2010-22781.
38. Han, J.C. and Huh, M., 2010, “Recent Studies in Turbine Blade Internal Cooling,” Heat Transfer Research, Bezell House, Inc., ISSN 1064-2285, Vol. 41, No. 8, pp. 801-828.

39. Fu, L.W., Wright, L.M., and Han, J.C., 2006, "Buoyancy Effects on Heat Transfer in Five Different Aspect-Ratio Rectangular Channels with Smooth Walls and 45 Degree Ribbed Walls," J. Heat Transfer, Vol. 128, No. 11, pp. 1130-1141.

40. Han, J., C., Glicksman, L., R., and Rohsenow, W., M., 1978, "An Investigation of Heat Transfer and Friction for Rib-Roughened Surfaces," International Journal of Heat and Mass Transfer, Vol. 21, pp. 1143-1156.

41. Han, J., C., Park, J., S., and Lei, C., K., 1985, "Heat Transfer Enhancement in Channels with Turbulence Promoters," ASME Journal of Engineering for Gas Turbines and Power, Vol. 107, No. 1, pp. 628-635.

42. Han, J., C., 1988, "Heat Transfer and Friction Characteristics in Rectangular Channels with Rib Turbulators," ASME Journal of Heat Transfer, Vol. 110, No. 2, pp. 321-328.

43. Han, J., C. and Park, J., S., 1988, "Developing Heat Transfer in Rectangular Channels with Rib Turbulators," International Journal of Heat and Mass Transfer, Vol. 31, No. 1, pp. 183-195.

44. Taslim, M., E., and Lengkong, A., 1998, "45-Degree Staggered Rib Heat Transfer Coefficient Measurements in a Square Channel," ASME J TURBOMACH, Vol. 120, No. 3, pp. 571-580.

45. Rallabandi, A.P., Alkhamis, N., and Han, J.C, 2011, "Heat Transfer and Pressure Drop Measurements for a Square Channel with 45° Round Edged Ribs at High Reynolds Numbers," ASME J TURBOMACH, Vol. 133, No. 3, pp. 031019.

46. Wagner, J., H., Johnson, B., V., and Kopper, F., C., 1991, "Heat Transfer in Rotating Serpentine Passages with Smooth Walls," ASME J TURBOMACH, Vol. 113, pp. 321-330.

47. Johnson, B., V., Wagner, J., H., Steuber, G., D., and Yeh, F., C., 1994, "Heat Transfer in Rotating Serpentine Passages with Trips Skewed to the Flow," ASME J TURBOMACH, Vol. 116, No. 1, pp. 113-123.

48. Han, J., C., Zhang, Y., M., and Kalkuehler, K., 1993, "Uneven Wall Temperature Effect on Local Heat Transfer in a Rotating Two-Pass Square Channel with Smooth Walls," ASME Journal of Heat Transfer, Vol. 114, No. 4, pp. 850-858.

49. Zhang, Y. M., Han, J., C., Parsons, J., A., and Lee, C., P., 1995, "Surface Heating Effect on Local Heat Transfer in a Rotating Two-Pass Square Channel with 60-Degree Angled Rib Turbulators," ASME J TURBOMACH, Vol. 117, No. 2, pp. 272-278.

50. Johnson, B., V., Wagner, J., H., Steuber, G., D., and Yeh, F., C., 1994, "Heat Transfer in Rotating Serpentine Passages with selected Model Orientations for Smooth or Skewed Tip Walls," ASME J TURBOMACH, Vol. 116, pp. 738-744.

51. Dutta, S., and Han, J., C., 1996, "Local Heat Transfer in Rotating Smooth and Ribbed Two-Pass Square Channels with Three Channel Orientations," ASME Journal of Heat Transfer, Vol. 118, No. 3, pp. 578-584.

52. Azad, G.S., Uddin, M.J., Han, J.C., Moon, H.K., Glezer, B., 2002, "Heat transfer in a two-pass rectangular rotating channel with 45-deg angled rib turbulators", ASME J TURBOMACH, 124, No. 2, pp. 251–259.

53. Wright, L.M., Liu, Y.H., Han, J.C., and Chopra, S., 2008, "Heat Transfer in Trailing Edge Wedge-Shaped Cooling Channels under High Rotation Numbers," ASME Journal of Heat Transfer, Vol. 130, No. 7, pp. 071701-1~ 11.

54. Zhou, F., and Acharya, S., 2008, "Heat Transfer at High Rotation Numbers in a Two-Pass 4:1 Aspect Ratio Rectangular Channel with 45 deg Skewed Ribs," J TURBOMACH, Vol. 130, No. 2.

55. Liu, Y.H., Huh, M., Han, J.C. and Moon, H.K., 2010, "High Rotation Number Effect on Heat Transfer in a Triangular Channel with 45°, Inverted 45°, and 90° Ribs," ASME Journal of Heat Transfer, Vol. 132, No. 7, pp. 071702.

56. Huh, M., Lei, J., and Han, J.C., 2012, "Influence of Channel Orientation on Heat Transfer in a Two-Pass Smooth and Ribbed Rectangular Channel (AR=2:1) under Large Rotation Numbers," ASME J TURBOMACH, Vol. 134, Issue 1, pp. 011022.

57. Liu, Y.H., Huh, M., Han, J.C., and Chopra, S., 2008, “Heat Transfer in a Two-Pass Rectangular Channel (AR=1:4) Under High Rotation Numbers,” ASME Journal of Heat Transfer, Vol. 130, No. 8, pp. 081701-1~ 9.

58. M. Huh, J. Lei, Y.H. Liu, J.C. Han, 2011, “High Rotation Number Effects on Heat Transfer in a Rectangular (AR = 2:1) Two-pass Channel”, ASME J TURBOMACH, 113, No. 2, pp. 021001–11.

59. Wright, L. M., Fu, W. L., and Han, J. C., 2005, “Influence of Entrance Geometry on Heat Transfer in Rotating Rectangular Cooling Channels (AR=4:1) with Angled Ribs,” J. of Heat Transfer, Vol. 127, April, pp. 378-387.

60. Fu, W.L., Wright, L.M., and Han, J.C., 2005, “Heat Transfer in Two-Pass Rotating Rectangular Channels (AR=1:2 and AR=1:4) with 45° Angled Rib Turbulators,” ASME J TURBOMACH, Vol. 127, January, pp. 164-174.

61. Kays, W., Crawford, M., and Weigand, B., 2005, “Convection Heat and Mass Transfer”, McGraw-Hill, New York.

62. Rallabandi, A., Lei, J., Han, J.C., Azad, S., and Lee, C.P., 2013, “Heat Transfer Measurements in Rotating Blade-shape Serpentine Coolant Passage with Ribbed Walls at High Reynolds Numbers,” ASME Paper, GT2013-94162.

APPENDIX A

TURBINE VANE SUCTION SIDE HEAT TRANSFER COEFFICIENT

A. Liquid Crystal Instrumentation

The 20°C bandwidth liquid crystal (R29C20W, Hallcrest) was used to measure the initial temperature and the color changing time of the vane surface. The color of liquid crystals was recorded by a RGB camera with 24-bit color frame grabber board. The lightening was provided by two strong white LED light at temperature of 5000K. A total of 20 seconds of TIF image data was captured with 20Hz data frequency. In-house computer programs convert HUE value into temperature and then to heat transfer coefficients.

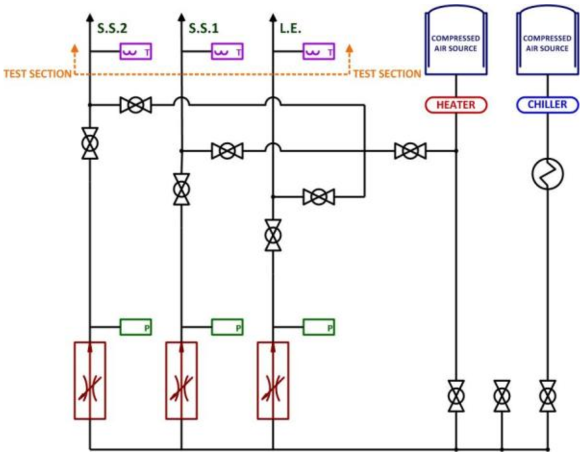

Figure 47 Transient liquid crystal test loop setup

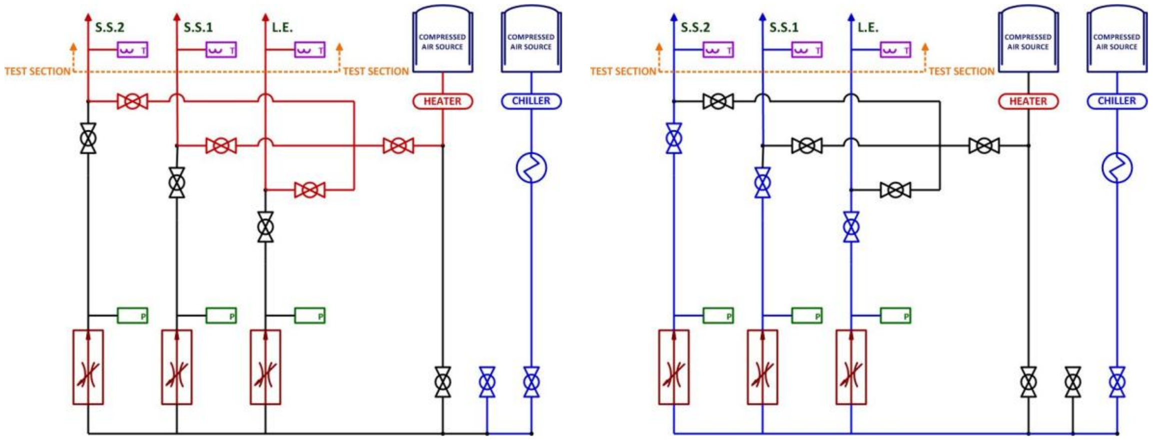

(a) Preheat **(b) Data acquisition**

Figure 48 Flow loop schematic for heat transfer experiments

The complete heat transfer experiment setup is displayed in **Fig47**. The flow loop is designed to preheat the SLS test vane to surface temperature 43°C before send in the main flow and this process usually takes 120 minutes. The schematic of preheat process is illustrated in **Fig48 (a)**. The preheat compressed air circulated through a 6kW heater and a 1 inch orifice meter before entering the test section. At this time most part of the three coolant loops are isolated from the preheat jets by individual valves. However, preheat jet and the experiment coolant jets still shared the same passage after the isolation valves. Compare both **Fig48 (a)** and **(b)**, one can identify the overlapped portion of preheat and experiment. The residual heat built up in the test blade during preheat process could significantly affect the experiment coolant temperature as well as the uncertainty of the study. To minimize the impact of residual heat, the experimental coolant jet is pre-cooled by NEXLAB HX150 chiller before injecting into the test section.

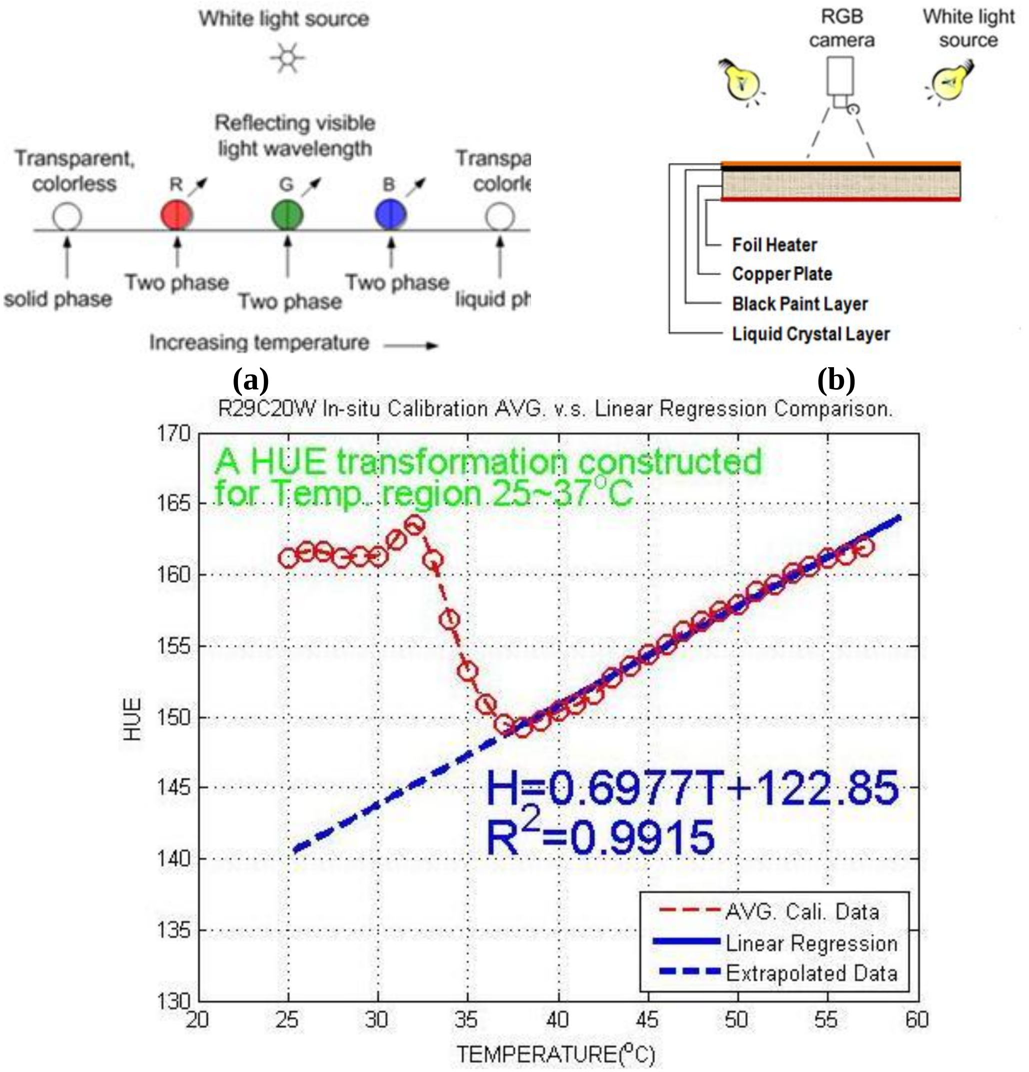

(a) (b)

(c)

Figure 49 Transient liquid crystal (TLC) working principle & R29C20W LC in-situ calibration

Real time coolant jet temperature history is recorded by NI Labview program. This information is used to support the Duhamel correction of changing coolant jet temperature in heat transfer coefficient calculation.

B. Transient Liquid Crystal

1. Measurement Theory

Liquid crystal (LC) working principle is displayed in **Fig 49(a).** The liquid crystal molecule undergoes a phase change from solid to liquid during the temperature changes from lower to upper boundaries. With proper calibration regarding the color (hue value) and temperature, one can easily refer the actual temperature with hue value. Since both LC solid and liquid states are transparent, and the two phase color changes with respect to temperature. Thus LC provides a reliable correspondence between surface temperature and hue value.

The 20°C bandwidth liquid crystal (R29C20W, Hallcrest) was used to measure the initial temperature of the vane surface, and the color changing time. The color of liquid crystals was recorded by a RGB color CCD camera with 24-bit color frame grabber board. From every pixel of the stored image, hue value was determined using the single hex cone color model. The surface temperature of each location (pixel) was determined using the calibrated hue versus temperature relation constructed by in situ calibration.

2. Calibration of Transient Liquid Crystal

Calibration was performed to find the hue versus temperature relation. An in situ calibration performed with a LC calibration device **(Fig 49(b))** located in the anneal cascade and the CCD camera at the actual data acquisition position. The calibration device was mainly constituted by a foil heater and a cooper plate. The thin foil heater was placed at the bottom of a 0.635 cm thick copper plate. And the copper plate was painted with plain black paint to avoid undesired reflection. Since the color display of liquid crystals depends on the background color, the same black surface paint was used for the calibration and the vane suction side heat transfer tests. Input voltage to the foil heater was set properly in order to increase the surface temperature by 1 °C, and enough time (10 minutes) was allowed for the temperature to be steady at each temperature step. At each temperature step, the surface temperature was acquired by two T-type thermocouple that attached to the back surface of black copper plate. Meanwhile, the color image of corresponding liquid crystal surface was recorded to a computer. The hue value was calculated from the stored image, and the relationship between hue and temperature was obtained.

Fig 49(c) displays the results of in situ calibration and the linear regression of R29C20W liquid crystal. The linear model generated by least square method with R^2= 0.9915 (goodness of fitting) was used to represent the correspondence of temperature and hue value at temperature range from 37 to 57°C (solid blue line). The lower LC clear-point is determined as 32°C by extrapolating (dashed blue line) the linear model.

C. Heat Transfer Coefficient

The transient liquid crystals technique was used to measure heat transfer and film-cooling effectiveness on the surface in this study. The local heat transfer coefficient over a liquid crystals coated surface can be obtained using a 1- dimensional semi-infinite solid assumption for the test surface, shown in **Fig 50**.

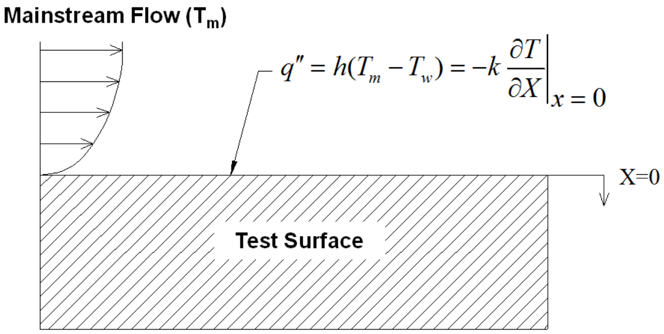

Figure 50 Heat transfer coefficient (HTC) measurement theory: 1D semi-infinite solid model

Note that the blade material (SLA) has a low thermal conductivity of 0.47W/m K. The test duration is smaller (2-10 sec) than the time required for the temperature to penetrate the full thickness of the blade tip material. Thus a 1-D transition, semi-infinite solid assumption is valid throughout the surface, except near the tip edges. The local heat transfer coefficient over a TLC coated surface can be obtained using a 1-

dimensional semi-infinite solid assumption with convective boundary condition at the test surface.

$$k\frac{\partial^2 T}{\partial x^2} = \rho C_p \frac{\partial T}{\partial t}$$

$$at\, t = 0, T = T_i$$

(12)

$$at\, x = 0, -k\frac{\partial T}{\partial x} = h\left(T_w - T_m\right)$$

$$at\, x \rightarrow \infty, T = T_i$$

The solution for the above 1-D transient conduction equation at the surface (x=0) is:

(13) $$\frac{T_w - T_i}{T_m - T_i} = 1 - \exp\left(\frac{h^2 \alpha t}{k^2}\right) erfc\left(\frac{h\sqrt{\alpha t}}{k}\right)$$

By knowing the initial temperature (T_i) of the test surface, the mainstream (recovery) temperature (T_m) at the cascade inlet and the color change temperature (T_w) at time t, the local heat transfer coefficient (h) can be calculated from Equation (13). For the film-cooling test, two similar transient tests with different coolant air temperature are needed to obtain the heat transfer coefficient (h) and the film cooling effectiveness (η). In order to determine the film cooling effectiveness, the mainstream temperature (T_m) in Equation (13) is replaced by the local film temperature (T_f). Which is a mixture of the coolant (T_c) and mainstream temperature (recovery temperature) (T_m). The film temperature is defined in terms of the film-cooling effectiveness η.

$$(14)\ \eta=\frac{T_w-T_i}{T_m-T_i}\quad or\quad T_f=\eta T_c+\left(1-\eta\right)T_m$$

Then, Equations (13) and (14) can be combined as follows:

$$(15)\ \frac{T_w-T_i}{T_f-T_i}=\frac{T_w-T_i}{\eta T_c+\left(1-\eta\right)T_m-T_i}=1-\exp\left(\frac{h^2\alpha t}{k^2}\right)erfc\left(\frac{h\sqrt{\alpha t}}{k}\right)$$

$$(16)\ T_w-T_i=\left\{\eta\left(T_{c,0}-T_m\right)+T_m-T_i\right\}\times F\left(\frac{h\sqrt{\alpha t}}{k}\right)+\sum_{i=1}^{n}\left[\eta F\left(\frac{h\sqrt{\alpha(t-\tau_i)}}{k}\right)\Delta T_{c,i}\right]$$

Considering the existence of residual heat phenomena in test section after preheat process, the coolant temperature (T_c) changes with time. With the real time data monitored from the NI thermal couple setup, Duhamel's superposition theorem can be applied to Equation (15) and the in house HTC calculation program were designed by Equation (16).

D. Experiment Condition

For LC studies, mainstream Mach number effect can be described by comparing M=1.0 and DR=1.5 for both Mach number 0.7 and 1.1 cases. Blowing ratio effect can be fathomed by Ma#=1.1 and DR=1.5 for M=0.0, 1.0 and 1.6 results. LC experiment parameters listed in **Table 7**. Although out of viewing range, the three rows leading edge showerhead holes were operated at the same blowing ratio as the suction side holes.

Table 7 Vane suction side LC test matrix

NUMBER	MACH NUMBER	DENSITY RATIO	BLOWING RATIO
L11-1	1.1	1.5	0.0
L11-2	1.1	1.5	1.6

E. Heat Transfer Coefficient Results

The liquid method in this part of study is used to measure the time difference between initial temperature and the lower clear point temperature (solid state of LC). The initial temperature is set to be 43 °C while the lower clear point is 32°C. **Fig51** displays the time difference between these two temperatures of each pixel. In Ma=1.1, M=1.6, DR=1.5 case **Fig51(b)**, since the coolant injected to the film coolant configuration was still in an evaluated temperature. Thus one can see the long trace of long changing time immediate downstream of the cooling holes. The real time coolant temperature history of M=1.6 is described in **Fig52**.

The coolant temperatures were measured at the midsection inside of each coolant passages. The highest temperature at the beginning is the preheat jet temperature, and the experiment took place around 15 seconds after the preheat air was redirected to ambient. The coolant supplied was from compressed carbon dioxide bottles with a room temperature at 22°C. The elevated coolant history clearly provide the information of how severe the residual heat from the preheat process affects the coolant jets. Even till the test ends, the coolant temperature is still higher than initial surface temperature (43°C).

Thus the coolant jet is actually heating the vane surface and this is the reasons instead of quicker LC changing time downstream the cooling holes, one can observe the long LC changing time traces.

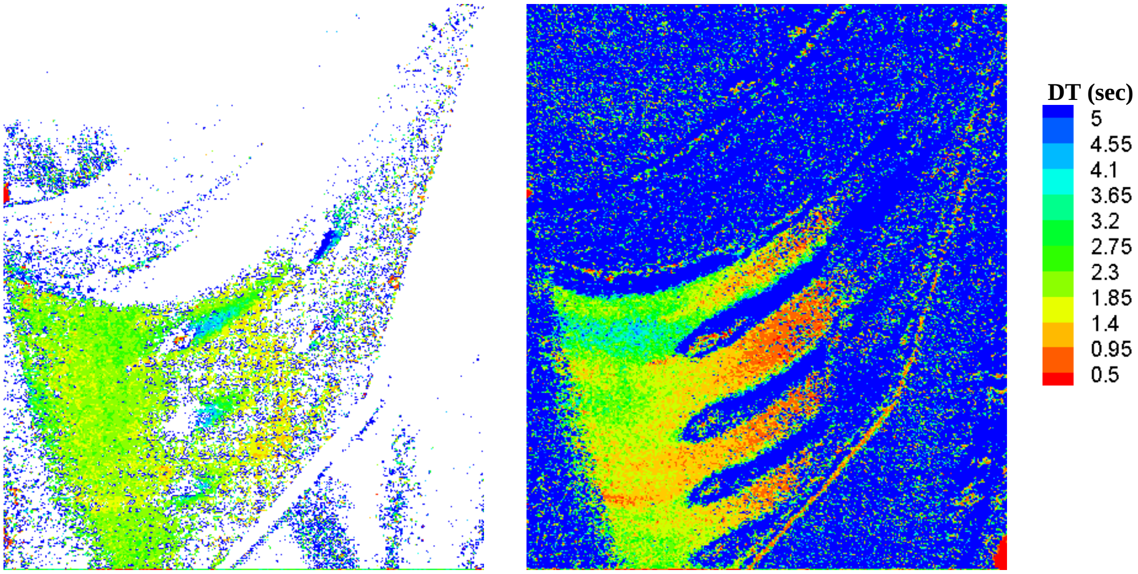

(a)Ma=1.1 M=0 **(b)Ma=1.1 M=1.6 DR=1.5**

Figure 51 LC lower clear point time

Applying the 1D semi-infinite model, the heat transfer is evaluated and displayed in **Fig53**. The heat transfer coefficient increased gradually from leading edge alone the vane suction side towards downstream. And this result is compatible with the actual trend experienced in real engine condition.

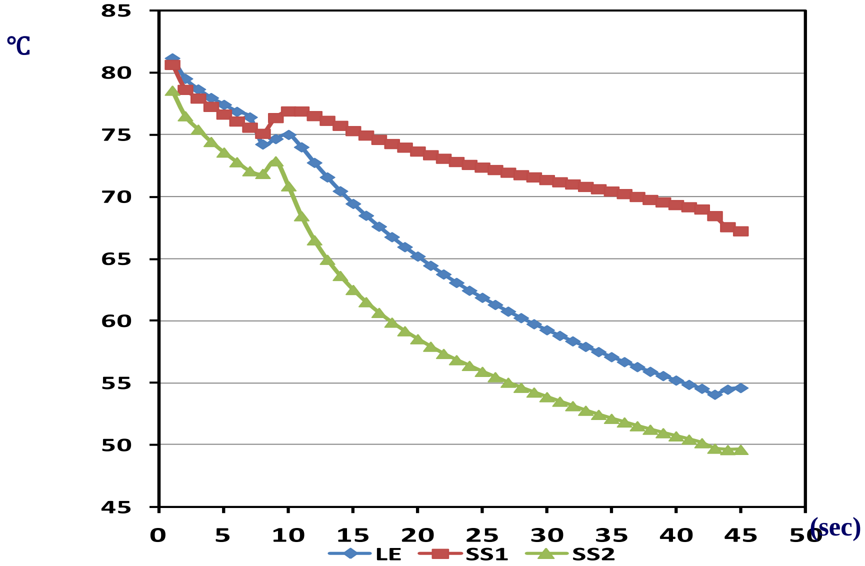

Figure 52 Coolant temperature history for Ma=1.1 M=1.6 DR=1.5

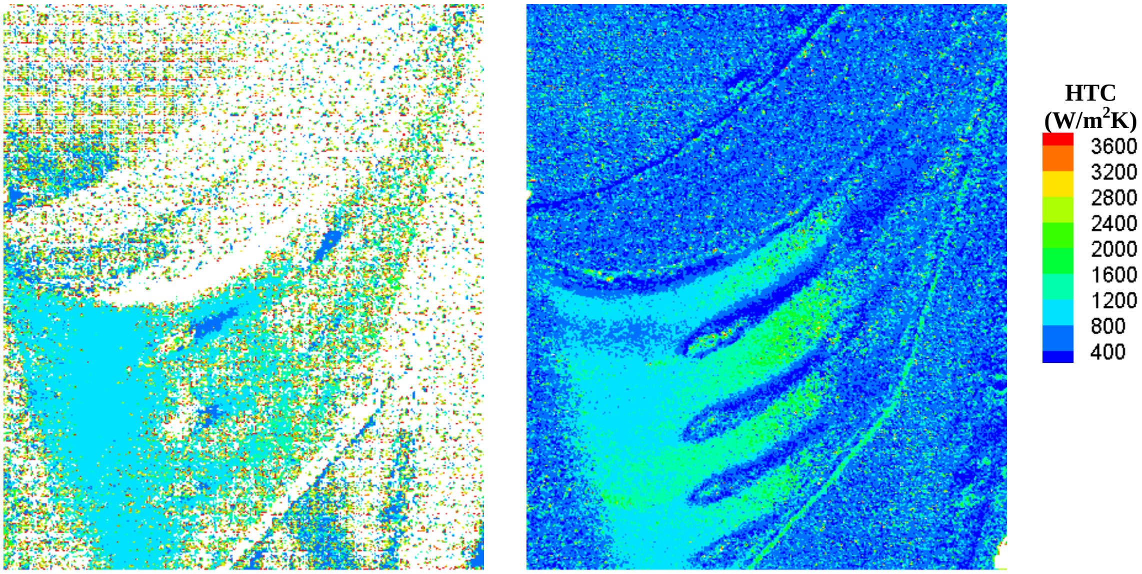

(a)Ma=1.1 M=0 **(b)Ma=1.1 M=1.6 DR=1.5**

Figure 53 Heat transfer coefficient distribution

F. Conclusion for Turbine Vane Suction Side Heat transfer Coefficient

Liquid crystal method is used to measure heat transfer coefficient on a transonic turbine vane suction surface. Blowing ratio effect on vane surface heat transfer coefficient was also determined. The key highlights are presented below:

1) Liquid crystal results greatly suffered from the view angle effect. From the in-situ calibration curve, the difference in HUE range between two liquid crystal phases is about 12. Thus the uncertainty of corresponding results is high.
2) Residual heat accumulated in test vane during preheat process greatly elevated the coolant temperature. This entangles the vane surface and coolant plenum heat transfer.
3) Current heat transfer data is calculated with the fixed initial temperature (R29C20W green point) and wall temperature (R29C20W lower clear point) and the time difference between these temperatures.
4) Needed to employ a more reliable method for thermal experiments in current test section. For example, the temperature sensitive paint method (TSP) maybe a potential candidate. Since the data response mechanism is more close to PSP.

APPENDIX B

TRANSONIC TURBINE VANE TEST SECTION DESIGN

The two major issues for current test section are orientated from heat transfer experiments. The limited visual access leads to limited data access and tremendous view angle effects. Since view angle effect is of primary importance to all spectrum based visual methods.

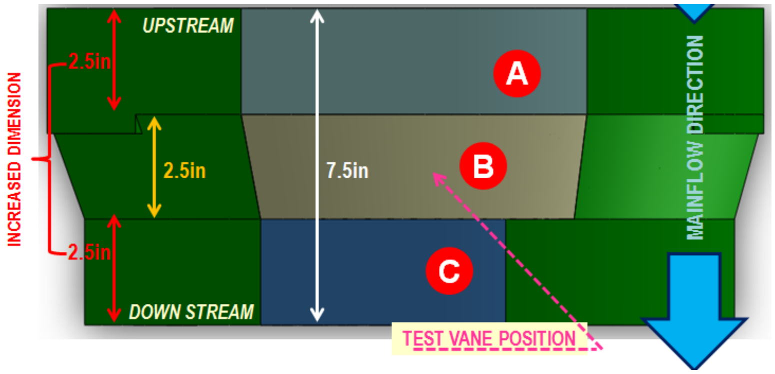

(a)Test section exterior dimension in stream line direction

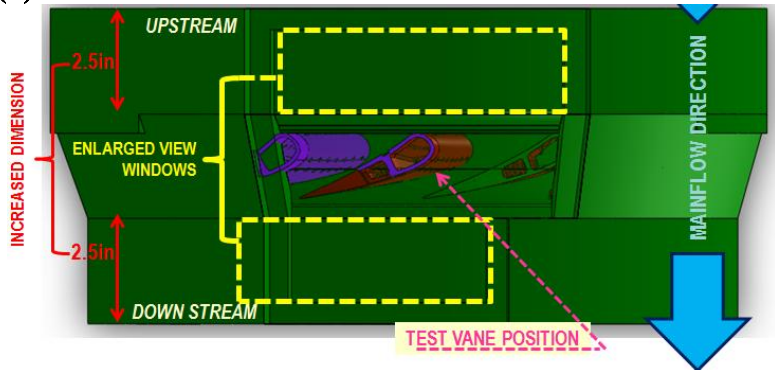

(b)Viewing glass location and visual access schematic
Figure 54 Vane cascade design (top view)

Thus this is the first task to consider for a new design. Residual heat accumulation during preheating process is also very important. The coolant temperature elevated significantly due to picking up energy from the test vane while circulating through the coolant passages. A brand new design is finished in response to obstacles experienced in current test section.

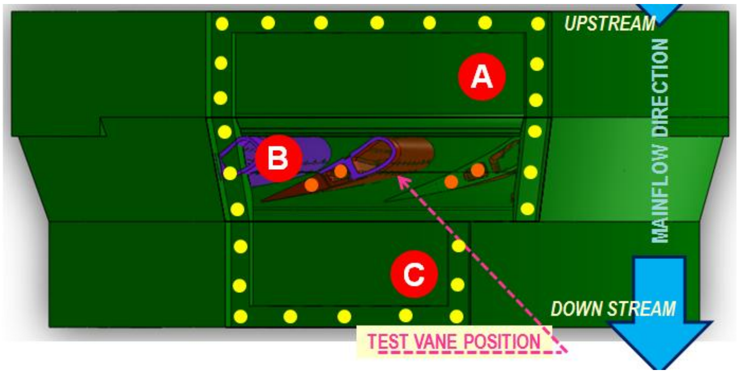

Figure 55 Viewing glass junction design

A. Increase Visual Access

Enlarge the viewing window under proper safety concern is the most important step. The main portion of new cascade will be fabricated by metal based SLS technology to fulfill structure concern. The test vane will be fabricated by SLA (Somos nanotool) material, due to the trade-off for both material strength and thermal conductivity. To avoid the window shielding effect that one experienced in the current test section. The viewing glasses in new test section are design to be by transparent acrylic with traditional machining. Also the window material strength and load condition were estimated and safety factor were calculated for each of the windows.

1. Main Structure Design

In order to increase the visual access, the new design extended 2.5 inch both upstream and downstream of current test section. **Fig 54** displays the top view of new dimension and viewing window location.

2. Viewing Window Safety Factor Estimation

The three viewing windows and their junctions with the main metal structure are considered to be the most critical part with material strength concerns in the design. **Fig 55** illustrates the junction design of all viewing glasses. All side tap sized 3/16 in and 0.2 in depth (marked yellow). Window A and C are bolted on three sides with 11 and 9 screws respectively. Window B bolted in three positions on both sides, two on the dummy vane, and two on the test vane (total 10). All taping on cascade sized 3/16 in and 0.5 in depth (marked orange).

Experience and test conditions from the current test section served as design constrain for the new design. The safety calculation was based on the following criteria: (1) 30 psi operational static pressure on test section inner wall. (2) Transparent Acrylic preselected as window material. (3) Acrylic shear strength is 9000 psi. Detailed safety calculation is listed in **Table 8.**

Table 8 Safety factor estimation

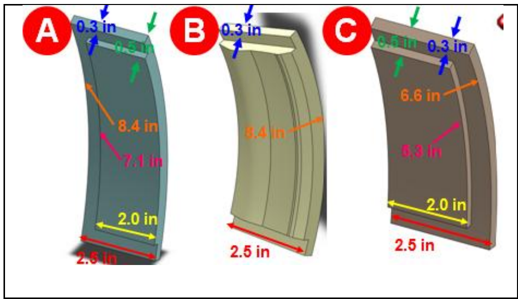	WINDOW NUMBER	PRESSURE LOAD AREA (in^2)	TOTAL SHEAR LOAD (lb-f)	SHEAR LOAD AREA (in^2)	AVERAGE SHEAR STRESS (psi)	SAFETY FACTOR
	A	13.98	419.40	3.30	127.1	70.82
	B	18.55	556.50	1.59	350.0	25.71
	C	9.46	283.80	2.65	107.1	84.01

3. Window Exterior Reinforcement Design

To further secure the viewing windows at the free side, two metal window exterior reinforcement rings designed to serve this purpose. One holds windows A & B and the other supports windows B & C. They are designed to have 0.25 inches metal overlap on both adjacent windows, and 0.25 inches in thickness (T_H). **Fig 56** described the schematic of metal reinforcement ring design. Ring AB and Ring BC are marked dark blue and green in the figure respectively.

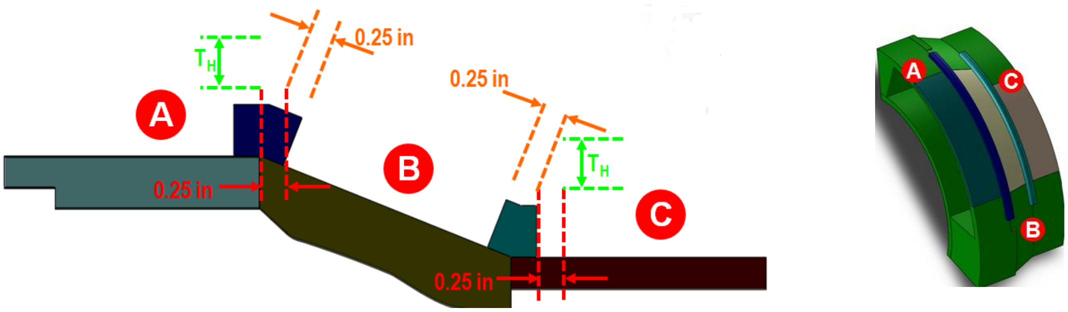

Figure 56 Window exterior reinforcement ring design

4. Simulated Visual Access of New Test Section Design

Fig 57 displays the view area of the new test section design simulated with Solidworks. Although the new design still suffered from blockage from the reinforcement rings, and the camera access to vane suction and pressure side are not perpendicular. In comparison with the current test section, new design had greatly increased the amount of view area. It provides access to the vane pressure side as well as the stagnation area. The view angle between the camera and target is most likely to reduce significantly, and this will greatly improve the thermal experiments data quality.

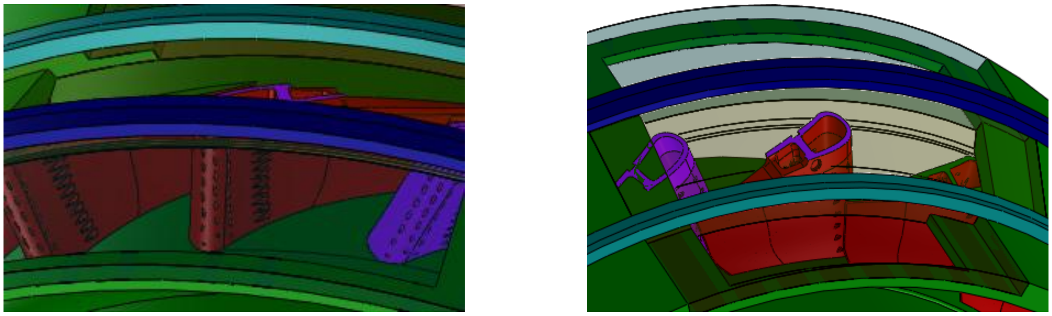

(a) Leading edge **(b) Suction side**

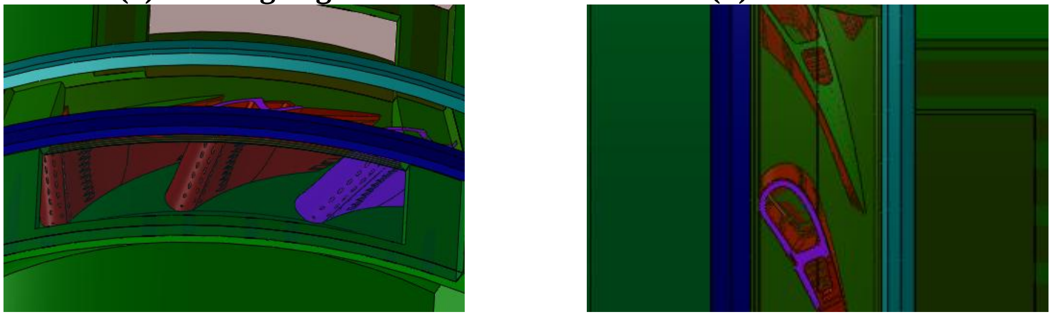

(c) Pressure side **(d) Hub endwall**

Figure 57 Simulated data acquisition view

B. Reduce Coolant Residual Heat Accumulation

To separate the preheat loop with the test vane coolant supply loop is the basic concept of reducing coolant residual heat accumulation. In order to achieve this goal, in the new design, the preheat jets will discharge from the adjacent dummy vanes on the cascade to the target surface. This will prevent the direct contact of coolant jets and preheated part, as well as benefit the heat transfer experiment accuracy. The new preheat concept and the design results are described in **Fig 58** and **59** respectively.

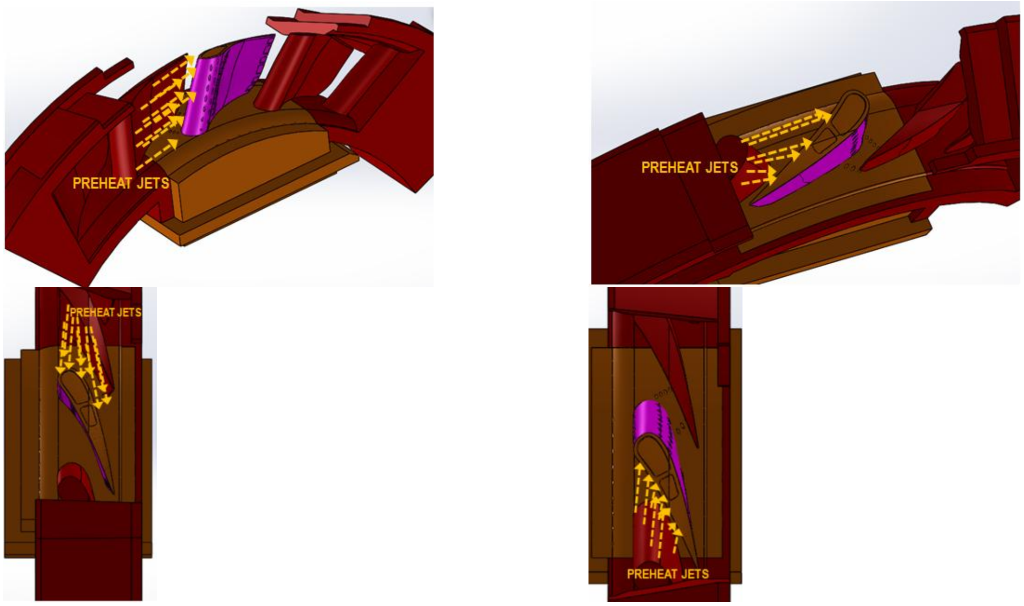

(a)Suction side **(b)Pressure side**

Figure 58 Conceptual preheat design for new test section

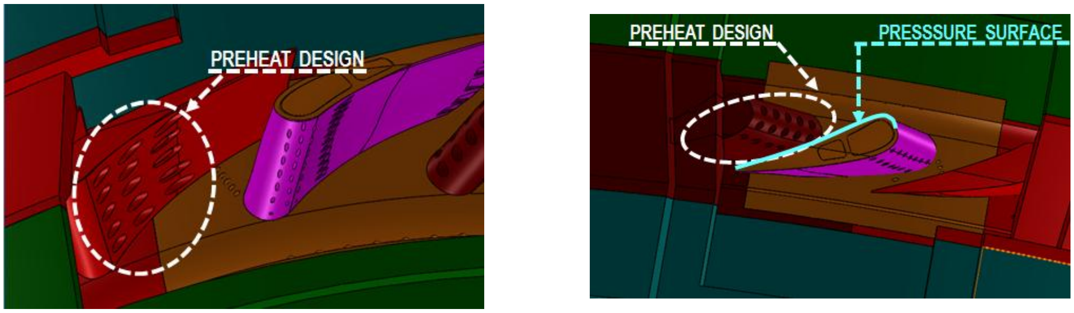

(a)Suction side **(b)Pressure side**

Figure 59 Preheat design for new test section

C. Increase Coolant Supply Uniformity

Coolant supply passage of current design lacks of actual plenum volume. This leads the coolant to stagnate at the tip end of each passage and contributes to non-uniformity of ejection amount from each coolant hole. **Fig 60** displayed the newly designed center test assembly to provide more uniform coolant jet distribution at each cooling rows.

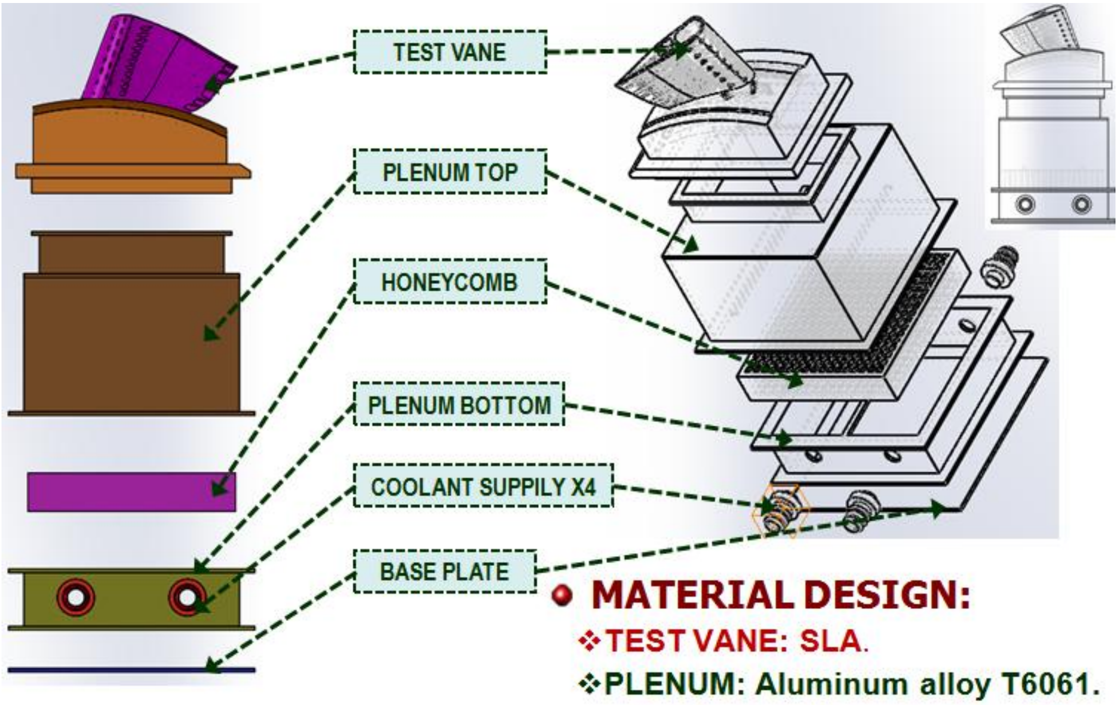

Figure 60 Center test assembly design for new test section

In order to broaden the study to cover the platform film cooling, two the interchangeable test vane were designed. One for vane surface film cooling, equipped with cooling configurations on pressure side (1 row), leading edge (3 rows), and suction side (2 rows). The other equipped with two rows of film cooling configuration at the passage and one row at cascade upstream. **Fig 61** shows the test vane design for both platform and vane surface film cooling.

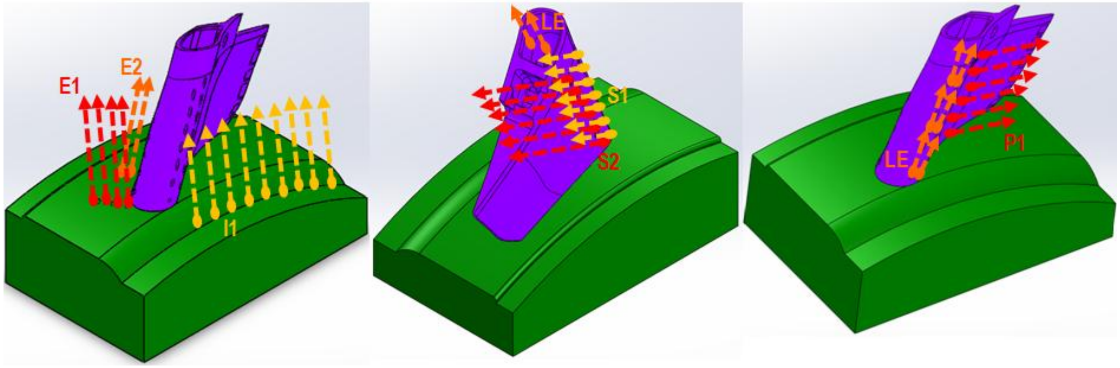

(a) Platform **(b)Vane surface**

Figure 61 Interchangeable film cooling test vane design for new test section

D. New Test Section

The design concepts of the new test section design are summarized in this section.

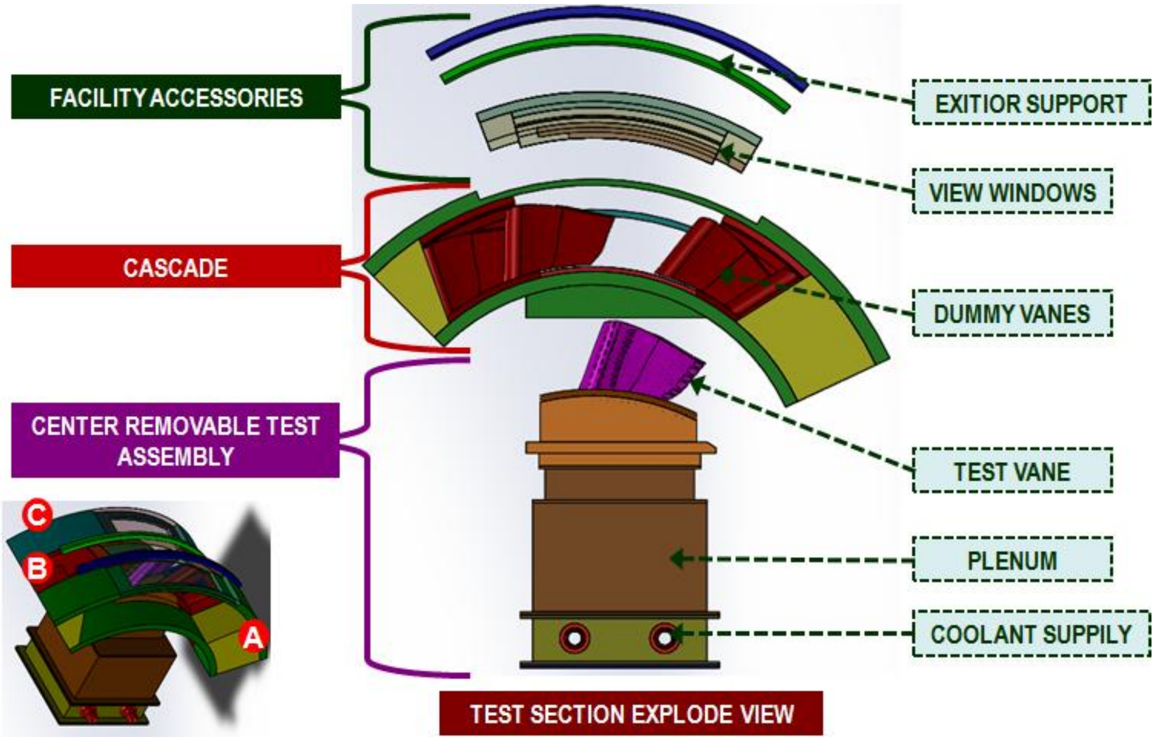

Figure 62 Test section total assembly 2D explode view

1. Test Section Total Assembly

The basic idea of test section total assembly is listed in the following. **Fig 62, 63** illustrated the 2D explode view of the total assembly.

(1) Five vane four passages cascade design.

(2) Test vane on center removable assembly, designed with complete vane and end-wall film cooling features.

(3) Four solid dummy vanes provide possibilities for improving the preheat process.

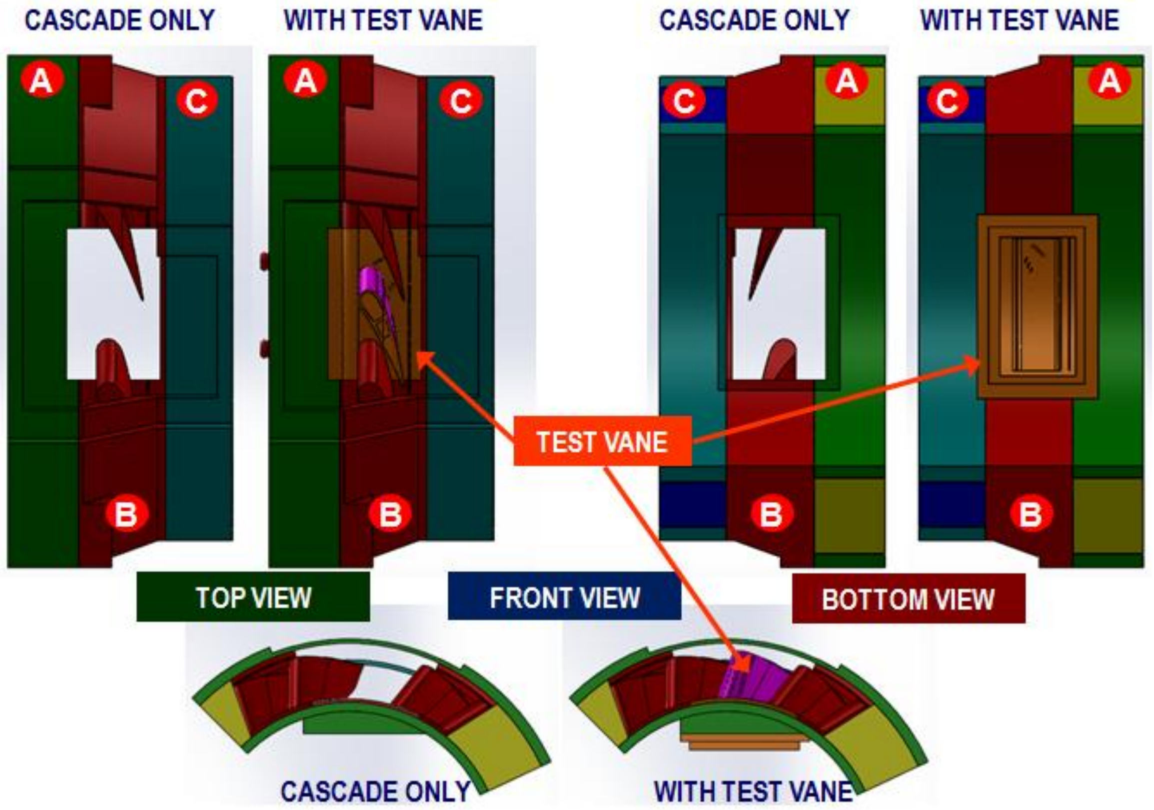

Figure 63 Test section total assembly (top and bottom view)

2. Fabrication and Cost Control

The primary concern in fabrication is the cost control. The fabrication method and the material is listed as the following. And the total cost estimation of the test section is $36,000.

(1) Three sections cascade structural design.

(2) Due to feature complexity, section B planned to be fabricated with metal SLA technique.

(3) Sections A & C will be manufacture by traditional machining on Aluminum alloy T6061.

(4) Cascade sections A & C are further divided into four parts respectively (**Fig 64**).

(5) This is beneficial for cost control since it lowered machining hardware and technique requirements.

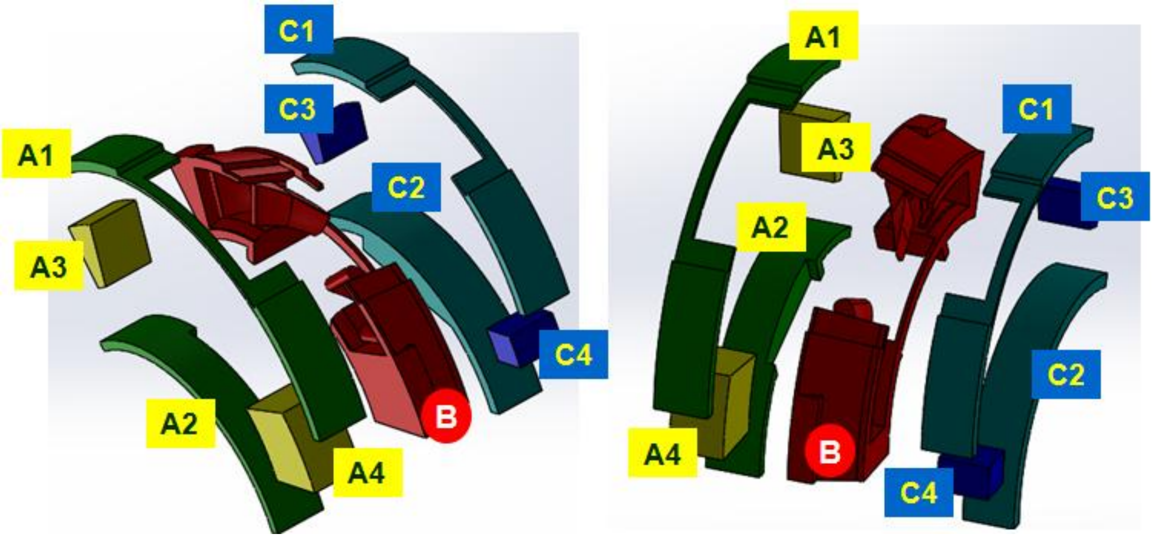

Figure 64 Section A and C assembly

APPENDIX C

NEW INTERNAL ROTATING COOLANT PASSAGE DESIGN

A marvel internal cooling feature design of broken staggered turbulators planned to compare with the current results of standard 45° tubrulators presented in this study. The design process is listed in the following and the corresponding figure in **Fig 65**.

(1) Start form the original rib configuration: Square rib, e=1.59 mm. 45°, p/e =10.

(2) Rib A configuration: Dimension: 1/3 of the original rib, identical starting point as original rib.

(3) Rib B configuration: Dimension: 1/3 of the original rib, parallel shift up half original rib spacing (7.95mm) toward the previous rib A.

(4) Rib C Configuration: Dimension: 1/3 of the original rib, turn 90° at the 2L/3 from Rib A starting point.

(5) New Rib configuration.

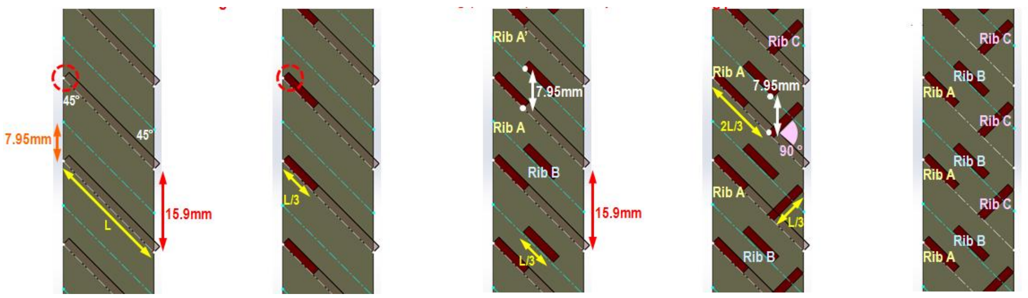

(1) **(2)** **(3)** **(4)** **(5)**

Figure 65 New configurations (broken stagger turbulators) design procedure